A LAYERWISE APPROACH TO MODELING PIEZOLAMINATED PLATES

A THESIS SUBMITTED TO
THE GRADUATE SCHOOL OF NATURAL AND APPLIED SCIENCES
OF
MIDDLE EAST TECHNICAL UNIVERSITY

BY

CEVHER LEVENT ERTÜRK

IN PARTIAL FULLFILMENT OF THE REQUIREMENTS
FOR
THE DEGREE OF DOCTOR OF PHILOSOPHY
IN
AEROSPACE ENGINEERING

JULY 2005

Approval of the Graduate School of Natural and Applied Sciences

_____

Prof. Dr. Canan Özgen
Director

I certify that this thesis satisfies all the requirements as a thesis for the degree of Doctor of Philosophy.

_____

Prof. Dr. Nafiz Alemdaroğlu
Head of Department

This is to certify that we have read this thesis and that in our opinion it is fully adequate, in scope and quality, as a thesis for the degree of Doctor of Philosophy.

_____

Assoc. Prof. Dr. Ozan Tekinalp
Supervisor

Examining Committee Members (first name belongs to chairperson of the jury and the second name belongs to supervisor)

Prof. Dr. Mehmet Akgün   (Yeditepe Üniv.,MAK) _____

Assoc. Prof. Dr. Ozan Tekinalp   (METU,AEE) _____

Dr. Volkan Nalbantoğlu   (ASELSAN) _____

Assoc. Prof. Dr. Altan Kayran   (METU,AEE) _____

Assoc. Prof. Dr. Ata Muğan   (İstanbul Teknik Üniv.,MAK) _____

I hereby declare that all information in this document has been obtained and presented in accordance with academic rules and ethical conduct. I also declare that, as required by these rules and conduct, I have fully cited and referenced all material and results that are not original to this work.

Cevher Levent Ertürk

ABSTRACT

A LAYERWISE APPROACH TO MODELING PIEZOLAMINATED PLATES

Ertürk, Cevher Levent

Ph.D. Department of Aerospace Engineering

Supervisor: Assoc. Prof. Dr. Ozan Tekinalp

January 2005, 152 pages.

In this thesis, optimal placement of adhesively bonded piezoelectric patches on laminated plates and the determination of geometry of the bonding area to maximize actuation effect are studied. A new finite element model, in which each layer is considered to be a separate plate, is developed. The adhesive layer is modeled as a distributed spring system. In this way, relative transverse normal and shear motion of the layers are allowed. Effect of delamination on the adhesive layer stresses is also studied and investigated through several case studies. Optimization problems, having single and multiple objectives, are investigated for both actuator placement and selective bonding examples. In these case studies, 2D and 3D Pareto fronts are also obtained. 'Hide and Seek Simulated Annealing' method is adapted for discrete problems and used as the optimization technique for single-objective problems. Finally, Multiple Cooling Multi Objective Simulated Annealing optimization algorithm is adapted and used in multi-objective optimization case studies.

Keywords: Finite Element Method, Laminated Plates, Piezoelectric, Multi-Objective Optimization, Selective Bonding

ÖZ

PİEZOELEKTRİK KATMANLI PLAKALARIN TABAKASAL
YAKLAŞIMLA MODELLENMESİ

Ertürk, Cevher Levent

Doktora, Havacılık ve Uzay Mühendisliği Bölümü

Tez Yöneticisi: Doç. Dr. Ozan Tekinalp

Ocak 2005, 152 sayfa.

Bu çalışmada, çok katmanlı plakalar üzerine yapıştırılmış piezoelektrik yamaların en iyi yerleşimi ve yapışkan alan geometrisinin, eyleyicinin etkisini artıracak şekilde eniyilenmesi incelenmiştir. Bütün katmanların ayrı bir plaka olarak varsayıldığı yeni bir sonlu elemanlar modeli geliştirilmiştir. Yapıştırıcı katman, dağınık yay sistemi olarak modellenmiştir. Bu şekilde katmanların birbirlerine göre dikey ve kayma hareketleri mümkün kılınmaktadır. Çeşitli örnek çalışmalar ile, yama ve ana yapı arasındaki ayrılmanın yapıştırıcı katmanda ortaya çıkan gerilmelere etkisi de incelenmiştir. Bir ve daha fazla amaçlı eniyileme problemleri, yama pozisyonları veya yapıştırma geometrisi tasarım parametresi alınarak çözülmüştür. Bu örneklerde, iki ve üçboyutlu Pareto sınırları elde edilmiştir. 'Araştır ve Sakla – Tavlama Benzetimi' eniyileme yöntemi, kesikli tasarım parametreleri kullanılabilecek şekilde uyarlanmıştır. Son olarak, çoklu soğutmalı çok amaçlı tavlama benzetimi eniyileme algoritması birden fazla amaçlı eniyileme problemleri için uyarlanmış ve örneklerde kullanılmıştır.

Anahtar Kelimeler: Sonlu Elemanlar Yöntemi, Çok Katmanlı Plakalar, Piezoelektrik, Çok Amaçlı Eniyileme, Seçici Yapıştırma

ACKNOWLEDGMENTS

TABLE OF CONTENTS

CHAPTER 1

INTRODUCTION

1.1. GENERAL

Designing of adaptive structures consisting of piezoelectric actuators and sensors is a multidisciplinary problem, which requires an extensive background on [1],[2];

- Structural modeling,
- Optimization,
- Control,
- Driver electronics.

This study is mainly concentrated on a new structural modeling technique for multilayer plates with bonded piezoelectric layers. Unlike equivalent single layer (ESL) models, developed structural model allows the individual deformation of all layers, accounts for adhesive layer flexibility and may include multiple delamination regions. Although some multilayer models may account for delamination of the adhesive layer, the approach proposed in this thesis offers a much simpler solution. Furthermore, it is also possible to examine interlaminar stresses between the piezoelectric and nonpiezoelectric layers.

In this study, in addition to actuator placement problems, also studied by numerous researchers in the past, a new type of optimization problem, whose design variables are related to the geometry of the delamination region between the actuator patches and substrate, is investigated. These problems are solved for single and multiple objective optimization case studies. 'Hide and Seek' simulated annealing optimization method is used for single objective optimization problems, whereas Multiple Cooling Multi Objective Simulated Annealing (MC-MOSA), optimization algorithm is adapted for selected multi objective discrete optimization problems.

Many practical applications, listed below, are good examples when placement of actuators and/or sensors is the design variables;

- Vibration suppression
- Aeroelastic control
- Sound attenuation
- Health monitoring systems
- Shape control

Therefore corresponding objective functions with these applications may also be used in optimization problems. In this study, static deformations and/or modal displacements are selected as objective functions. Choosing modal displacements of most contributed modes to the response as objective functions is a very effective way in obtaining best actuator placement. However, best actuator positions, which maximize the actuation effect for one mode, may not help us to decrease control effort for other modes. Hence, Pareto-optimum solutions for these multi-objective cases must be identified. Modal displacements of different vibration modes are generally very conflicting design objectives. Therefore, well defined Pareto frontal surfaces and high number of Pareto solutions may be expected.

1.2. THESIS OBJECTIVES

The first objective of this thesis is to develop a new structural model for multilayer plates with piezoelectric actuators and sensors. The model shall be capable of the examining the effects of adhesive layers and possible delamination regions.

Second objective is to address piezoelectric actuator placement problem using both a single objective as well as multiple conflicting objectives. Either location of patches or parameters related to the geometry of delamination between the actuator layer or patch and the substrate is considered as design variables. When same finite element mesh is used for different configurations, design variables are no more continuous. Therefore, number of all possible configurations is limited. In some cases full set of combinations may be evaluated and best configurations can be identified. Alternatively, a smarter way of seeking for global optimum may be accomplished by using stochastic methods. 'Hide and

Seek' simulated annealing method is employed with minor modifications for discrete problems.

1.3. BACKGROUND

1.3.1. Modeling Multilayer Structures

Multilayer plates containing piezoelectric sensor, and actuator layers were extensively addressed in the literature. Various models as well as discretization methods were proposed.

Equivalent single layer (ESL) theories are usually employed in modeling laminated plates. It is also used for plates with piezoelectric layers. Pletner and Abramovich [3] investigated the static and dynamic response of anisotropic piezolaminated shells with spatially discrete sensors and actuators using Kirchhoff-Love plate assumptions. They developed a method that converts induced-strain loading due to applied voltage to the piezoelectric material to the equivalent mechanical loading. Reddy [4] studied both classical laminated plate theory (CLPT) and first-order shear deformation theory (FSDT) models of laminates with integrated sensors and actuators. Besides finite element solutions, Navier solutions are presented as well [4]. Liu [5] also used CLPT and developed a non-conforming rectangular plate-bending element. Higher order shear deformation theories are also used. For example, Correia, et al. [6] developed three different finite elements having 5 to 11 degrees of freedom for elastic behavior and 1 degree of freedom for piezoelectric behavior at each node. The deformations, frequencies and stresses predicted by the models are compared to each other and to those available in the literature for thin plates. For thick plates, piezoelectric layer stresses, predicted by the five degrees of freedom model was substantially different than the eleven degrees of freedom model. In ESL plate theories, the derivatives of the displacements are continuous in the direction of plate thickness. This leads discontinuous inter-laminar stress field since each layer has different material properties or orientation. Many other phenomena such as calculation of shear correction factor for arbitrary stacking sequence and shear locking for thin plates when using FSDT or having unrealistically high bending stiffness for thick plates when using CLPT are well-known problems of ESL models.

In his historical note, Carrera examines the origins of multilayer plate theories [7]. He presents three distinct zigzag theories: Proposed by Leknitskii in 1935, by Ambartsumian in 1958, and finally by Reissner in 1984. It is indicated that the original work of Lehnitskii, although quite promising, is ignored in the literature. It is also shown that most of the current zigzag theories are the particular cases of Ambartsumian's approach. The Reissner's approach, that uses the Reissner's Mixed Variational Theorem, permits assumptions on both displacements and transverse stresses. Carrera, using Reissner's approach employed two independent piecewise continuous fields for displacements and for transverse shear as well as normal stresses [8]-[11]. The theory is applicable to both ESL models and layerwise models. Brank and Carrera [12] imposed interlaminar shear stress continuity and developed four-node ESL finite element. Icardi [13], on the other hand, formulated an eight-node ESL finite element by assuming a third order zigzag type displacement field.

Both full layerwise theories and partially layerwise theories are extensively used for modeling laminated piezoelastic structures. In full layerwise theories all displacement components have interpolation functions for each layer separately in the thickness direction. One-dimensional piecewise continuous Lagrange interpolation functions are generally used to approximate the displacement and electrostatic potential fields in the direction of thickness [14],[15]. Defining a layerwise rotation field, which is independent from the displacement field, is also used in some studies. Tzou and Ye [16] used layerwise constant shear angle theory to develop piezoelastic triangular shell elements. In the study of Masud and Panahandeh [17], the displacement field is continuous through the thickness, although, rotation field is layerwise continuous and discontinuous across these layers. Saravanos [18] uses continuous displacement field model through the thickness while the electric potential is layerwise continuous. A layerwise treatment of displacements and electric potentials was also implemented [19].

In addition to the ESL and layerwise finite element models, examples on 3D finite elements may also be found in the literature. Due to high side-to-thickness ratio, standard 3D finite elements are not adequate for accurate modeling of plates. Therefore special 3D elements must be developed which does not have an aspect ratio restriction. There are also examples of using 2D and 3D elements together when modeling plate type structures with piezoelectric layers. For example, Tzou and Tseng [20] derived a piezoelectric hexahedron

finite element and they used it with a 2D-plate structure. Ha and Chang [21] also studied the response of piezo-laminated composites using finite elements. For this purpose they developed an eight-node three-dimensional composite brick element, based on the theory of elasticity for anisotropic and inhomogeneous materials. Detailed information on different type of elements developed for laminated structures and comparisons between these models may be found in references [22],[23].

Moorthy and Reddy [24],[25] indicates the advantages of using layerwise theories in modeling delamination. However, most layerwise theories assume that interconnections between layers are perfect. Thus, in many models relative deformation between adjacent layer surfaces are not permitted to occur. Yuceoglu and Updike, however, considered adhesive layer flexibility [26]. Tekinalp, et al. [27],[28] while investigating the vibration of multilayer beams, modeled the adhesive layers as distributed normal and shear springs. Thus, the layers were permitted to deform relative to each other. Euler-Bernoulli and shear deformation theories are used, and effect of adhesive layer flexibility as well as shear deformation on beam bending frequencies is investigated. These ideas are later applied to multilayer plates and lap joints [29] in examining their mode shapes and natural frequencies.

In this study the modeling approaches presented in references [27]-[29] are extended to modeling multi-layer plates containing piezoelectric sensor and actuator layers. The layers are modeled using Classical Plate Theory. Instead of the integration matrix and transfer matrix methods used in the previous studies, special finite elements are developed in this study. In addition the delamination effects are also considered. Four-node, displacement based finite elements uses Lagrange and Hermite type interpolation functions for in plane and bending deformations of each layer. The layers can be isotropic or orthotropic, or may be made of piezoelectric materials to be used as sensors or actuators. To decrease the number of nodal degrees of freedom, some of the layers may be grouped together using a proper ESL approach. The element developed in this study is also suitable for modeling interlaminar stresses and modeling delamination. For example, defining a very soft adhesive, or completely removing adhesive stiffness from the element stiffness matrix a simple model of delamination may be obtained. In this thesis, the developed model is abbreviated as MLP-FAB (Multi-Layered Plate with Flexible Adhesive Bonding).

5

1.3.2. Actuator Placement

References [1] and [2] are survey papers covering almost all studies on optimal placement of actuators and sensors up to year 2002. These two papers completes each other, since Padula and Kincaid [1] reviewed the studies conducted before 1999 and Frecker only considered the papers published after 1999. Although studies, not including formal optimization techniques, were also considered in [1], Frecker [2] surveyed papers including optimal solutions. She also classified the papers according to optimization strategies, in five different groups such as:

(1) Placing the actuators on existing structures: Generally only locations of actuators are considered as design variables. In some studies, sizing of actuators is also included.

(2) Optimizing actuator location and controller parameters together: Controller parameters, such as feedback gain or actuation voltages are optimized either simultaneously or in sequence with actuator locations.

(3) Simultaneous optimization of the structure and actuator: The parameters of the base structures, which are generally beams and plates, as well as actuator parameters are taken as design variables.

(4) Drive electronics parameters: Optimal design of electronics, such as power amplifier, is considered.

(5) Structural optimization for a particular actuator: As opposed to first group of studies, structure is optimally designed for one or more predetermined actuators.

Among these, first three groups are mostly related to our study. In addition to the papers referenced in these survey papers, more recent studies, related to optimal placement of actuators are also surveyed. These studies, related to first two groups, which are mentioned above, are listed in Table 1.1. For some of these studies, controller variables are also selected as design variables besides the placement of the actuators.

Among the optimization methods, genetic algorithms are mostly used [30],[33],[36]-[40]. However, simulated annealing algorithm is another well-known

method for combinatorial optimization problems. Superiority of SA method over gradient descent method is emphasized in Reference [32].

Selection of the next candidate solution from the current one is another question in optimization problems. In the SA algorithm proposed by Metropolis et al. [41], the next candidate solution is created by randomly displacing an atom by a small amount. Similarly, for using SA in a combinatorial optimization problem, a slight and random change from previous values of design variables gives a suitable candidate solution. On the other hand, it may be desirable to jump a far point in the design space. When searching for the next trial point, methods such as random walk can easily be adjusted for small or relatively bigger steps.

Most of the methods for finding solutions to optimization problems with discrete parameters are based on iterative improvements. Starting with an initial trail solution, iterative improvement techniques repeatedly consider changes in the present solution and accept only those solutions that improve the performance criterion. The disadvantage of these techniques is that they may become trapped in a local optimum. Without having a mechanism to allow climbing out of local optima, these techniques may fail to discover global or any other local optima. The simulated annealing algorithm provides such a mechanism, which was introduced by Kirkpatrick et al. [42] for combinatorial optimization. In order to run away from local minima, non-improving solutions should also be accepted with a certain probability. Acceptance probability of the non-improving solutions is decreased slowly. Therefore, the SA method differs from conventional iterative improvement methods mainly in the introduction of a slowly decreasing probabilistic acceptance of non-improving solutions.

Simulated annealing method was used by Chen et al. [43], to optimize the placement of both active and passive members in truss structures. They aimed maximization of energy dissipated over a finite time interval which is an integer multiple of maximum period of the dynamical system. Their performance criterion is an effective measure of degree of damping augmentation. They defined the optimization problem:

Maximize finite time energy dissipation, function of member locations, feedback gains and passive damping.
Subject to the constraints of upper bounds on the feedback gains.

7

Liu, et al. [44] also used SA for the multi objective optimization problem, where structural member sizes and locations of actuators and sensors are design variables. Objective function was control cost, total mass, robustness, measurement of controllability and observability or weighted sum of all. Developed method was used to optimize a space truss. Another implementation of SA algorithm is studied by Maxwell, et al. [32] given in Table 1.1. For that specific application SA gives more appropriate solutions, since it is not entrapped by local minima.

Table 1.1. Most recent studies on optimal placement of actuators.

Ref.	Objective Function(s)	Design Variables and Constraint Function(s)	Optimization Method	Act. Type	Application
[30] Li, Cheng, Gosselin, 2004	Minimize the acoustic potential energy	Actuator locations, no constraint	GA	PZT	Cylindrical shell with an internal floor partition
[31] Damaren, 2003	Maximize damping injected into each mode	Actuator locations, no constraint	Searching full combination of selected subset of design space	PZT	Box: system of joined plates
[32] Maxwell, Asokanthan, 2003	Minimize tip displacement error, hub angle error and total mass	Actuator locations, control parameters for independently actuated PZTs	SA, GD (gradient descent)	PZT	Single link flexible manipulator
[33] Yan, Yam, 2002	Minimize attenuation time and control power	Number and location of actuators	GA for placement, eigenvalue distribution of energy correlative matrix for optimal number of actuators	PZT	Space truss
[34] Ip, Tse, 2001	Minimize modal displacements	Location and orientation of PZT patch	Finding objective function surface (not formal)	Single PZT	Isotropic rectangular plate
[35] Gao, Chen, Ma B., Ma X. S., 2003	Maximize energy dissipation	Active bar placement and feedback gains, Constraints: on dynamic stress and displacement response	Full combination	Active bars	Truss
[36] [3.9] Locatelli, Langer, Müller, Baier, 2000	Maximize active damping, minimize the mass	Actuator and sensor positions, control parameters, stiffness and mass distribution	GA (MOGA) or a gradient-based method	PZT and active bars	Beam, plate or truss

Although there are few studies [45],[46], which includes the effects of the bonding layer on the actuation of piezoelectric layers, to the best of this author's knowledge, there has not been any work that incorporates the optimization of debonding region between the actuator layer and substrate. In this study, by assigning size and location of debonding area as design variables, an optimum rectangular unbonded region is found to obtain maximum actuation considering different objective functions.

1.4. ORIGINAL CONTRIBUTIONS

To the author's knowledge, the following contributions are original to this thesis:

- Modeling approach: Although the use of distributed spring on modeling multilayer plates has been previously presented [27], inclusion of piezoelectric layers is carried out in this thesis. To analyze the model a new finite element is developed.

- Calculation of stresses in the adhesive layer and correction for normal stiffness

- Multi objective actuator placement based on adaptation of MC-MOSA optimization method for discrete problems

- Tailoring the bonding area to maximize actuation effect of the piezoelectric actuator.

1.5. SCOPE

In Chapter 2, modeling of multilayer plates is investigated. Actuator and sensor equations of multilayer plate with surface bonded piezoelectric patches are derived. A new finite element is developed for this piezoelectric plate model. Several case studies are presented: static analysis of a square and a rectangular plates with surface bonded piezoelectric patches, a narrow plate in cylindrical bending to compare with results found in the literature, a square plate to compare its deformation and frequencies with the ESL model, and a delaminated plate to examine the effects of delamination on deformation and adhesive layer stresses.

In Chapter 3, the optimum placement of piezoelectric actuators and selective bonding of the actuator layer is studied. State space form of the equations of motion is presented. In addition to modal displacements, eigenvalues

of the controllability grammian are used in the objective functions. Different performance indices are introduced and compared. Single and multiple objective optimization case studies are conducted. Effects of different optimization parameters and search techniques on the success of the optimization methods are investigated. 2D and 3D Pareto fronts are obtained in multi objective optimization problems. Control spillover problems are also considered and studied in multi objective optimization problems.

In Chapter 4, these studies are summarized and conclusions are given.

CHAPTER 2

A LAYERWISE APPROACH TO PIEZO-ELECTRIC PLATES

2.1. INTRODUCTION

Multilayer plates containing piezoelectric layers are modeled considering the deformation of the adhesive layers. Special finite elements, that use linear Lagrange and conforming Hermite type interpolation functions, are developed. The results of the formulation are compared with the other results presented in the literature. Since flexible bonding formulation is also suitable for modeling delamination, case studies containing partially delaminated PZT patches are presented. It is shown for a cantilever plate that, while partial delamination between the piezoelectric and non-piezoelectric layers does not affect the maximum deformation significantly, it affects the local stresses near delaminated regions.

In the following sections, finite element formulation of the multilayer plate system containing piezoelectric, and non-piezoelectric layers is given and results of the MLP-FAB model are compared to the results available in the literature as well as to the MSC.NASTRAN results. A correction to transverse normal stiffness that improves the prediction of transverse normal stresses in adhesive layer is proposed and its effectiveness is demonstrated. Adhesive layer stresses created by an electrically loaded piezoelectric patch are given and discussed. Effect of delamination on adhesive stresses is also investigated. Finally, general conclusions of this study are given.

2.2. FORMULATION OF THE PROBLEM

2.2.1. Assumptions and Displacement Field

In this study following assumptions are made:

1. Adhesive layers thicknesses are small compared to the thicknesses of adherends. For this reason, the adhesive layers are assumed to deform linearly. Only transverse normal stress (σ_z^a) and strains (ε_z^a), and in-plane shear stress (τ_{xz}^a, τ_{yz}^a) and strains ($\gamma_{xz}^a, \gamma_{yz}^a$) are taken into account. The in-plane stretching of the adhesive layer is neglected, since adhesive layer is very thin compared to other layers and its stiffness in that direction is quite small.

2. Adherends are modeled using classical plate theory assumptions.

3. Mass of the adhesive layer is ignored.

4. Deformations are small.

5. Possible contact between the layers, when delamination exists, is ignored.
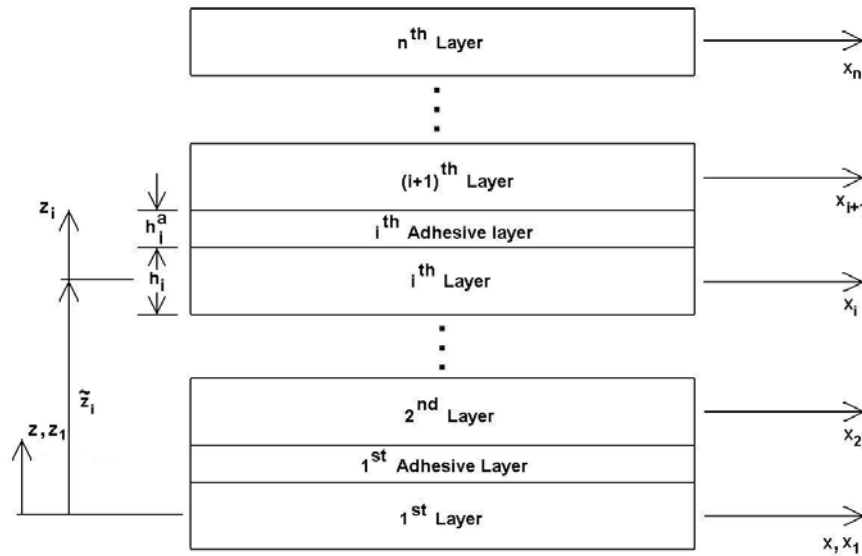

Figure 2.1. Definition of coordinate axes and layer thicknesses for n-layered plate. Similar figure may be drawn for y-z plane.
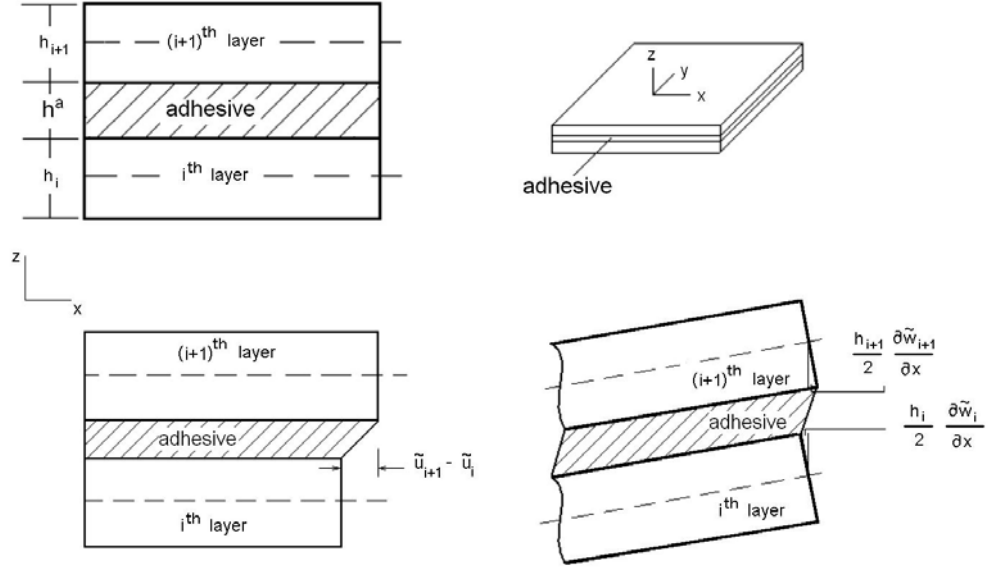
Figure 2.2. Geometry of the adhesive layer deformation.

Energy expressions for a multi-layer system bonded together, as shown in Figure 2.1 and Figure 2.2 are obtained below. The layers may be made of a piezoelectric, or a non-piezoelectric material. The total kinetic energy T, and strain energy U, of the system is the sum of the corresponding energies of individual layers. Kinetic energy of the system does not contain terms from the adhesive layer, since its mass is neglected. Thus,

$$T = \sum_{i=1}^{m} T_i^p + \sum_{j=1}^{n} T_j^n \tag{2.1}$$

$$U = \sum_{i=1}^{m} U_i^p + \sum_{j=1}^{n} U_j^n + \sum_{k=1}^{p} U_k^a \tag{2.2}$$

where subscripts refer to the respective layer and superscripts p, n, and a, indicate piezoelectric, non-piezoelectric and adhesive layers.

Using Classical Plate Theory assumptions and employing coordinate system given in Figure 2.1, displacements of the non-adhesive layers may be written as;

13

$$u_i(x_i, y_i, z, t) = \widetilde{u}_i(x_i, y_i, t) - \frac{\partial \widetilde{w}_i(x_i, y_i, t)}{\partial x_i} z_i \tag{2.3}$$

$$v_i(x_i, y_i, z, t) = \widetilde{v}_i(x_i, y_i, t) - \frac{\partial \widetilde{w}_i(x_i, y_i, t)}{\partial y_i} z_i \tag{2.4}$$

$$w_i(x_i, y_i, t) = \widetilde{w}_i(x_i, y_i, t) \tag{2.5}$$

In the above expressions, '~' refers to mid-plane properties. Thus, $\widetilde{u}_i, \widetilde{v}_i, \widetilde{w}_i$ indicate the deformations of the mid-planes. It is assumed that the mid-planes of the individual layers are parallel to each other. For this reason, individual layer coordinates (x_i, y_i, z_i) are replaced by a common coordinate system (x, y, z). Then the displacements may be written as;

$$u_i(x, y, z, t) = \widetilde{u}_i(x, y, t) - \frac{\partial \widetilde{w}_i(x, y, t)}{\partial x}(z - \widetilde{z}_i) \tag{2.6}$$

$$v_i(x, y, z, t) = \widetilde{v}_i(x, y, t) - \frac{\partial \widetilde{w}_i(x, y, t)}{\partial y_i}(z - \widetilde{z}_i) \tag{2.7}$$

$$w_i(x, y, t) = \widetilde{w}_i(x, y, t) \tag{2.8}$$

2.2.2. Strain Energy of the Adhesive Layer

Adhesive layer strains may be obtained considering two separate deformation mechanisms as shown in Figure 2.2 An analytical derivation of the strains is presented below.

The linear deformations of the adhesive layers are written in terms of the deformations of the adjacent structural layers. Thus,

$$u_i^a = u_i^{top} + \left(u_{i+1}^{bottom} - u_i^{top}\right)\frac{z - z_i^{top}}{h_i^a} \tag{2.9}$$

$$v_i^a = v_i^{top} + \left(v_{i+1}^{bottom} - v_i^{top}\right)\frac{z - z_i^{top}}{h_i^a} \tag{2.10}$$

$$w_i^a = w_i^{top} + \left(w_{i+1}^{bottom} - w_i^{top}\right)\frac{z - z_i^{top}}{h_i^a} \tag{2.11}$$

where superscripts '*top*' and '*bottom*' refer to the top or bottom surface of the related layer. For example,

$$u_i^{top} = \tilde{u}_i - \frac{\partial \tilde{w}_i}{\partial x} \frac{h_i}{2}$$

(2.12)

$$u_{i+1}^{bottom} = \tilde{u}_{i+1} + \frac{\partial \tilde{w}_{i+1}}{\partial x} \frac{h_{i+1}}{2}$$

(2.13)

and,

$$z_i^{top} = \tilde{z}_i + \frac{h_i}{2}$$

(2.14)

On the other hand, since transverse displacement is independent from the vertical coordinate;

$$w_i^{top} = w_i^{bottom} = \tilde{w}_i$$

(2.15)

Using these displacements, shear strains in the ith adhesive layer may be written. For example,

$$\gamma_{zx(i)}^a = \frac{\partial u_i^a}{\partial z} + \frac{\partial w_i^a}{\partial x}$$
$$= \left(\frac{\tilde{u}_{i+1} - \tilde{u}_i}{h_i^a} \right) + \frac{h_i}{2h_i^a} \frac{\partial \tilde{w}_i}{\partial x} + \frac{h_{i+1}}{2h_i^a} \frac{\partial \tilde{w}_{i+1}}{\partial x} + \left[\frac{\partial \tilde{w}_i}{\partial x} + \left(\frac{\partial \tilde{w}_{i+1}}{\partial x} - \frac{\partial \tilde{w}_i}{\partial x} \right) \left(\frac{z - z_i^{top}}{h_i^a} \right) \right]$$

(2.16)

In the above expression the terms given inside the square bracket are comparatively small since adherends are much thicker than the adhesive layers. For this reason it is neglected in this study. Then,

$$\gamma_{zx(i)}^a \cong \frac{1}{h_i^a} \left(\tilde{u}_{i+1} - \tilde{u}_i + \frac{h_i}{2} \frac{\partial \tilde{w}_i}{\partial x} + \frac{h_{i+1}}{2} \frac{\partial \tilde{w}_{i+1}}{\partial x} \right)$$

(2.17)

similarly,

$$\gamma^{a}_{yz(i)} \cong \frac{1}{h^{a}_{i}} \left(\tilde{v}_{i+1} - \tilde{v}_{i} + \frac{h_{i}}{2} \frac{\partial \tilde{w}_{i}}{\partial y} + \frac{h_{i+1}}{2} \frac{\partial \tilde{w}_{i+1}}{\partial y} \right) \tag{2.18}$$

and finally the normal strain in the ith adhesive layer may be written as,

$$\varepsilon^{a}_{z(i)} = \frac{\partial w^{a}_{i}}{\partial z} = \frac{\tilde{w}_{i+1} - \tilde{w}_{i}}{h^{a}_{i}} \tag{2.19}$$

The strain energy for a single adhesive layer may be written as:

$$U^{a} = \frac{1}{2} \int_{V^{a}} \left(\sigma^{a}_{z} \varepsilon^{a}_{z} + \tau^{a}_{zy} \gamma^{a}_{zy} + \tau^{a}_{zx} \gamma^{a}_{zx} \right) dV \tag{2.20}$$

2.2.3. Formulation of the Piezoelectric Layer

Linear constitutive relation in principal material coordinates of a piezoelectric layer poled in the thickness direction for isothermal case are [23],[47];

$$\{\sigma\} = \left[Q^{E} \right] \{\varepsilon\} - \left[e \right]^{T} \left\{ E^{f} \right\} \tag{2.21}$$

$$\{d\} = \left[P^{\varepsilon} \right] \left\{ E^{f} \right\} + \left[e \right] \{\varepsilon\} \tag{2.22}$$

where, $\{\sigma\}$, $\{\varepsilon\}$, and $\{d\}$ are the stress, strain and electric displacement vectors, $[Q^{E}]$ is plane stress reduced stiffness matrix measured at constant electric filed, $[e]$ is the piezoelectric coefficient matrix, $[P^{\varepsilon}]$ is the permitivity matrix measured at constant strain, $\{E^{f}\}$ is the vector of electric fields. This is the e-form of the piezoelectric equations [47]. When piezoelectric plate is poled in the thickness direction, it becomes a transversely isotropic material. Together with the plane stress assumptions, matrices in Equation (2.21) and (2.22) become,

$$[e] = \begin{bmatrix} 0 & 0 & 0 \\ 0 & 0 & 0 \\ e_{31} & e_{31} & 0 \end{bmatrix} \quad [P^{\varepsilon}] = \begin{bmatrix} P_{11} & P_{12} & 0 \\ P_{21} & P_{22} & 0 \\ 0 & 0 & P_{33} \end{bmatrix} \tag{2.23}$$

$$[Q^{E}] = \begin{bmatrix} Q_{11} & Q_{12} & 0 \\ Q_{12} & Q_{11} & 0 \\ 0 & 0 & Q_{66} \end{bmatrix} \quad Q_{11} = \frac{E_{1}}{1 - v_{12} v_{21}} \quad Q_{12} = \frac{v_{12} E_{2}}{1 - v_{12} v_{21}}$$

16

$$Q_{22} = \frac{E_2}{1 - \nu_{12}\nu_{21}} \quad Q_{66} = \frac{Q_{11} - Q_{12}}{2} = G_{12} \tag{2.24}$$

where E_1, E_2, G_{12} are the modulus of elasticity and rigidity, while ν_{12}, ν_{21} are the Poisson's ratios, and,

$$\{\sigma\} = \{\sigma_1 \quad \sigma_2 \quad \sigma_6\}^T \quad \{\varepsilon\} = \{\varepsilon_1 \quad \varepsilon_2 \quad \varepsilon_6\}^T$$
$$\{E^f\} = \{0 \quad 0 \quad E_3^f\}^T \quad \{d\} = \{d_1 \quad d_2 \quad d_3\}^T \tag{2.25}$$

If we write strain energy and electrical work using (2.21) and (2.22)

$$U^p = \frac{1}{2}\int_V \left(\{\varepsilon\}^T [Q]\{\varepsilon\} - \{\varepsilon\}^T [e]^T \{E^f\} \right) dV \tag{2.26}$$

$$W_E = \frac{1}{2}\int_V \left(\{E^f\}^T [P^\varepsilon]\{E^f\} + \{E^f\}^T [e]\{\varepsilon\} \right) dV \tag{2.27}$$

The electric field can be thought of as the gradient of the electrical potential field [48],

$$\{E^f\} = -\{\nabla\} \bullet \{V\} \tag{2.28}$$

If we consider V_3^p as only potential difference applied, then second term in (2.26) may be written as,

$$U_2^p = \frac{e_{31} V_3^p}{2} \int_\Omega (\varepsilon_1 + \varepsilon_2) \, dx\,dy \tag{2.29}$$

Similarly,

$$W_E = \frac{1}{2}\int_\Omega \left[\frac{P_{33}}{h^p} \left(V_3^p\right)^2 - e_{31} V_3^p \left(\varepsilon_1 + \varepsilon_2\right) \right] dx\,dy \tag{2.30}$$

In the classical plate theory, linear strains can be written in terms neutral plane strains ($\tilde{\varepsilon}_1, \tilde{\varepsilon}_2$) (in this case mid-plane as well), and curvatures (κ_1, κ_2).

$$\varepsilon_1 = \tilde{\varepsilon}_1 - z\kappa_1$$
$$\varepsilon_2 = \tilde{\varepsilon}_2 - z\kappa_2 \tag{2.31}$$

Then,

17

$$W_E - U_2^p = \frac{1}{2}\frac{P_{33}}{h^p}\left(V_3^p\right)^2 \int_\Omega dx\,dy - e_{31}V_3^p \int_\Omega \left(\widetilde{\varepsilon}_1 + \widetilde{\varepsilon}_2\right)dx\,dy \qquad (2.32)$$

and,

$$\begin{bmatrix} \widetilde{\varepsilon}_1 \\ \widetilde{\varepsilon}_2 \end{bmatrix} = [R]\begin{bmatrix} u \\ v \end{bmatrix} \qquad (2.33)$$

It is interesting to observe that the piezoelectric contribution to the energy, Equation (2.32), does not contain any out of plane deformations (i.e. w), which is a fundamental difference of the flexible bonding formulation proposed in this manuscript from the equivalent single layer formulation.

2.3. FINITE ELEMENT DISCRETIZATION

For in-plane deformations (u,v) linear Lagrange interpolation functions, and for the transverse deformation (w), conforming Hermite type interpolation functions are employed in the finite element formulation [23]. The elements are rectangular, and have four nodes in each layer. Thus for an n-layered plate, the element has $4n$ nodes as shown in Figure 2.3. In Figure 2.4, the rectangular elements and nodes of a two-layer plate system is depicted. The interpolating functions require the following degrees of freedom to be specified at each node: $\{u,\ v,\ w,\ w_{,x},\ w_{,y},\ w_{,xy}\}$. The strain energies of the non-piezoelectric layers, piezoelectric layers, and the adhesive layers shall all be included in the formulation of an n-layered system.

One may use a variational approach or Lagrange's equations to obtain the element matrices. The derivation of mass and stiffness matrices is quite straightforward and may be found in textbooks on finite elements [23]. Here the contribution of the adhesive layer to the global stiffness matrix as well as actuator and sensor matrices will be presented.
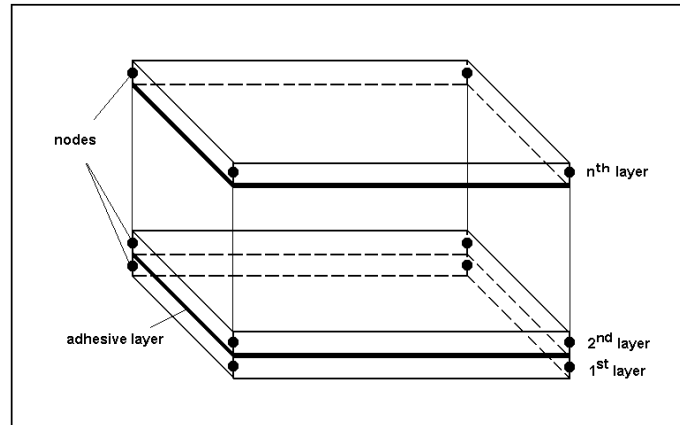
18

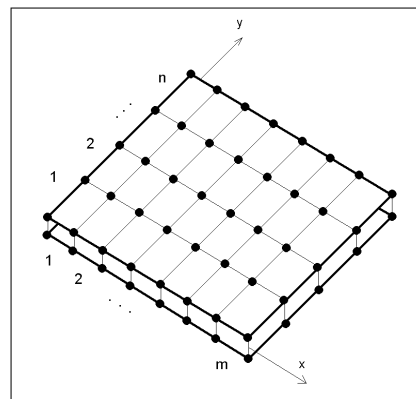Figure 2.3. Multilayered adhesively bonded plate element with four node at each layer

Figure 2.4. Two layer, adhesively bonded plate system finite element model using four node elements.

2.3.1. Effect of the Adhesive Layer to the Global Stiffness

The adhesive layer is treated as an isotropic material. Then, using equations from (2.17) to (2.20), together with the constitutive relations, the strain energy of the adhesive layer may be expressed in terms of the displacements of the upper and lower layers. In addition these displacements are interpolated from nodal degrees of freedom.

$$\{u \quad v \quad w\}^{T} \cong [\Theta]\{\Delta\} \tag{2.34}$$

Where, matrix $[\Theta]$ contains the interpolation functions. Then, the stiffness matrix contribution of the adhesive layer for an *n* layered system may be found from:

$$K_{ij} = \frac{\partial U^a}{\partial \Delta_i \, \partial \Delta_j} \quad i = 1, 2, \ldots 24n \quad j = 1, 2, \ldots 24n \tag{2.35}$$

For example, a finite element of a three-layer system has 12 nodes, with 6 degrees of freedom at each node. Without the adhesive layer there is no coupling between the layers. Addition of adhesive layer elements to the stiffness matrix causes the coupling between layers as shown in Figure 2.5.
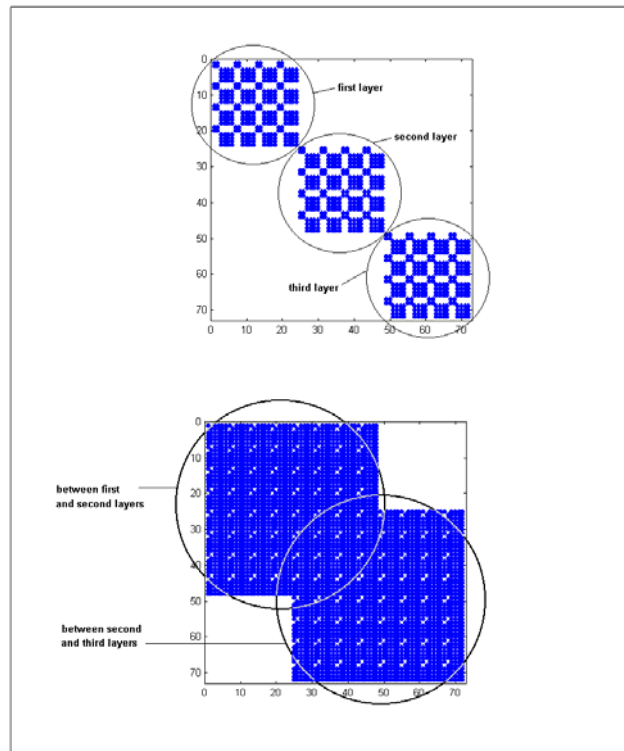

Figure 2.5. Top figure shows non-zero terms of element stiffness matrix without the adhesive layer while the bottom one shows the pattern after it is populated with terms due to adhesive layers.

2.3.2. The Piezoelectric Layer

The piezoelectric layer contributes to the global stiffness matrix. However, these layers may also be used as an actuator or a sensor. The displacement field is discretized using Lagrange interpolation functions, since piezoelectric layer contribution to an actuator or a sensor contains only in-plane displacements.

$$\begin{bmatrix} u \\ v \end{bmatrix} \cong \begin{bmatrix} \Psi \end{bmatrix}\{\Delta_0\} \tag{2.36}$$

where $\{\Delta_0\}$ is subset of $\{\Delta\}$. These strains may be expressed in terms of nodal displacements;

$$\{\varepsilon\} = \begin{bmatrix} R \end{bmatrix}\begin{bmatrix} \Psi \end{bmatrix}\{\Delta_0\} = \begin{bmatrix} B \end{bmatrix}\{\Delta_0\} \tag{2.37}$$

Then, related actuator matrix may again be obtained from Lagrange's Equation,

$$\frac{d}{dt}\left(\frac{\partial L}{\partial \dot{q}_j}\right) - \frac{\partial L}{\partial q_j} = F_j \qquad j = 1,\ldots n \tag{2.38}$$

and,

$$L = T - U + W_E \tag{2.39}$$

where, F_j are the generalized forces. Then the actuator matrix at element level is,

$$\{D^e\} = -e_{31}\int_\Omega [B]^T \begin{bmatrix} 1 & 1 \end{bmatrix}^T \, dx\,dy \tag{2.40}$$

To obtain a sensor vector, one shall consider E_3 as an independent variable and consider its variation. Another approach would be to treat E_3 as a generalized coordinate in Equation (2.38). For a single sensor layer the sensor element matrix is,

$$\{S^e\} = \frac{e_{31}\int\limits_{\Omega}[1 \quad 1][B]\,dx\,dy}{\frac{P_{33}}{h^p}\int\limits_{\Omega}dx\,dy} \qquad (2.41)$$

If the finite element is rectangular, then actuator and sensor matrices for a single layer are;

$$\{D^e\} = \frac{1}{2}e_{31}\begin{bmatrix} -b & -a & b & -a & b & a & -b & a \end{bmatrix}^T \qquad (2.42)$$

$$\{S^e\} = \frac{h^p}{2P_3\,a\,b}e_{31}\begin{bmatrix} b & a & -b & a & -b & -a & b & -a \end{bmatrix} \qquad (2.43)$$

In the above equation, a, and b are the side lengths of the rectangular finite elements. Then, the equations of motion and as well as sensor equations can be written as;

$$[M]\{\ddot{\Delta}\} + [K]\{\Delta\} = [D]\{V^{ac}\} + \{F\} \qquad (2.44)$$

$$\{V^{se}\} = [S]\{\Delta\} \qquad (2.45)$$

Where $[D]$ and $[S]$ are the global actuator and sensor matrices respectively.

2.4. RESULTS AND DISCUSSION

In this section, several cases are presented: static analysis of a square and a rectangular plates with surface bonded piezoelectric patches, a narrow plate in cylindrical bending to compare with results of Reference [49], a square plate to compare its deformation and frequencies with the ESL model, and delaminated plate to examine the effects of delamination on deformation and adhesive layer stresses.

2.4.1. Static Analysis of Rectangular Plates with Surface Bonded Piezoelectric Patches

In this section, static analysis of rectangular plates with surface bonded piezoelectric patches will be presented. Either isotropic or [0/90/0] cross-ply

symmetric laminate is considered. Material properties are listed in Table 2.1 and Table 2.2. A piezoelectric patch is bonded to the base plate as shown in Figure 2.6. The piezoelectric layer is either loaded statically or electrically, and corresponding deformations and stresses are calculated and given.

Table 2.1. Properties of the isotropic, orthotropic, piezoelectric materials and the adhesive used in the study.

Property	Isotropic Plate	[0/90/0] laminate
E_1/E_2	1	25
E_2/G_{12}	2.6	2
v_{12}	0.3	0.25
E_2/E_a (Hard Adhesive)	17.5	1
E_2/E_a (Soft Adhesive)	175	0.1
v_a	0.429	0.429
h/h_a	30	60
h/h_{PZT}	1	1
E_2/E_{PZT}	1.111	0.0635
v_{PZT}	0.28	0.28

Table 2.2. Values of the parameters.

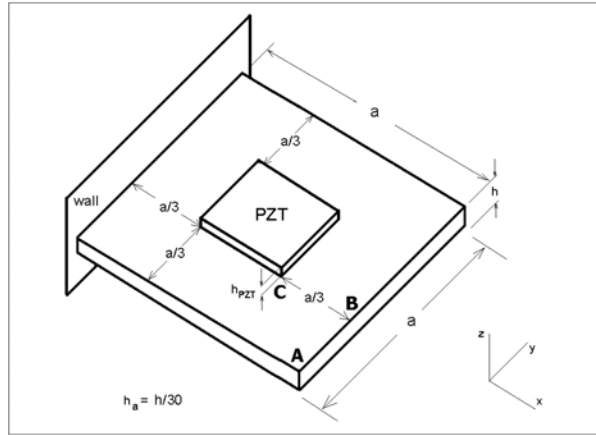| Parameter	Value
q_0	1 N/mm
E (isotropic)	70000 Mpa
E_1	100000 Mpa
h_a	0.1 mm
a	300 mm
e_{31}	0.01134 (N/Vmm)
V	200 V

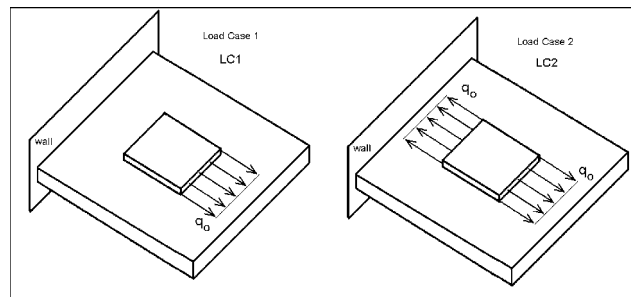Figure 2.6. Geometry of the plate and monitoring points A, B and C.

Figure 2.7 Two load cases: Load Case 1 (LC1), and Load Case 2 (LC2).

Patch Loaded with Distributed in Plane Forces

To understand the convergence properties of the finite element formulation, a piezoelectric patch, bonded on a cantilever plate, is loaded with distributed forces. Two loading cases are considered (Figure 2.7). In Loading Case One (LC1) the patch is loaded only on one side. In the second loading case, the patch is loaded symmetrically on opposite sides. The patch-plate system is discretized using rectangular finite elements. For presentation purposes, the out of plane deformations are made non-dimensional using,

$$\overline{w} = w\left(\frac{E_2\,h^3}{a^3\,q_0}\right)10^4 \qquad (2.46)$$

The non-dimensional out of plane deformation obtained at the free corner (corner 'A' shown in Figure 2.6) of the plate when it is loaded according to LC1 is calculated for 3X3 to 15X15 mesh. The solutions for a system bonded using soft adhesive and hard adhesive are given in Figure 2.8. The deformation at the free corner (corner 'A') of the plate is also calculated for LC2 as well. These latter results are given in Figure 2.9. If convergence of the two load cases are compared it may be seen that LC1 converges with fewer elements than LC2. For example, the difference between the transverse displacements at point A for a 12x12 mesh and a 15x15 mesh (hard adhesive) is less than 0.03 percent for LC1. On the other hand, for LC2, this difference is 0.7 percent. Similar behavior may be observed for the system bonded using a soft adhesive.
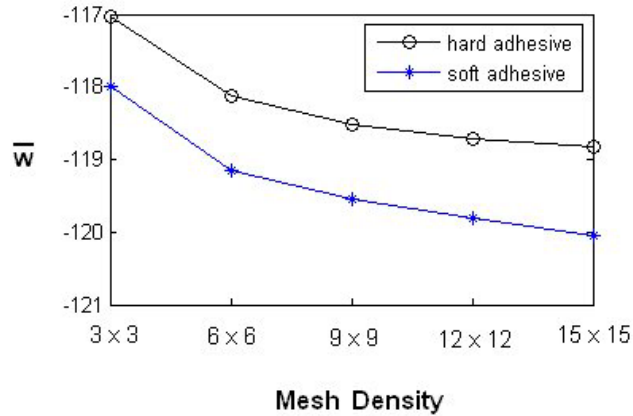

Figure 2.8. The non-dimensional transverse displacement of the corner of the free edge of the isotropic plate when plate is subjected to LC1.

It is also interesting to compare the deformation results obtained for hard adhesive, and soft adhesive cases. For example, in LC1, the difference in deformation values at point A, calculated using 15x15 mesh is about 1.08 percent. However for LC2, this difference rises to 14.2 percent. These results may be explained considering the transmission of the forces from the patch to the base plate through the adhesive layer. In Figure 2.10 the mechanism of one-dimensional loading is drawn. The top loading is similar to LC1 where the bottom loading is similar to LC2. In the top loading the force, F, must be balanced with the distributed shear forces and distributed moments acting on the bottom surface

of the patch. The main source of deformation for the LC1 is the bending moment. On the other hand the only source of deformation for LC2, is the distributed shear stress, which is closely related to the adhesive layer properties. For example, if the adhesive is rigid, there will be no distributed shear force acting on the base plate. Due to this reason the adhesive layer properties are more important in the LC2.
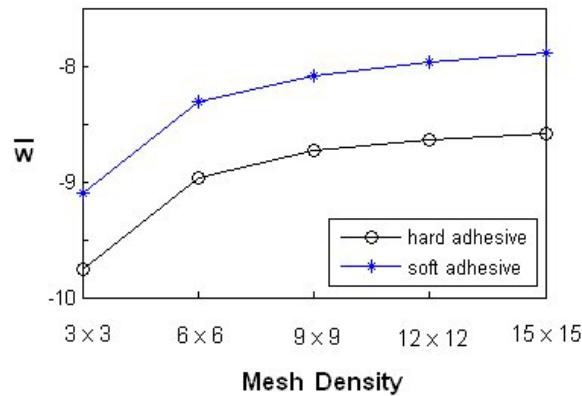

Figure 2.9. The non-dimensional transverse deformation of the corner of the free edge of the isotropic plate when plate is subjected to LC2.
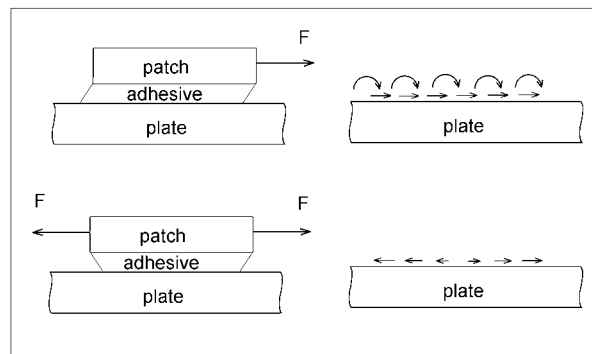

Figure 2.10. Transmission of the load from patch to the base plate.

The last observation from Figure 2.8 and Figure 2.9 would be the way finite element solution converges. When we increase the number of finite elements used the calculated deformation increases, in LC1 case. Which is just the opposite for LC2. This situation may be confusing since stiffness should decrease

with increasing number of elements. However, this decrease in deformation for LC2 is due to better representation of force transmission with increasing finite elements. From the above discussion, two conclusions may be made:

- For LC2 type of loading, adhesive properties has important bearing on response of the structure. Thus, the structure with hard adhesive deforms more.

- Denser mesh is necessary for LC2 type of loading to better simulate the shear force transmission from the patch to the base plate.

Electrically Loaded Piezoelectric Patch

In this section static response of a plate with a piezoelectric patch loaded electrically is examined. For this purpose, the displacements and stresses are made non-dimensional using (numerical values of the parameters are given in Table 2.1 and Table 2.2),

$$\overline{w} = \frac{w}{e_{31}V}\left(\frac{E_2\,h^3}{a^3}\right)10^3 \tag{2.47}$$

$$\overline{\sigma} = \frac{\sigma\,h^2}{a\,e_{31}V}10^6 \tag{2.48}$$

In Figure 2.11, the calculated non-dimensional deformed shape of an isotropic square plate, as a result of an electric filed applied to the bonded piezoelectric patch is plotted. The location of the patch may easily be guessed from this deformed shape.

Results of adhesively bonded finite element model are compared with the MSC/NASTRAN model results to verify the formulation as well as the computer code developed. The MSC/NASTRAN model is constructed using solid (brick) elements, and the adhesive layer is neglected. Therefore, very hard adhesive layer is used in MLP-FAB model to minimize the effect of the adhesive layer on the deformation results. Again a cantilever square plate with a central piezoelectric patch (Figure 2.6) is used. The nodal deformations along the line running from the center of the wall support to the center of the free edge are plotted in Figure 2.12. The base plate is an isotropic plate, and both the plate and the patch have the same thickness. It may be seen from Figure 2.12 that the

27

results are in very good agreement. However, during the study it is found that the agreement deteriorates when base plate and patch thicknesses differ considerably.
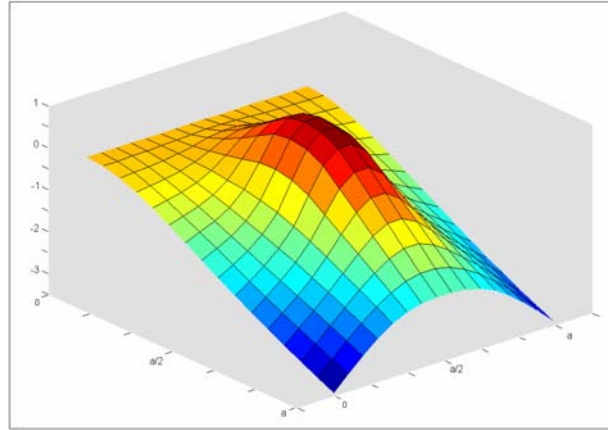

Figure 2.11 Deformed shape for 18x18 mesh FE model of plate when voltage is applied on PZT patch.
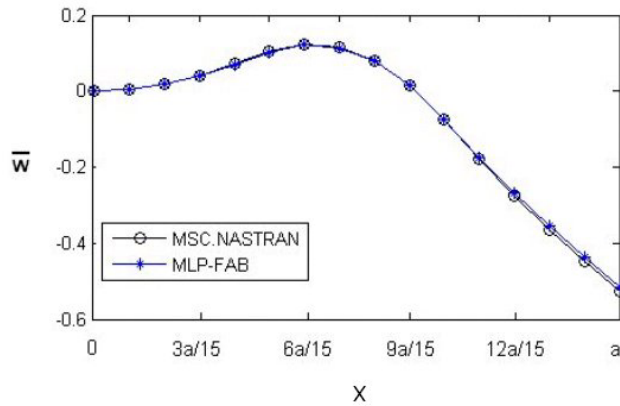

Figure 2.12. Comparison the results of MSC/NASTRAN model constructed using brick elements, and the results of the flexible bonding model. The nodal deformations of the centerline, running from the wall support to the free edge are plotted.

When a potential difference is applied to a piezoelectric patch poled in the thickness direction, a tensile (or compressive) distributed force is applied to the patch (Figure 2.13). Although, in this case, the created load due to the in plane deformation of the patch is in both directions, the shape of the loading is similar to

28

the loading of LC2. Therefore above conclusions given for LC2 are valid when the loading is made through an electrical field.
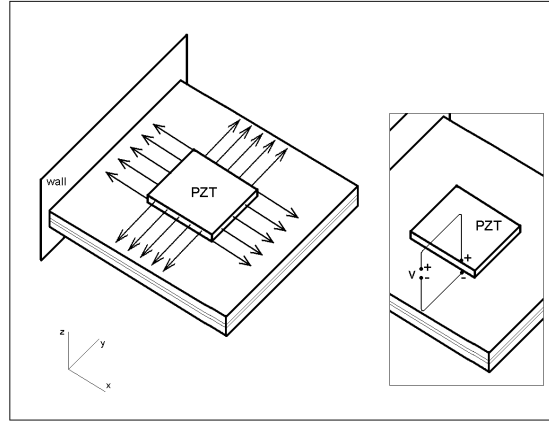

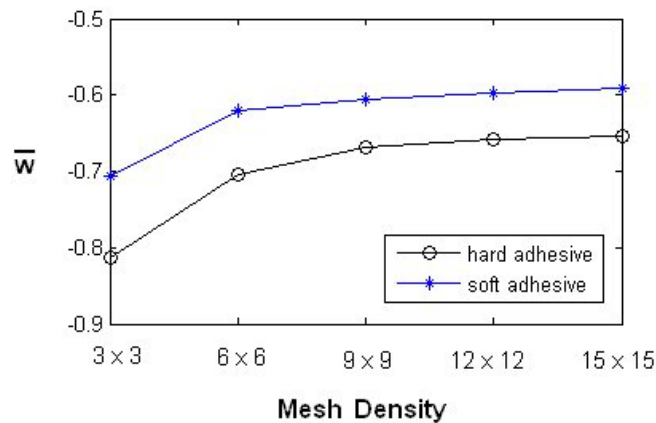Figure 2.13. Application of the electric field to the piezoelectric patch and resulting forces

Figure 2.14. Non-dimensional transverse displacement of the isotropic square plate at corner point of the free edge when voltage is applied on PZT patch.

In Figure 2.14 and Figure 2.15 non-dimensional transverse displacements at corner point of the free edge (point 'A' in Figure 2.6) when an electrical field is applied to a piezoelectric patch are given. The base plates are isotropic and cross-ply symmetric laminate, respectively. In both cases plates bonded to the piezoelectric patch with a hard adhesive deforms 10 to 12 percent more than the plates bonded with a soft adhesive. A 15x15 mesh in both cases gives pretty

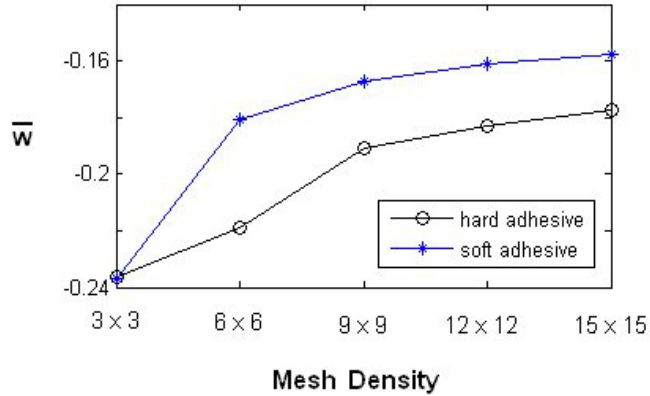good results. More finite elements shall undoubtedly increase the solution accuracy.

Figure 2.15. Non-dimensional transverse displacement of the [0/90/0] square plate at corner point of the free edge when voltage is applied on PZT patch
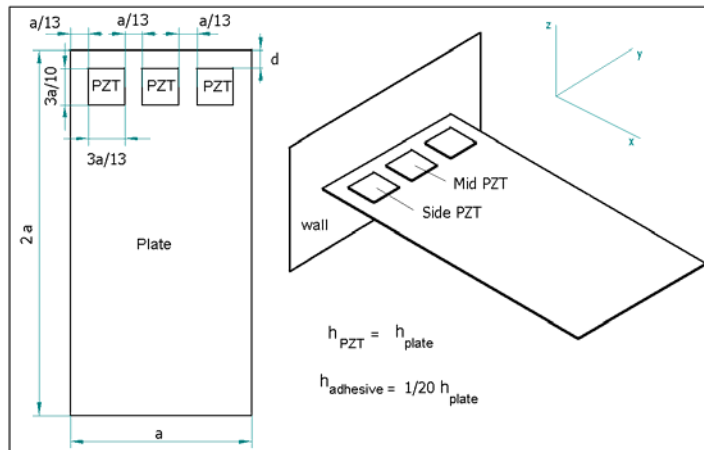

Figure 2.16. Geometry and location of the piezoelectric patches and base plate used in the stress calculation studies

In this part of the study, the stresses created, by a piezoelectric patch, on the base plate is investigated. The base plate is an orthotropic plate where the fiber direction coincides with the 'x' axis (Figure 2.16). The material properties are given in Table 2.1 and Table 2.2. Plates are supported using two different boundaries. The first one is clamped at '$x=0$' edge free on other three edges

(CFFF). The second one is simply supported at '$x = 0$' and '$x = 2a$', and free along the two remaining edges (SSFF). Three different piezoelectric patches are bonded on the plate (Figure 2.16), and the same electrical field is applied to all three patches. Stresses at the mid plane of the plate at the points directly below the center of the patches bonded above them are calculated. Initially, the patches are placed at $d = a/10$ from the top support (i.e. $x = 0$, Figure 2.16). All three patches are moved together towards the opposite edge ($x = 2a$). The calculated stresses are plotted in figures Figure 2.17 to Figure 2.22.
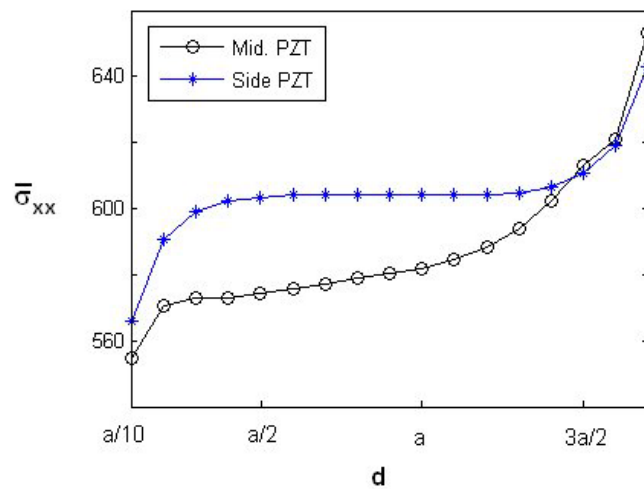

Figure 2.17. Normal stress, σ_{xx}, on the mid plane of the plate at a point below the center of the piezoelectric patch where, d, is the distance of the patch from the wall (CFFF)

For CFFF boundary conditions, normal stresses (σ_{xx}, and σ_{yy}) increase as the patch is moved from clamped end to the free end (Figure 2.17-Figure 2.19). The stresses below the side piezoelectric patch are larger than those generated below the middle piezoelectric patch. The shear stress, τ_{xy}, is comparatively small, and displays a more symmetric behavior as the patch moves to the free edge.
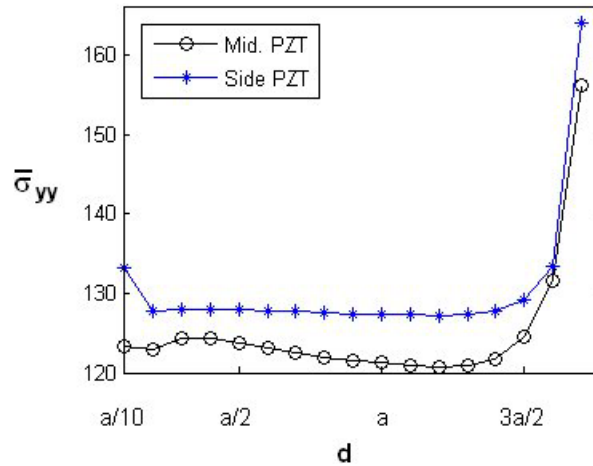
Figure 2.18. normal stresses, σ_{yy}, on the mid plane of the plate at a point below the center of the piezoelectric patch where, d, is the distance of the patch from the wall (CFFF)
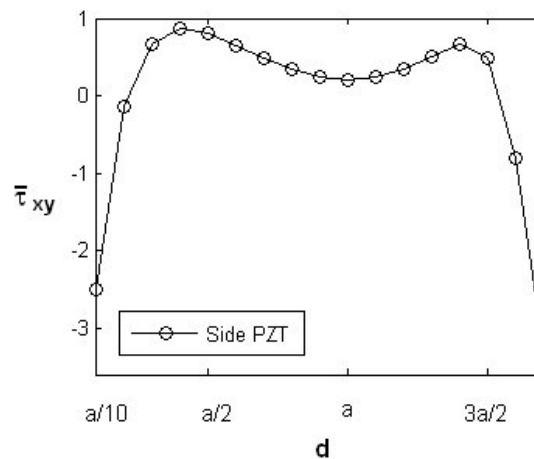

Figure 2.19. Shear stress, τ_{xy}, at the mid plane of the plate below the center of the piezoelectric patch where, d, is the distance of the patch from the wall (CFFF)

The stresses calculated for the plate with SSFF boundary condition are plotted in Figure 2.20-Figure 2.22. Both the normal stresses and shear stresses display symmetry as the patch moves from one support to the other support. Again the mid plane stresses below the center of the side piezoelectric patch is larger than the center piezoelectric patch. It may be observed from the figure that normal stresses obtained from a plate with SSFF boundary condition are smaller than the ones obtained from the plate with CFFF boundary condition. The shear

32

stress again gives a symmetric pattern as patches are moved from one support to the other as expected. However, these stresses obtained are higher than those obtained in the CFFF case.
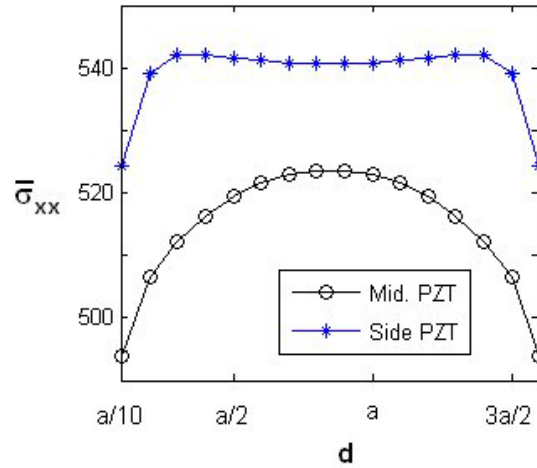

Figure 2.20. Normal stress, σ_{xx}, on the mid plane of the plate at a point below the center of the piezoelectric patch where, d, is the distance of the patch from the '$x = 0$' edge (SSFF)

Figure 2.21. Normal stress, σ_{yy}, on the mid plane of the plate at a point below the center of the piezoelectric patch where, d, is the distance of the patch from the '$x = 0$' edge (SSFF)
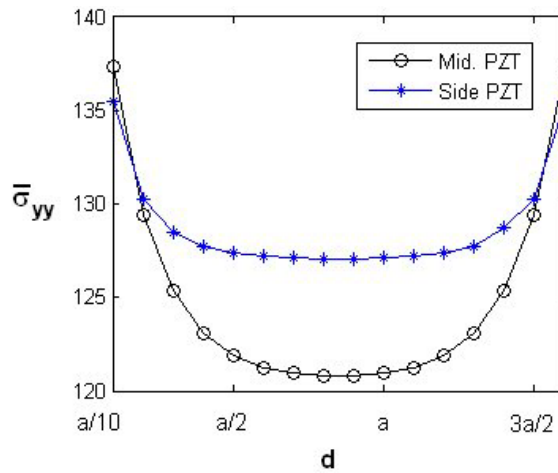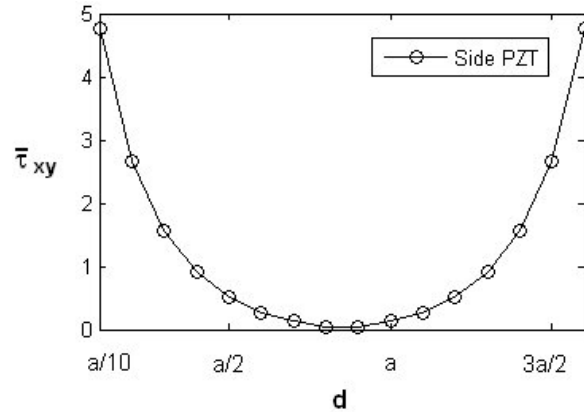
Figure 2.22 Shear stress, τ_{xy}, at the mid plane of the plate below the center of the piezoelectric patch where, d, is the distance of the patch from the from the '$x=0$' edge (SSFF)

Summary

In this section, two different case studies are presented. In the first case study, single piezoelectric patch is placed in the middle of the cantilevered square plate. The static response of the base plate under different loading cases is investigated. It is observed that response of the structure is very sensitive to adhesive layer properties. It is also seen that denser mesh is required when loading is similar to the loading generated by an electrically loaded piezoelectric patch. Also given are the stresses at the mid plane of the supporting plate caused by an electrically loaded piezoelectric patch. It is found that side patches cause more stress at the base plate than the middle patch, and cantilever plate experiences more stress at the mid plane below the center of the piezoelectric patch than the simply supported plate.

2.4.2. Cantilever Plate in Cylindrical Bending

Robbins et al., [49] investigated the effect of various modeling approaches to the deformation of beams. They have used finite element models based on classical beam theory (CBT), first order shear deformable beam theory (SDBT), and multi layered beam theories (MLBT1 and MLBT2). The deformations obtained on the tip of the beam using these theories are reproduced (from [49]) in Table 2.4. For comparison purposes a narrow (10 mm wide) three-layered cantilever plate, with same material properties and layer thicknesses (Table 2.3), as shown

in Figure 2.23, is considered. In order to compare results with the results from [49], a distributed edge load, which causes the cylindrical bending of the plate, and creates an equivalent actuation strain of 0.001 in PZT layer, is applied (Figure 2.24, LC1).
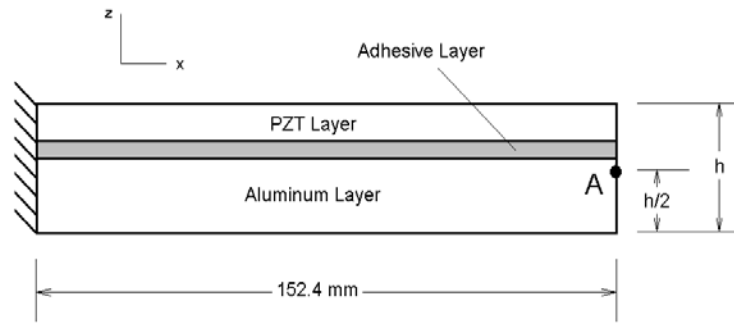

Figure 2.23. Geometry of the cantilever beam, [49].

Table 2.3. Material properties and dimensions from Reference [49].

Property	Aluminum	Adhesive	PZT
E (Mpa)	68950	6895	68950
G (Mpa)	27580	2462	27580
Thickness (mm)	15.24	0.254	1.524
Density (Mg/mm^3)	2.768 10^{-9}	-	7.640 10^{-9}

The deformation results for the multi-layered plate with flexible adhesive bonding (MLP-FAB) are presented in Table 2.4. Also presented are the deformations obtained using MSC.NASTRAN model of the narrow plate composed of brick elements. The model was created using four hexahedral elements in the thickness direction as shown in Figure 2.25. It may be observed that in the case of x-direction inplane deformation results of MLP-FAB are close to the axial deformation results CBT and SDBT results given in Robbins [49]. However, MLBT1, MLBT2 as well as MSC.NASTRAN models deformed up to 7 percent less than MLP-FAB model. It should be noted that since both the developed model and MSC.NASTRAN model have no nodes at Point A (Figure

35

2.23), displacements are interpolated from the neighboring nodes. When transverse displacements are considered, it may be observed from the table that the MLP-FAB deforms less than the other models (0.75% to 1.38%). However, this slight difference may be due to the numerical inaccuracies as well.

Table 2.4. Comparison of deformations at point A of Figure 2.23. Although, number of the elements are different for different models, convergence of the tip displacement is satisfied for MSC.NASTRAN and MLP-FAB models.

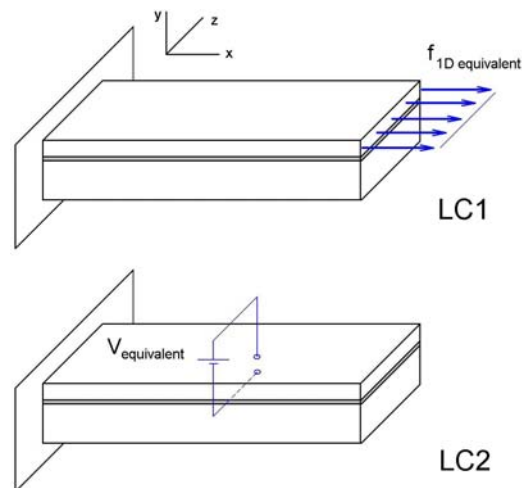|		u (mm)	w (mm)
Robbins and Reddy [49] (25×30×1 mesh)	CBT	0.01426	0.3470
	SDBT	0.01426	0.3470
	MLBT1	0.01366	0.3470
	MLBT2	0.01339	0.3465
MSC.NASTRAN (15×4×1 Solid Elements)		0.01350	0.3448
MLP-FAB (LC1, 100×1×1 mesh)		0.01432	0.3422
Difference (%) between MLP-FAB and	CBT	-0.42	1.40
	SDBT	-0.42	1.40
	MLBT1	-4.61	1.40
	MLBT2	-6.49	1.26
	Solid Model	-5.73	0.76

Figure 2.24. Equivalent tip load to create actuation strain of 0.001 (LC1), and potential difference (LC2).
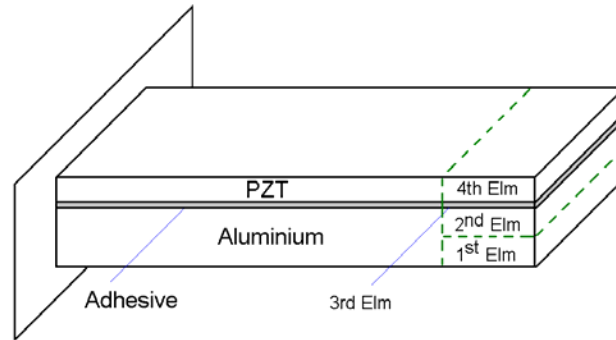
Figure 2.25. 4 elements are used in the thickness direction to form the solid model.

2.4.3. Comparison of MLP-FAB with ESL

152.4x152.4 square plate having same layer and material properties with the previous example is analyzed (Table 2.2 and Table 2.3). Deformation results are compared with the results obtained using ESL model together with NASTRAN QUAD4 elements. For this purpose equivalent loads, as shown in Figure 2.26 are used in the ESL solutions.   Displacements of two points (A and B) on the midplane as shown in Figure 2.27 are considered. The results are listed in Table 2.5. At Point A, the difference between inplane deformations is about 1% and 5% for x and y directions respectively. However at Point B, there is a very small difference between 'x' direction inplane displacements. The inplane displacements obtained in the 'y' direction are zero due to the symmetry as expected.   For transverse deformations, on the other hand, the difference was about 1% at the corner (Point A) and negligible for Point B as well. The cases with soft adhesive deformed about 1 % less than the hard adhesive. Due to the adhesive layer flexibility, forces or moments transmitted to the main structure were lower, causing lower deformation. Transverse deformations along lines at the intersection of the midplane with '$y=0$', '$y=L/2$', and '$x=L$' planes are given in Figure 2.28. In all cases the MLP-FAB model with a hard adhesive deformed less than ESL model.

37

Table 2.5. Comparison of deformations at points A and B (shown in Figure 2.27). All models are discretized by 10×10 mesh. The soft adhesive used is 10 times softer than the hard adhesive.

Location	Deformation	ESL model (MSC.NASTRAN QUAD4 Elements)	MLP-FAB (Hard Adhesive)	MLP-FAB (Soft Adhesive)
A	u (mm)	0.01121	0.01064	0.01053
	v (mm)	-0.0055	-0.0054	-0.0054
	w (mm)	-0.3307	-0.3270	-0.3223
B	u (mm)	0.01092	0.01094	0.01090
	v (mm)	0.0000	0.0000	0.0000
	w (mm)	-0.2756	-0.2758	-0.2719
		Difference (%) between MSC.NASTRAN model and MLP-FAB		
		Hard Adhesive	**Soft Adhesive**	
A	u	-5.08	-6.07	
	v	-1.82	-1.82	
	w	-1.12	-2.54	
B	u	0.18	-0.18	
	v	-	-	
	w	0.07	-1.34	

The convergence of the natural frequencies of MLP-FAB finite element model with increasing mesh number is also investigated. The changes in the first four frequencies with mesh number are given in Figure 2.29. From the figure, it may be stated that a 16x16 mesh gives rather accurate results while the difference between 14x14 mesh and 16x16 mesh is less than 0.07 % in all cases. Natural frequencies of a two-layer system modeled using MLP-FAB approach using soft and hard adhesives are compared to those of ESL model solved using MSC.NASTRAN QUAD4 elements. The first four frequencies and corresponding mode shapes are given in Table 2.6. Among these first four frequencies, maximum difference between the results is found for second natural frequency. The frequency of the second mode of MLP-FAB model is about 4.6% more than the frequency of the similar mode of ESL model, which says torsional stiffness of MLP-FAB model, is higher.
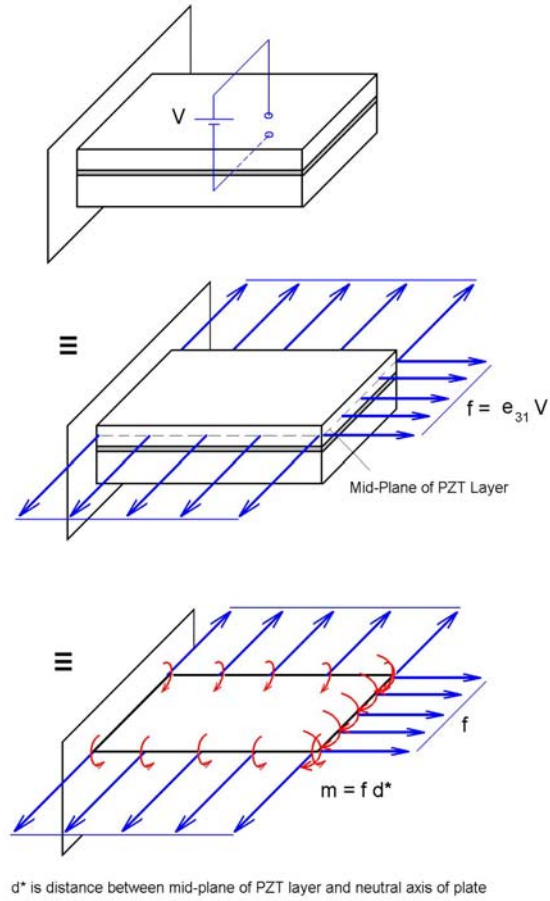
Figure 2.26. Internal forces due to applied voltage on PZT layer are converted to external distributed forces and moments for ESL model.
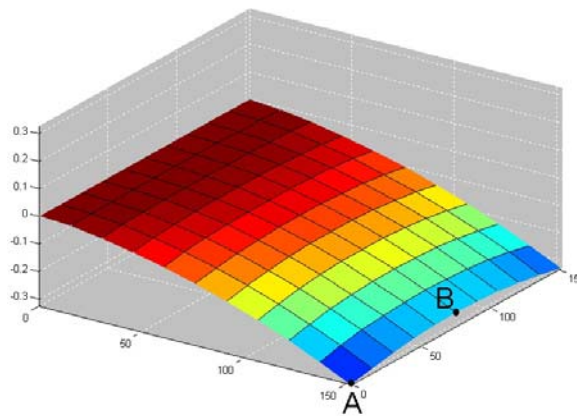

Figure 2.27. Deformed shape when sufficient voltage to cause an actuation strain of 0.001 is applied.
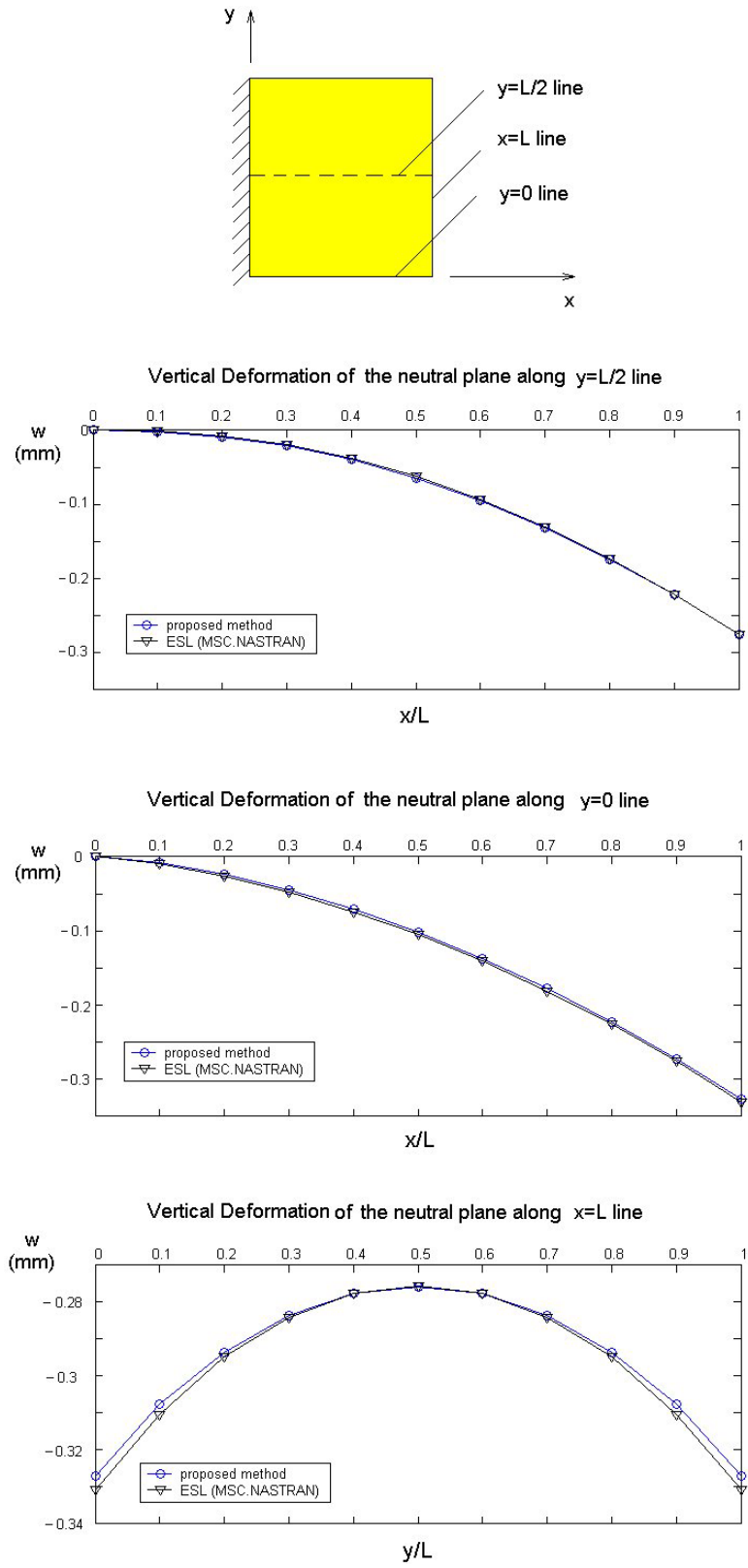
Figure 2.28. Comparison of vertical deformations of ESL and MLP-FAB with hard adhesive on lines y=L/2, y=0 and x=L.
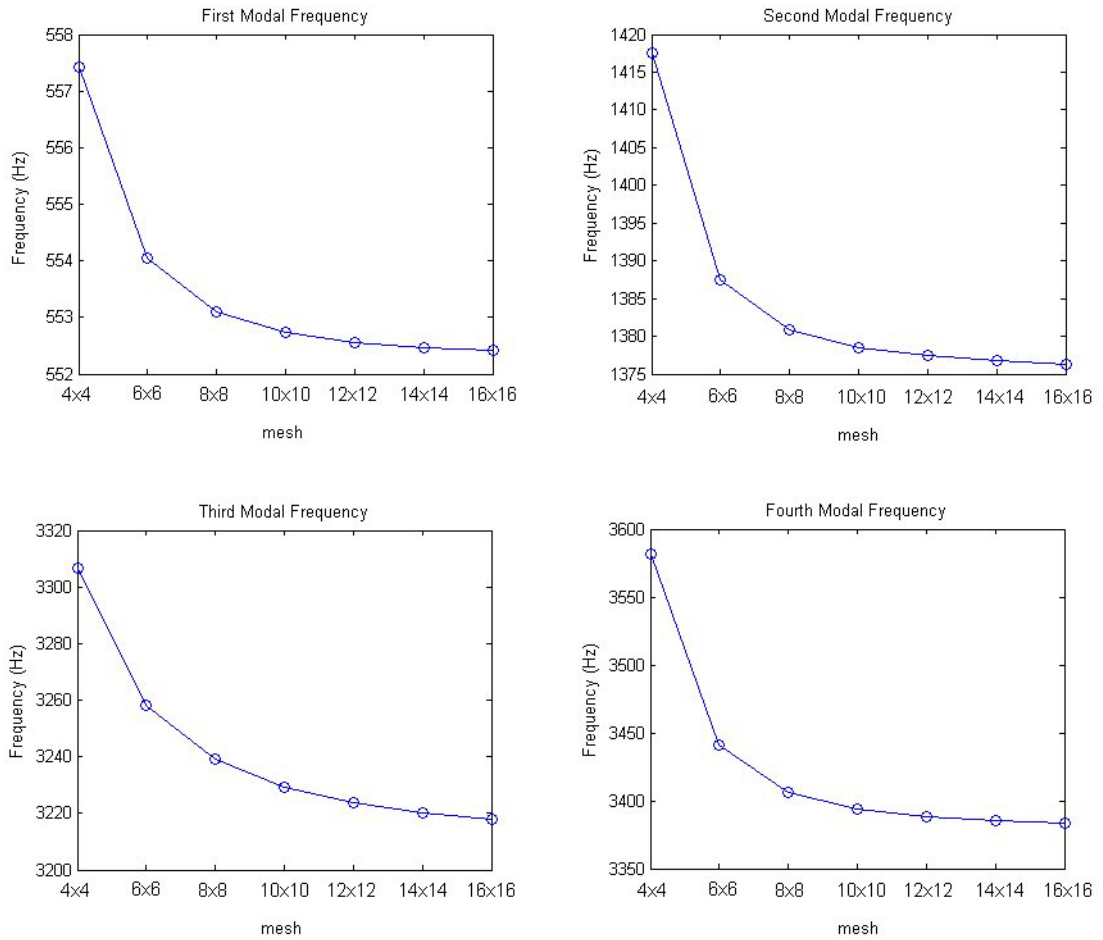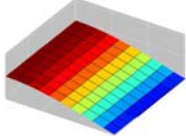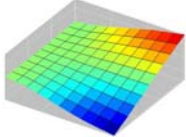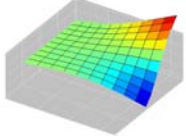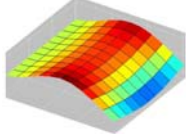
Figure 2.29. Convergence plots of first four natural frequencies with changing mesh number.

The soft adhesive used in the calculations had a ten times lower modulus of elasticity than the hard adhesive. It may be observed from the table that there is a very small difference between the hard adhesive and soft adhesive results. The mode shapes of the frequencies presented are all symmetric modes. However, it is the antisymmetric modes where substantial stretching of the adhesive layer occurs, causing difference between the frequencies of the multilayer plates constructed using soft and hard adhesives [28].

Table 2.6. Comparison of first four modal frequencies between proposed method and ESL model. Selected soft adhesive is 10 times softer than the hard adhesive. All models are discretized by 14×14 mesh.

Mode Shape	MSC.NASTRAN ESL (Hz)	MLP-FAB Hard Adhesive (Hz)	MLP-FAB Soft Adhesive (Hz)
	551.6	552.4	551.1
	1317	1377	1361
	3212	3220	3220
	3248	3385	3344

2.4.4. Stresses in Adhesive Layers and Correction for Transverse Normal Stiffness

Since, the accurate prediction of adhesive layer stresses is important for the assessment of failures, these stresses are evaluated and compared in this section. For this purpose, again the cantilever plate in cylindrical bending is employed (Figure 2.23-Figure 2.24). In Figure 2.30, shear stresses in adhesive layer are presented for both loadings (LC1 and LC2, shown in Figure 2.24). The shear stress plot of LC1 is very close to the plot given in Reference [49] for the MLBT1 formulation. However, there is a substantial difference in adhesive layer shear stress, when a potential difference sufficient to cause equal amount of strain is applied (LC2). The LC1 causes a cylindrical bending of the plate like in beam bending, while LC2 causes bending in both directions (1 and 2). Although selected geometry has very high aspect ratio, strain in width-direction due to applied voltage (LC2) still affects the shear stress.
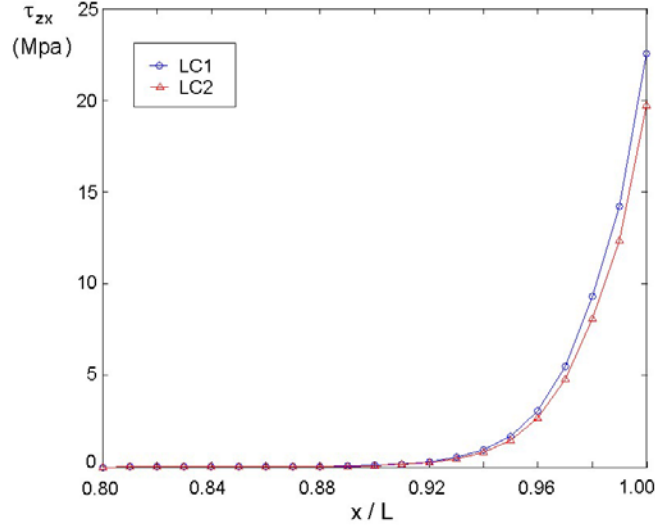
Figure 2.30. Adhesive layer shear stress τ_{zx}, near the free end of the cantilevered plate for LC1 and LC2 loadings.

The MLBT2 formulation results given in Reference [49], permits transverse normal strains predict lower stresses in the transverse normal direction. The formulation above neglects the transverse normal strains in the adherends. For this reason, the adhesive layer appears to be much stiffer in the thickness direction, causing higher normal stresses to appear. The error involved would be small as long as adhesive layer is much softer than the adherends in the thickness direction. However, when adherends are quite thick and adhesive layer elastic constants are high, the adherend stiffness may become comparable to the adhesive stiffness in the thickness direction. In this case, transverse normal strains shall be taken into account that requires the use of high order plate theories for the layers [49],[50]. Another approach would be to adjust the stiffness of the adhesive layer in the thickness direction.

For an adhesive layer of uniform thikness, the adhesive layer strain energy due to transverse normal deformation may be written as:

$$U^1 = \frac{1}{2} \int_{V^a} \left(\sigma_z^a \cdot \varepsilon_z^a \right) \cdot dV = \frac{1}{2} \int_{A^a} k_i^a (\tilde{w}_{i+1} - \tilde{w}_{i+1})^2 dA \qquad (2.49)$$

where, $k_i^a = E_i^a / h_i^a$, which may be wieved as a set of distributed normal springs attaching the upper and lower layers. Together with the adherends, the stiffness

43

of the multilayer system, may also be wiewed as a set of springs attached in series (Figure 2.31)
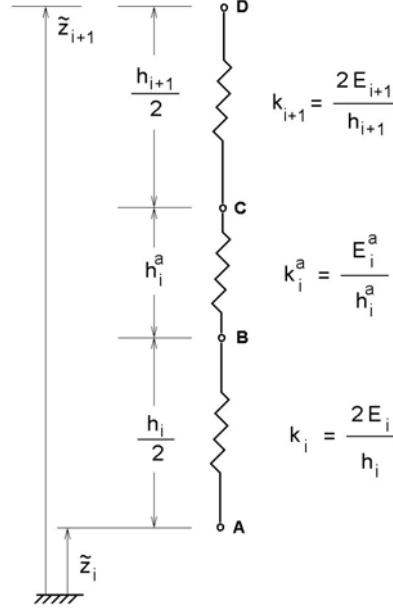
Figure 2.31. Thickness direction stiffness modeled using a series of springs between mid-planes of upper and lower layers.

Again assuming each layer has a uniform thikness, an equivalent distributed spring coefficient, and the strain energy due to thikness-wise deformation may be written as:

$$k_i^{eq} = \left(\frac{h_i}{2E_i} + \frac{h_i^a}{E_i^a} + \frac{h_{i+1}}{2E_{i+1}} \right)^{-1}$$

(2.50)

and,

$$U^1 = \frac{1}{2} \int_{A^a} k_i^{eq} (\tilde{w}_{i+1} - \tilde{w}_i)^2 \, dA$$

(2.51)

Then the transverse normal stresses become,

44

$$\sigma_{z\,(i)}^{a} = k_{i}^{eq}(\tilde{w}_{i+1} - \tilde{w}_{i})$$

$\qquad\qquad\qquad\qquad\qquad\qquad\qquad\qquad\qquad\qquad\qquad\qquad$ (2.52)

The above derivation assumes a constant normal stress between the mid-planes of the adherends. To evaluate the effects of the above formulation, the three layer narrow plate in cylindrical bending problem is modeled again in MSC.NASTRAN using solid elements. However, this time a denser mesh is employed. Thus, 100 elements in longitudinal direction, 12 elements in thickness direction and 4 elements in width direction are used. Since they are relatively thin, both adhesive and PZT layers are modeled using only one element in thickness direction. The structure is again loaded with LC1. Although the displacements obtained in MSC.NASTRAN with fine mesh are almost same as those obtained with a coarse mesh presented above, stresses are different, especially near the free edge where stress gradient is very high. The normal stress results in the adhesive layer are plotted in Figure 2.32. The stresses given in the figure are those obtained at the mid-plane of the adhesive layer. On the same figure, the transverse normal stresses predicted with MLP-FAB models with and without stiffness corrections are also given. It may be observed from the figure that, while transverse normal stress values obtained without correction are quite high (MLP-FAB), those obtained with stiffness correction (MPL-FAB corrected) are lower and they are quite close to the MSC.NASTRAN solution. In Table 2.7 numerical values of the stresses occurring at the unsupported corner ($x=L$) are given. Results in Figure 2.32 and Table 2.7 show that, suggested correction is very effective in predicting transverse normal stresses. Without the stiffness correction, normal stress in the thickness direction was about 86% higher than MSC.NASTRAN solution, while it is reduced to less than 5% with the stiffness correction. Transverse normal strains, although small, also affects the transverse shear stress. It may be seen from Figure 2.33 that transverse shear stresses are also reduced by the transverse stiffness correction. The numerical values of the maximum shear stress occurring at the free edge are listed in Table 2.7 as well. It may be observed form the table that the maximum transverse shear stress predicted by MLP-FAB with and without the stiffness correction are about 20% and 30% higher than those predicted by MSC.NASTRAN solid model.

Table 2.7. Stresses of the adhesive layer predicted by different models.

Model	Mesh	σ_z (Mpa)	τ_{zx} (Mpa)
MLP-FAB	100x1	-17.49	22.53
MLP-FAB Corrected	100x1	-9.861	20.97
MSC.NASTRAN (adhesive center)	100x12x4	-9.415	17.40
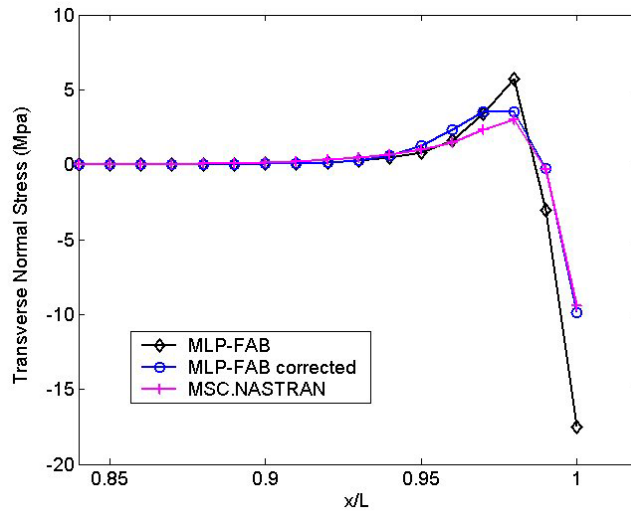
Figure 2.32. Free edge ($y = 0$) transverse normal stresses in the adhesive layer, LC1 loading.
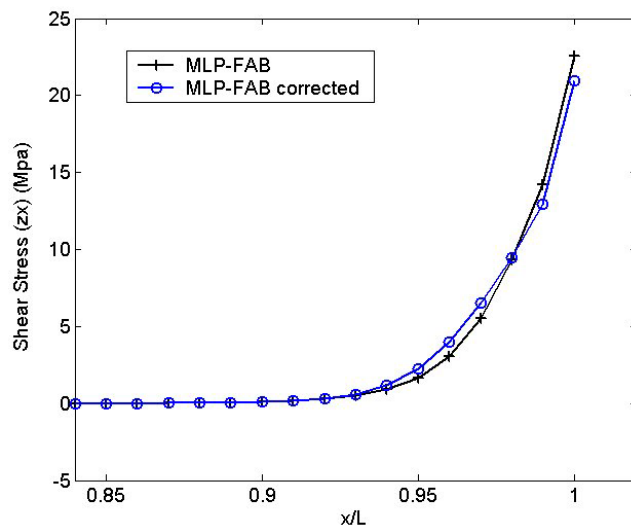
Figure 2.33. Free edge ($y = 0$) transverse shear stresses of the adhesive layer, LC1 loading.

2.4.5. Effects of Delamination on Adhesive Layer Stresses

In this section, effects of delamination on adhesive layer stresses are investigated. The selected geometry and layer properties are given in Figure 2.34, Table 2.8, and Table 2.9. Figure 2.35 shows the delaminated region. The orthotropic rectangular base plate is cantilevered from the short edge, while fiber directions are parallel to 'x' and 'y' axis. A 200 V potential difference is applied to PZT.
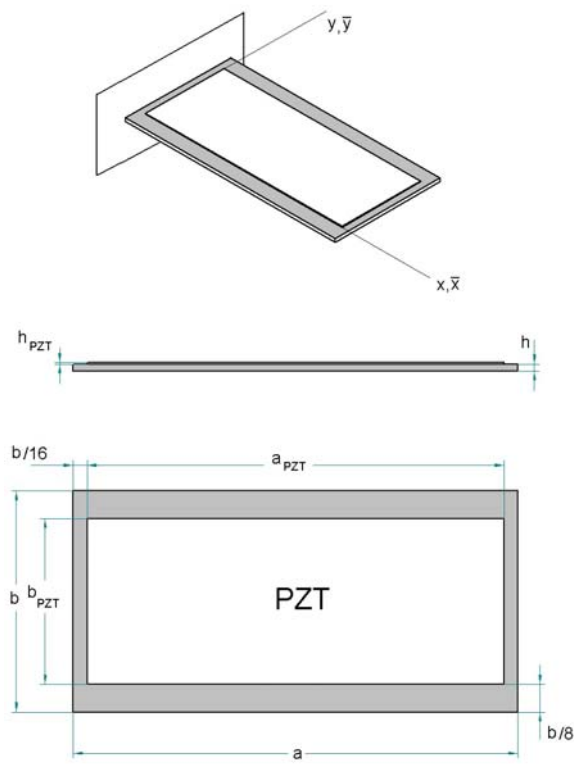
Figure 2.34. Geometry of the cantilever plate used in the delamination study.
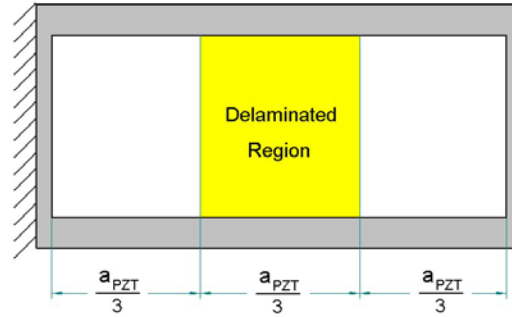
Figure 2.35. Location of the delamination region.

Table 2.8. Dimensions of the cantilever plate.

Dimensions	(mm)
a	320
b	160
a_{PZT}	300
b_{PZT}	120
h	5
h_{PZT}	1
$h_{adhesive}$	0.1

Table 2.9. Properties of the cantilever plate with an orthotropic base.

Property	Plate	Adhesive	PZT
E_1 (Mpa)	134400	400	63000
E_2 (Mpa)	10340	-	-
G_{12} (Mpa)	5000	140	24610

Using the MLP-FAB finite element model, the maximum transverse displacement found was -0.1033 mm for the fully attached case and -0.1030 mm for the delaminated case at corners of the free edge. Although, deformation results are very similar for fully attached and delaminated cases, local stresses in adhesive layer near delaminated region are quite different. Since, along the line of delamination, relative displacement of upper and lower nodes increase, adhesive strains and stresses raise as well. These results are shown in Figure

2.36 to Figure 2.39. Referring to Figure 2.34, non-dimensional coordinates and stresses, are defined as;

$$\bar{x} = \frac{x}{a_{PZT}} \qquad (2.53)$$

$$\bar{y} = \frac{y}{b_{PZT}} \qquad (2.54)$$

$$\bar{\tau} = \frac{\tau \, a_{PZT}}{e_{31} V} \qquad (2.55)$$

Figure 2.36. Comparison of $\bar{\tau}_{zx}$ in adhesive layer along $\bar{y} = 0.5$ plane of fully attached case with delaminated case, 64×16 mesh.

Figure 2.37. Zoomed in view of $\bar{\tau}_{zx}$ given in Figure 2.36.

Figure 2.36 presents the shear stress variation of the adhesive layer along the '$\bar{y} = 0.5$' plane. From the figure a sharp increase in the stresses along the edges of the piezoelectric plate is observable at '$\bar{x} = 0$' and '$\bar{x} = 1$'. Although it is not as large, there is also a sharp increase in the stresses at the delamination boundary. Note that the distributed spring model used for the adhesive layer predicts nonzero shear stresses at the boundaries. As clearly shown in Reference [26], these stresses go to zero with a very high stress gradient. Using the analytical solutions of plates, in cylindrical bending and stretching, given in Reference [26], it is verified that, stress level predicted at the boundary is close to actual maximum stress especially for hard adhesives. The shear stress $\bar{\tau}_{yz}$ of the adhesive layer is zero along the line on '$\bar{y} = 0.5$' plane due to symmetry.
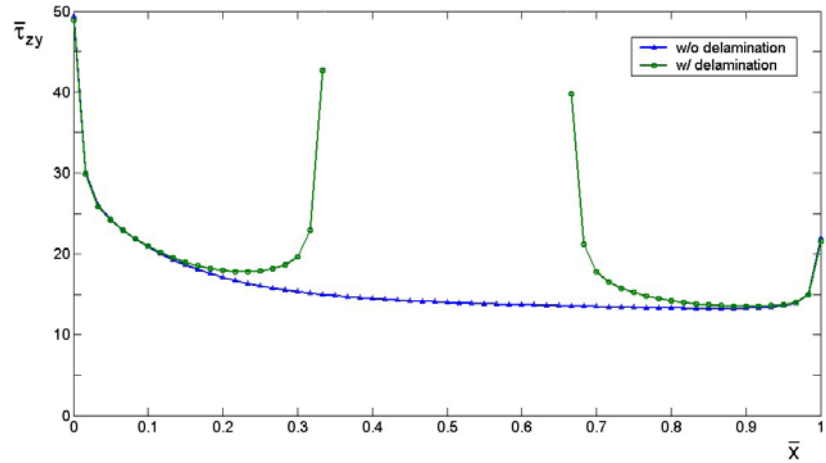
Figure 2.38. Comparison of $\overline{\tau}_{zy}$ in adhesive layer along '$\overline{y}$ = 1' plane of fully attached case with delaminated case, 64×16 mesh.
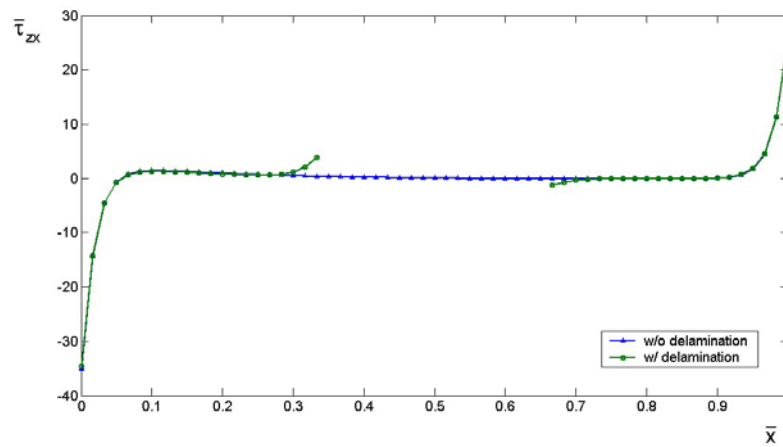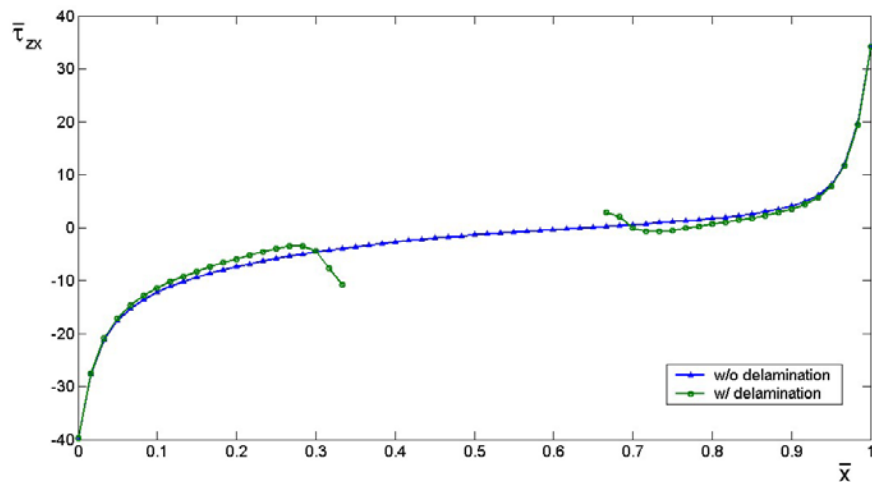

Figure 2.39. Comparison of $\overline{\tau}_{zx}$ in adhesive layer along '$\overline{y}$ = 1' plane of fully attached case with delaminated case, 64×16 mesh.
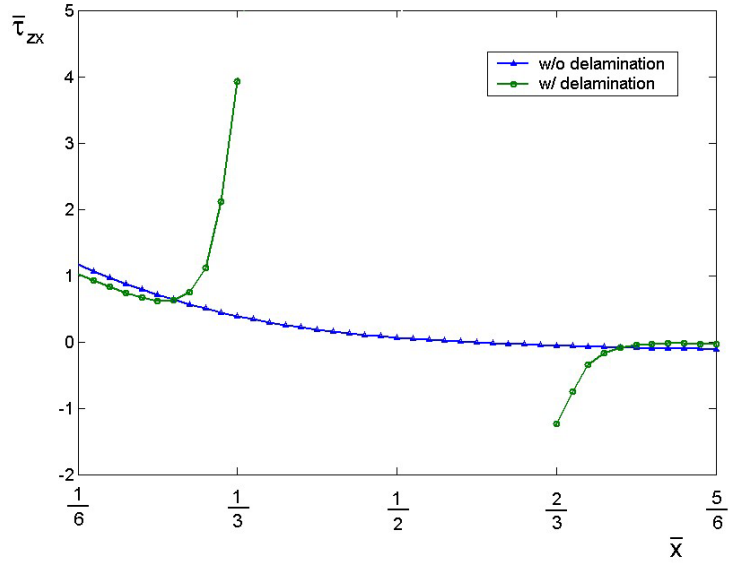
The shear stresses of the adhesive layer along the '$\overline{y}$ = 1' plane are given in Figure 2.38 and Figure 2.39. From the figures it may be observed that the level of $\overline{\tau}_{zy}$ is higher than $\overline{\tau}_{zx}$ at the delamination boundary. Comparing Figure 2.36 and Figure 2.39 it may be observed that the level of shear stresses, $\overline{\tau}_{zx}$, along the centerline ($\overline{y} = 0.5$) is less than it is along the edge ($\overline{y} = 1$) since it also deforms less as well.

51

In Figure 2.40, variation of adhesive shear stress τ_{zy} along lines parallel to the short edge (*y*-axis) at different $\bar{x}$ locations ('$\bar{x}=0$', '$\bar{x}=1/3$', '$\bar{x}=2/3$', '$\bar{x}=1$', planes). It may be observed from the figure that the stress levels along '$\bar{x}=0$' plane are higher than the others since near the cantilevered root of the base plate does not move at all while the piezoelectric plate deforms substantially. Similarly when τ_{zx} is examined (Figure 2.41), the stress along ('$\bar{x}=0$' and '$\bar{x}=1$', planes are much higher since the maximum relative displacement occurs along these planes while τ_{zx} is zero along '$\bar{x}=0.5$' plane.
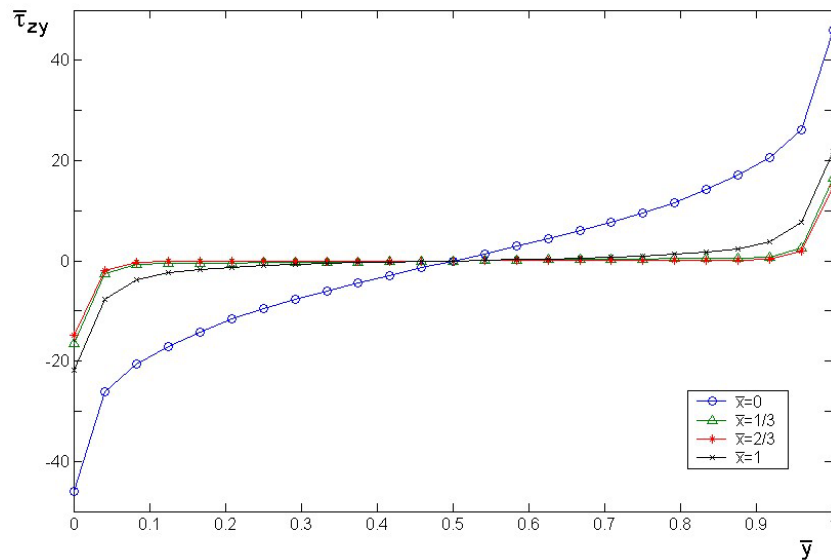
Figure 2.40. Variation of adhesive layer shear stress, $\bar{\tau}_{zy}$, along '$\bar{x} = 0$', '$\bar{x} = 1/3$', '$\bar{x} = 2/3$', and '$\bar{x} = 1$' planes, (fully attached case, 32×32 mesh).

Figure 2.42 to Figure 2.45 compares the shear stresses for delaminated undelaminated configurations along the delamination boundary ('$\bar{x}=1/3$', '$\bar{x}=2/3$', planes). Maximum shear stress τ_{zy} is twice as higher with delamination than it is without delamination, while occurring at the free edges ('$\bar{y}=0$' and '$\bar{y}=1$'). When the τ_{zx} is examined, it may be seen form the figures that the stress with delamination are at least three times higher again occurring along the free

edges. These results show the importance of delamination from adhesive layer shear stresses point of view.
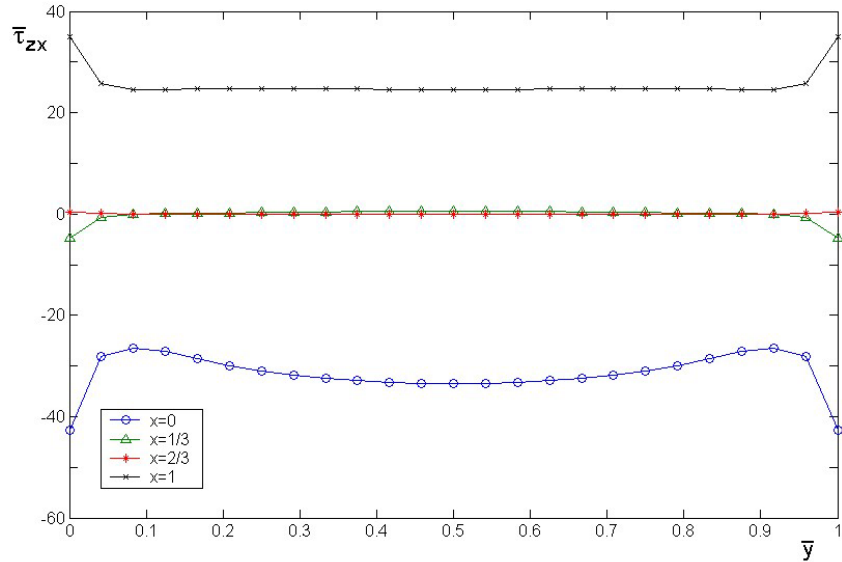
Figure 2.41. Variation of adhesive layer shear stress, $\overline{\tau}_{zx}$, along ' $\overline{x} = 0$', ' $\overline{x} = 1/3$', ' $\overline{x} = 2/3$', and ' $\overline{x} = 1$' planes (fully attached case, 32×32 mesh).
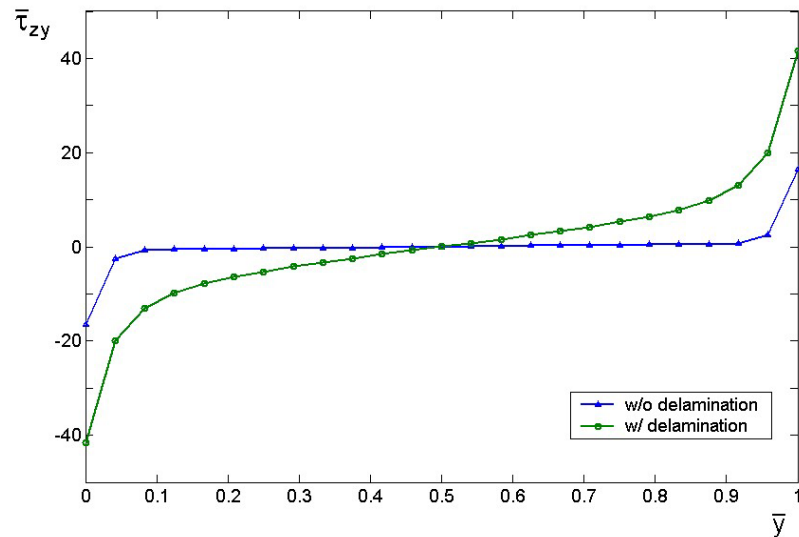
Figure 2.42. Adhesive layer stress $\overline{\tau}_{zy}$ along ' $\overline{x} = 1/3$' plane for fully attached, and delaminated cases (32×32 mesh).

53
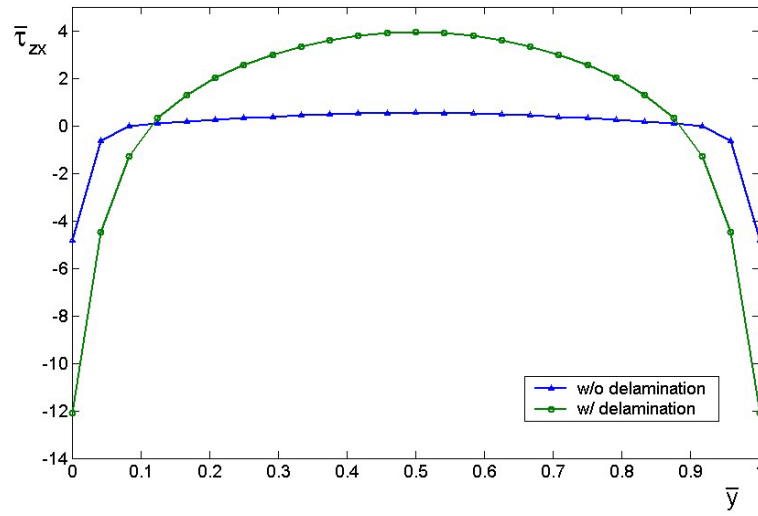
Figure 2.43. Adhesive layer stress $\overline{\tau}_{zx}$ along '$\overline{x} = 1/3$' plane for fully attached, and delaminated cases (32×32 mesh).
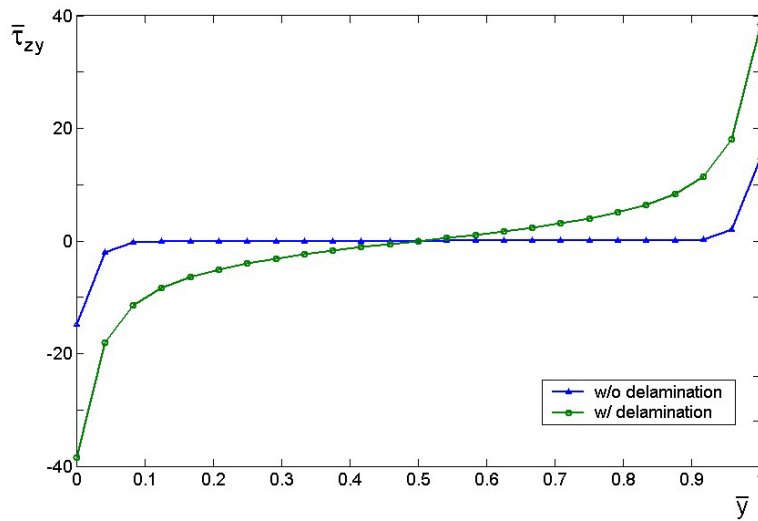
Figure 2.44. Adhesive layer stress $\overline{\tau}_{zy}$ along '$\overline{x} = 2/3$' plane for fully attached, and delaminated cases (32×32 mesh).
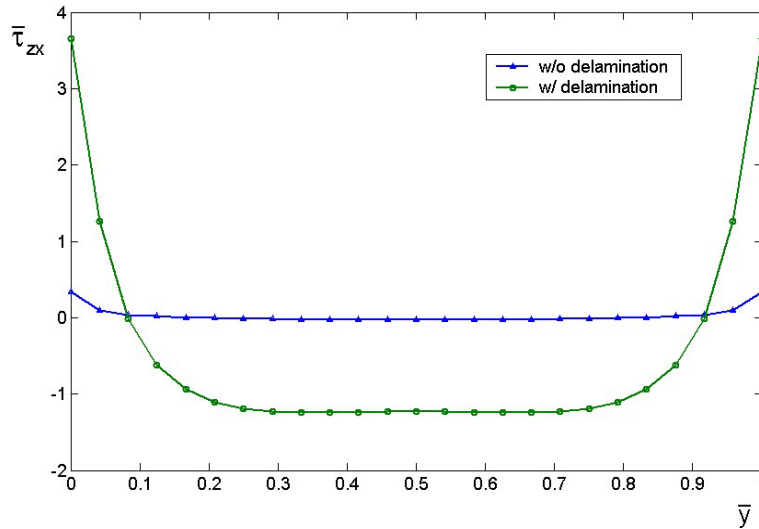
Figure 2.45. Adhesive layer stress $\bar{\tau}_{zx}$ along ' $\bar{x}$ = 2/3' plane for fully attached, and delaminated cases (32×32 mesh).

2.5. SUMMARY OF THE CHAPTER

In this chapter multi-layer plates that contains piezoelectric layers are modeled using a layerwise approach that considers the adhesive layer flexibility. The adhesive layer is assumed to be very thin, massless, and its deformation is linear. The strain energies of the adhesive layers as well as strain energies of the piezoelectric layers are written. Proper finite elements are developed. The coupling terms between the layers due to adhesive layer is depicted in the global stiffness matrix.

The results of the formulation are compared to some results from the literature and good agreement is obtained. The model results are also compared to the predictions obtained using ESL model. It is found that maximum difference in vertical deformations between these two model solutions is about 1.1 percent. It is also shown that the more flexible the adhesive layer, the less it deforms when an electric field is applied. The convergence of the MLP-FAB model is also investigated through the natural frequency solutions.

The model presented in this chapter assumes that the adherends are rigid in the thickness plate direction. This causes inaccurate prediction of adhesive layer stresses when the thickness direction stiffness of the adherends are

comparable to those of the adhesive layer. It is shown that better adhesive layer stress predictions are possible if adhesive layer transverse normal stiffness is adjusted to include the adherend stiffness. The adherend shear deformation may also be important when the adherends are quite thick. Thus, higher order adherend models shall be employed in the future to evaluate the possible improvements to the model presented in this manuscript.

In the last case study, effect of delamination between PZT patch and base plate is investigated. Results show that although deformed shapes are quite similar, local stresses in adhesive layer differ especially near the delaminated region.

Finally it may be stated that the approach developed is capable of accurately modeling multi-layer system with discontinuous patches as well as delaminations.

CHAPTER 3

OPTIMIZATION OF SURFACE-BONDED PIEZOELECTRIC ACTUATORS ON PLATES; PLACEMENT AND SELECTIVE BONDING

3.1. INTRODUCTION

In this chapter, two issues are addressed: The optimum placement of surface bonded piezoelectric actuators and selective bonding of the actuator layer to the substrate is aimed. Design variables of the former type of the problems are locations of the patches. On the other hand, in the case of selective bonding; they are location, size and shape of the bonded region between the patch and substrate. Single objective as well as multi-objective problems is considered, considering either full combination of design variables or using 'Simulated Annealing' optimization algorithm. The selected objective functions are static deformations, modal displacements and special performance indices based on eigenvalues of the controllability grammian. Pareto fronts are obtained for multi-objective cases. Although design variables are continuous, to avoid mesh generation at each iteration, the problem is addressed as a discrete optimization problem. Furthermore, it may be inappropriate to compare results of models having different mesh configurations.

In Section 3.2 definitions of the objective functions are given. In Section 3.3, placement of a single PZT actuator to maximize excitation response of a beam is studied and the results are compared with analytical results found in the literature. In section 3.4, Pareto optimal solutions for multi-objective cases are studied considering full combination of design variables. 'Hide And Seek' Simulated Annealing algorithm is applied for combinatorial PZT placement problems in Section 3.5. In Section 3.6, multi-objective problems, maximizing the control effectiveness while minimizing the spillover, are studied. A multi-objective simulated annealing method, MC-MOSA, is also used in this section. Finally,

optimization of size and location of a rectangular unbonded region between the actuator layer and substrate is studied in Section 3.7.

3.2. STUDIES ON MEASURE OF CONTROLLABILITY

In this study maximization of the control effectiveness for piezoelectric patch placement and selective bonding problems is aimed. Modal displacements and eigenvalues of the controllability grammian are used in the definition of the objective functions. It is also seen that when using controllability grammian, modal reduction is necessary due to large size of the FE models used in the selected case studies.

Equations of motion of multiple-DOFs model are

$$[M]\{\ddot{x}(t)\} + [C]\{\dot{x}(t)\} + [K]\{x(t)\} = [D]\{V(t)\} \qquad (3.1)$$

Where $[M]$, $[C]$, and $[K]$, and are the mass, damping, and stiffness matrices respectively. $[D]$ is the control matrix which has the dimensions of 'n_{dof}' by 'n_{PZT}'. 'n_{dof}' is the total number of degree of freedoms and 'n_{PZT}' denotes the number of the piezoelectric patches. In order to write these equations in modal coordinates, it is possible to describe motion as,

$$\{x(t)\} = [\Phi]\{q(t)\} \qquad (3.2)$$

Where $\{q(t)\}$ is the vector of generalized coordinates and $[\Phi]$ is the modal matrix where columns are eigenvectors. Mass, stiffness and applied forcing are converted into the modal coordinates as shown below. These are called generalized mass, generalized stiffness and generalized force.

$$m_{g_i} = \{\Phi_i\}^T [M]\{\Phi_i\} \qquad (3.3)$$

$$k_{g_i} = \{\Phi_i\}^T [K]\{\Phi_i\} \qquad (3.4)$$

$$F_{g_i} = \{\Phi_i\}^T [D]\{V(t)\} \qquad (3.5)$$

Using these equations we can re-write equations of motion in modal coordinates. Furthermore, if we assume damping matrix is composed of a linear combination

of mass and stiffness matrices, equations of motion in modal coordinates will become 'n_{dof}' uncoupled equations.

$$m_{g_i} \ddot{q}_i(t) + 2\zeta_i \omega_{ni} m_{g_i} \dot{q}_i(t) + k_{g_i} q_i(t) = \{\Phi_i\}^T [D]\{V(t)\} \quad i = 1,2,...,n_{dof} \quad (3.6)$$

where

$$2\zeta_i \omega_{ni} m_{g_i} = c_{g_i} \tag{3.7}$$

'ω_{ni}' and 'ζ_i' are undamped modal frequency and modal damping ratio of the ith mode respectively. c_{gi} denotes generalized damping for the ith mode. Modal damping ratios are generally obtained experimentally.

Instead of considering all modal degrees of freedom, 'n_{dof}', one may take into account first 'n' equations, which have smallest natural frequencies;

$$m_{g_i} \ddot{q}_i(t) + 2\zeta_i \omega_{ni} m_{g_i} \dot{q}_i(t) + k_{g_i} q_i(t) = \{\Phi_i\}^T [D]\{V(t)\} \quad i = 1,2,...,n \quad (3.8)$$

or in matrix form;

$$[I]\{\ddot{q}(t)\} + [\tilde{C}]\{\dot{q}(t)\} + [\tilde{K}]\{q(t)\} = [\tilde{D}]\{V(t)\} \tag{3.9}$$

This modal reduction approach is the simplest one. There are however, other modal reduction techniques, one of which is called the balanced realization [51] In general, most energy is stored in the very few of the lowest modes. Thus the response of the structure may be approximated using these modes. However the value 'n' must also be selected adequately when persistent disturbance exists to reflect the response of the structure for any range of possible forcing frequency.

Transforming the second order equations of motion in modal coordinates may be written in state space form [51]:

$$\{\dot{z}\} = [A]\{z\} + [B]\{V\} \tag{3.10}$$

where;

$$\{z\} = \left\{ \begin{array}{c} \{q\} \\ \{\dot{q}\} \end{array} \right\} \qquad [A] = \begin{bmatrix} [0] & [I] \\ -[\tilde{K}] & -[\tilde{C}] \end{bmatrix} \qquad [B] = \begin{bmatrix} [0] \\ [\tilde{D}] \end{bmatrix} \qquad \text{(3.11)}$$

The state vector may also be defined as [52];

$$\{z\} = \left\{ \dot{q}_1 \quad \omega_1 q_1 \quad \dot{q}_2 \quad \omega_2 q_2 \quad \ldots \quad \dot{q}_n \quad \omega_n q_{n1} \right\} \qquad \text{(3.12)}$$

then state and input matrices are,

$$[A] = \begin{bmatrix} -2\xi_1\omega_1 & -\omega_1 & & & \\ \omega_1 & 0 & & 0 & \\ & & \ddots & & \\ & 0 & & -2\xi_n\omega_n & -\omega_n \\ & & & \omega_n & 0 \end{bmatrix} \qquad \text{(3.13)}$$

$$[B] = \begin{bmatrix} \tilde{D}_{11} & & \tilde{D}_{1\,n_{PZT}} \\ 0 & \cdots & 0 \\ \vdots & & \vdots \\ \tilde{D}_{n_{dof}\,1} & & \tilde{D}_{n_{dof}\,n_{PZT}} \\ 0 & \cdots & 0 \end{bmatrix} \qquad \text{(3.14)}$$

This latter definition of the modal state vector is advantageous in extracting the eigenvalues of the controllability grammian, in addition the order of the magnitudes of the eigenvalues corresponding to position and velocity states will be close to each other.

3.2.1. Modal Displacements

Modal displacements caused by piezoelectric forces are also a good measure of controllability. In order to solve modal equations of motion, we may separate modal displacements into two parts, such as caused by initial conditions and forcing.

$$q_i(t) = q_{I_i}(t) + q_{f_i}(t) \tag{3.15}$$

The modal displacements caused by initial conditions [53];

$$q_{I_i}(t) = e^{-\varsigma_i \omega_{n_i} t} \left[\left(\frac{\dot{q}_i(0) + q_i(0)\zeta_i \omega_{n_i}}{\omega_{d_i}} \right) \sin\left(\omega_{d_i} t\right) + q_i(0) \cos\left(\omega_{d_i} t\right) \right] \tag{3.16}$$

and the forced modal displacement (Duhamel's Integral);

$$q_{f_i}(t) = \frac{1}{m_{g_i} \omega_{d_i}} \int_0^t F_{g_i}(\tau) e^{-\varsigma_i \omega_{n_i}(t-\tau)} \sin\left[\omega_{d_i}(t-\tau)\right] d\tau \tag{3.17}$$

where the initial modal displacement and velocity are

$$q_i(0) = \frac{1}{m_{g_i}} \{\Phi_i\}^T [M]\{x(0)\} \tag{3.18}$$

$$\dot{q}_i(0) = \frac{1}{m_{g_i}} \{\Phi_i\}^T [M]\{\dot{x}(0)\} \tag{3.19}$$

and damped natural frequency is,

$$\omega_{di} = \omega_{ni} \sqrt{1 - \zeta_i^2} \tag{3.20}$$

It may be noted that, when modal damping ratio is less than 10 percent, the difference between the damped natural frequency and natural frequency is also less than 0.5 percent. For an undamped system Equation (3.22) and Equation (3.23) become;

$$q_{I_i}(t) = \left(\frac{\dot{q}_i(0)}{\omega_{n_i}} \right) \sin\left(\omega_{n_i} t\right) + q_i(0) \cos\left(\omega_{n_i} t\right) \tag{3.21}$$

$$q_{f_i}(t) = \frac{1}{m_{g_i} \omega_{n_i}} \int_0^t F_{g_i}(\tau) \sin\left[\omega_{n_i}(t-\tau)\right] d\tau \tag{3.22}$$

3.2.2. Responses to Different Forcing Functions

In this section forced modal displacements are calculated for different excitation functions.

Diract Delta Function

If load is impulsive, a pulse acting for a very short duration (when $t=a$), the forcing function may be expressed as;

$$\{F_{diract}(t)\} = [D]\{V\}\delta(t-a) \tag{3.23}$$

then using Equation (3.5)

$$F_{diract\,g_i}(t) = \{\Phi_i\}^T [D]\{V\}\delta(t-a) \tag{3.24}$$

defining a coefficient vector 'C' as;

$$C_i = \{\Phi_i\}^T [D]\{V\} \tag{3.25}$$

then using (3.22), (3.24) and (3.25), forced modal displacements may be expressed as;

$$q_{diract\,f_i}(t) = \frac{C_i}{m_{g_i} \omega_{n_i}} \int_0^t \delta(\sigma-a) \sin\left[\omega_{n_i}(t-\sigma)\right] d\sigma \tag{3.26}$$

by taking this integral,

$$q_{diract\,f_i}(t) = 0 \qquad\qquad if\ a \geq t$$

$$q_{diract\,f_i}(t) = \frac{C_i}{m_{g_i} \omega_{n_i}} \sin\left[\omega_{n_i}(t-a)\right] \qquad if\ a < t \tag{3.27}$$

<u>Step Function</u>

If a constant load is applied after time '$t=a$', forcing function is;

$$\{F_{step}(t)\} = [D]\{V\}h(t-a)$$
$$h(t-a) = 0 \ if \ t < a, \ h(t-a) = 1 \ otherwise$$

(3.28)

then using Equation (3.5) and (3.25),

$$F_{step\,g_i}(t) = C_i\,h(t-a)$$

(3.29)

Using (3.22) and (3.29) forced modal displacements may be written as;

$$q_{f_i}(t) = \frac{C_i}{m_{g_i}\,\omega_{n_i}}\int_0^t h(\sigma-a)\,\sin\left[\omega_{n_i}(t-\sigma)\right]d\sigma$$

(3.30)

or

$$q_{f_i}(t) = 0 \qquad\qquad if \ a \geq t$$
$$q_{f_i}(t) = \frac{C_i}{m_{g_i}\,\omega_{n_i}^2}\left(1 - \cos\left[\omega_{n_i}(t-a)\right]\right) \qquad if \ a < t$$

(3.31)

<u>Sinusoidal Loading</u>

Sinusoidal loading having circular frequency of ω_f may be expressed as;

$$\{F_{\sin}(t)\} = [D]\{V\}\sin(\omega_f t)$$

(3.32)

using Equation (3.5) and (3.25),

$$F_{\sin g_i}(t) = C_i\sin(\omega_f t)$$

(3.33)

and, forced modal displacements are;

$$q_{\sin f_i}(t) = \frac{C_i}{m_{g_i}\,\omega_{n_i}}\int_0^t \sin(\omega_f\sigma)\,\sin\left[\omega_{n_i}(t-\sigma)\right]d\sigma$$

(3.34)

63

or

$$q_{\sin f_i}(t) = \frac{C_i}{m_{g_i} \omega_{n_i}} \left[\frac{\omega_f \sin(\omega_n t) - \omega_n \sin(\omega_f t)}{\omega_f^2 - \omega_n^2} \right]$$ (3.35)

3.2.3. Measure of Controllability

The actuator placement shall be carried out to realize a controllable structure. However, the information, obtained from controllability matrix is binary, and says if states are controllable or not. Therefore, this information does not have any quantitative value about the controllability. For example, an actuator acting on the strain nodal point of the vibrating beam cannot have any control for that mode. However, if the actuation point is shifted by a very small amount, it is possible to control that mode, although through a large amount of control effort. Consequently, there is a need to determine how controllable the structure is. There are many different approaches presented in the literature to measure the degree of controllability [51]. One of the most common quantitative approaches about the controllability is to investigate eigenvalues of the controllability grammian matrix. The controllability grammian [51];

$$[W_C] = \int_0^\infty e^{[A]\tau} [B][B]^T e^{[A]^T \tau} d\tau$$ (3.36)

is generally obtained by solving the Lyapunov equation for asymptotically stable systems:

$$[A][W_C] + [W_C][A]^T + [B][B]^T = 0$$ (3.37)

The system should be stable. Then the system is controllable if the controllability grammian is nonsingular. A performance index, which utilizes the eigenvalues of the controllability grammian, was suggested by Hac and Liu [52].

$$PI = \left(\sum_{j=1}^{2n} \lambda_j \right) \sqrt[2n]{\prod_{j=1}^{2n} \lambda_j}$$ (3.38)

64

Where λ_j denotes the eigenvalues of the controllability grammian. The performance index has two parts. The first term represents the importance of summation of all eigenvalues, while the second term guarantees none of the eigenvalues to be small when maximizing this index. In their study [52], control spillover problem is also considered and they suggested the index below;

$$PI = \left(\sum_{j=1}^{2N} \lambda_j \right) \sqrt[2N]{\prod_{j=1}^{2N} \lambda_j} - \gamma \left(\sum_{k=2N+1}^{2n} \lambda_k \right) \sqrt[2(n-N)]{\prod_{k=2N+1}^{2n} \lambda_k} \qquad n > N \qquad (3.39)$$

With this index, it is possible to maximize eigenvalues of the controllability grammian for first *N* number of modes while keeping them small for rest of the modes. γ is the weighting constant which adjusts the importance of the spillover. Although this performance index is suitable to reflect the individual importance of the controlled modes, it may be inappropriate for the residual modes in some cases. For instance, when one of the residual modes is completely uncontrollable and a significant spillover is existed for the rest of the residual modes, this term is equal to zero and does not contribute the amount of the spillover in the performance index. To remedy this problem, the following PI may be used;

$$PI = \left(\sum_{j=1}^{2N} \lambda_j \right) \sqrt[2N]{\prod_{j=1}^{2N} \lambda_j} - \sum_{k=2N+1}^{2n} \gamma_{k-2N} \lambda_k \qquad n > N \qquad (3.40)$$

Where γ's are the weights for each eigenvalue, related to the residual modes. Finding these weights for a specific problem is the main disadvantage of the latter definition of the performance index.

Alternatively, the first and the second terms in Equation (3.39) and (3.40) may be considered as separate objective functions and Pareto frontal solutions may be searched for. In that case, the objective is to maximize the eigenvalues of the controlled modes and to minimize the eigenvalues of the residual modes. Although, weight constant in (3.39) is unnecessary, individual weights for each eigenvalue may still be required to scale the eigenvalues.

A more exhaustive study may be conducted by choosing each eigenvalue of the controllability grammian as a separate objective function. However, it may

not be very practical since the total numbers of controllable and residual modes to be considered are usually very large.

As stated in Reference [52], the values of eigenvalues and diagonal elements of the controllability grammian are very close when the state vector defined in Equation (3.12) is employed for lightly damped structures having well spaced modal frequencies. Therefore, (3.38), (3.39) and (3.40) may be re-written using the diagonal elements instead of the eigenvalues.

3.3. MODAL DISPLACEMENT TO PLACE A SINGLE PIEZOELECTRIC ACTUATOR ON A BEAM

Before carrying out a formal optimization procedure, results obtained from MLP-FAB formulation is compared with analytical results found in the literature, namely, with study of Barboni, et al. [54]. In their study, they chose an isotropic cantilever beam as base structure and placed a single pair of piezoelectric actuator patches on top and bottom surfaces. Bonding was assumed to be perfect. Length and position of the actuator were chosen as design variables. They neglected the effect of stiffness and mass of the piezoelectric patch to the system. Since their model was very simple, they were able to include their design variables in the objective function (deflection of the beam) explicitly. Then optimality condition, using this analytical solution, was easily established.

In order to have a meaningful comparison with these analytical results, our geometry and material properties were selected carefully. In Table 3.1, these parameters and why they were chosen, are given. In Table 3.2, the difference in modal frequencies for first four modes between two cases, where in the first case, the beam is without a piezoelectric patch and in the second case it is fully covered with a piezoelectric layer, is also shown. Among these modes, second and fourth modes are not controllable with our selected configurations, since these are bending modes in the plane of the plate. Mode shapes of the controllable modes are given in Figure 3.1 It may be noted that, using top actuator instead of a pair of actuators is another difference between our model and the analytical model [54].

Table 3.1. Geometry and material Properties.

Property		Value	Comment
Plate dimensions a x b		200 mm x 10 mm	High aspect ratio imitating a beam
Plate	E	200000 Mpa	Steel is chosen as substructure material to reduce the effect of stiffness and mass of the piezoelectric patch. In the study of Barboni, et al. [54], these contributions are totally ignored.
	G	76920 Mpa	
	Density	7.8E-9 Mg/mm^{3*}	
	Thickness	5 mm	
PZT patch	E	63000 Mpa	A thin piezoelectric patch is used, to reduce the stiffness and mass effects of the patch on the response of the structure.
	G	24230 Mpa	
	Density	7.64E-9 Mg/mm^3	
	Thickness	1 mm	
Adhesive	E	4000 Mpa	Relatively hard adhesive is chosen to approximate rigid bonding
	G	1400 Mpa	
	Thickness	0.1 mm	

Table 3.2. Comparison of modal frequencies for first four modes between two extreme cases, a beam without a piezoelectric patch and a beam, fully covered with a piezoelectric layer.

Mode	Modal Frequency (Hz) without any piezoelectric patch	Modal Frequency (Hz) fully covered w/ the piezoelectric layer
1st Bending	102.7	105.4
1st Bending (in the plane of plate)	248.6	234.4
2nd Bending	643.7	660.2
2nd Bending (in the plane of plate)	1545	1457

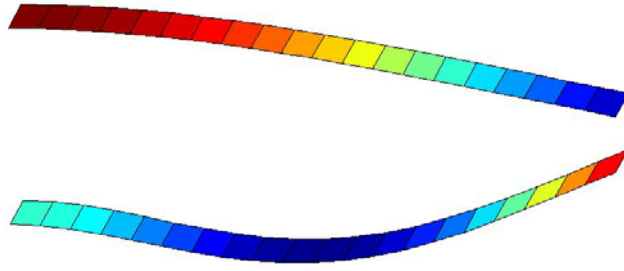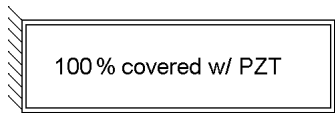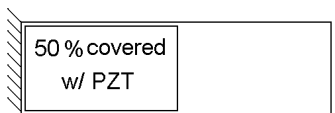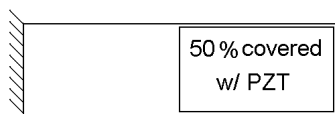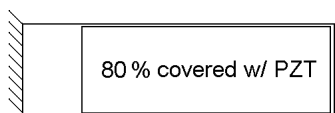* Mg/mm^3 is used as density unit in order to be compatible with Mpa-mm unit System.

Figure 3.1. First and third mode shapes of the beam without PZT patch (20x1 mesh). Similar mode shapes are obtained for a beam, fully or partially covered with a surface bonded patch, whose properties are given in Table 3.1.

Table 3.3. Four different configurations and their effectiveness in terms of modal amplitude created by applying step unit voltage.

Configuration	Mode	Amplitude per Unit Voltage (10^{-6}) mm/V	Modal Frequency (Hz)
100 % covered w/ PZT	1-20	343.0	-
	1	**309.8**	105.4
	3	25.83	660.2
50 % covered w/ PZT	1-20	262.1	-
	1	262.1	113.9
	3	0.6004	657.3
50 % covered w/ PZT	1-20	77.28	-
	1	45.04	94.90
	3	23.21	641.4
80 % covered w/ PZT	1-20	211.4	-
	1	163.3	97.95
	3	**42.28**	640.9

During this study, modal displacement at the tip per unit voltage applied on actuator is chosen as measure of controllability and aimed to be maximized. In Table 3.3, four different configurations of single piezoelectric patch are considered and corresponding results are given. Values, printed bold, are the maximums of the mode among selected configurations. Therefore, first and fourth configurations are found as best solutions to control first and third modes

respectively. It may be noted that, for controlling the first mode, fully covered configuration, and for the third mode, 78.5% of the total beam length covered with piezoelectric patch starting from the free side were found to be the optimum solutions by Barboni et al. as well [54].

A denser mesh (50x1) is also used to refine the best placement results of the third mode Table 3.4. After fitting a second order curve, the optimum value of the PZT covering percentage is found as 80.68, which is 2.8% more than the results of analytical model [54].

Table 3.4. Three different configurations are considered to find optimal solution to control the third mode. Form these results, 80.68% is found as optimal value of percentage of PZT covered area from the free side.

PZT covered surface percentage	10^{-6} Max Amplitude per Unit Voltage (10^{-6}) mm/V	3rd modal Frequency (Hz)
78%	41.99	640.7
80%	42.20	640.3
82%	42.16	639.9

Taking patch length as constant, finding the best position of the piezoelectric patch to control 5th mode (Figure 3.2) is another case, studied in Reference [54]. In their example the patch length was 20% of the beam length (Figure 3.3). They found optimum distance between the wall and center of the patch to be 71.1% of the beam length. To examine if our optimum location is close to this value, different piezoelectric patch positions were tested (Table 3.5). By fitting a second order curve to these displacement values, optimum value of the distance from center of the piezoelectric patch to the wall is found as 70.07% of the beam length, which is sufficiently close to the value presented by Barboni et al. [54]. Contribution of this mode to the transverse displacement at tip is taken as measure of controllability. Responses due to first twenty modes, and 5th mode only are shown in Figure 3.4 and Figure 3.5 respectively. It is seen that, 5th mode has an important contribution to the response of the structure.
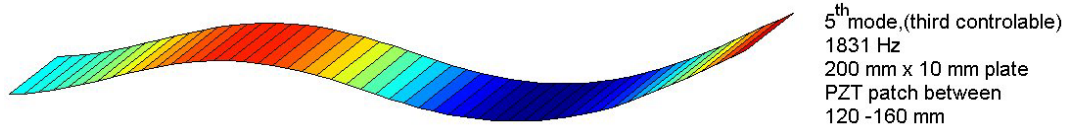
Figure 3.2. Fifth mode shapes of the beam without PZT patch (20x1 mesh). 5th mode shape of the beam, covered with a surface bonded patch, whose properties are given in Table 3.1 is similar.
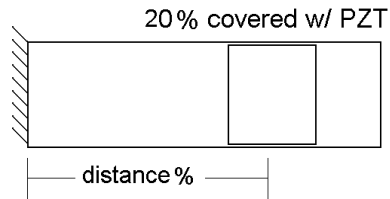

Figure 3.3. The distance between the wall and center of the piezoelectric patch.
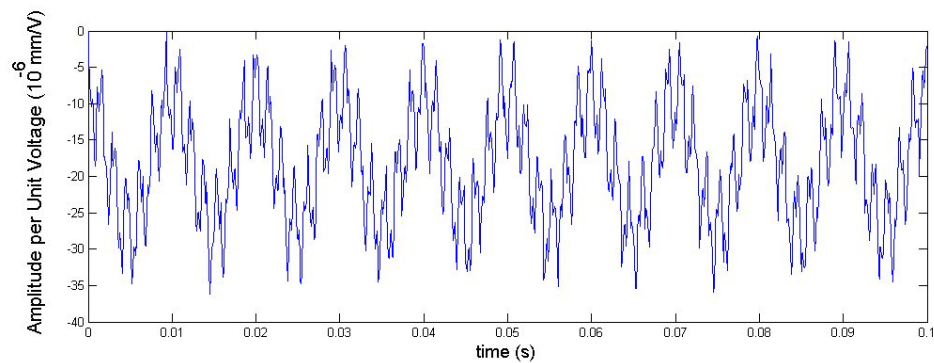

Figure 3.4. Vertical displacement at the tip when 1 Volt stepwise input is applied on piezoelectric patch. Only the contributions of the first 20 modes are considered.
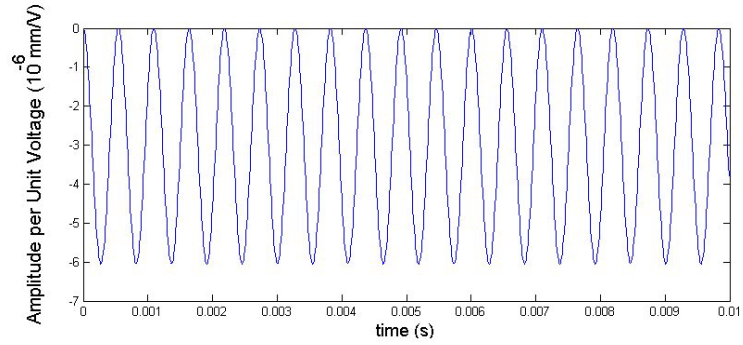
Figure 3.5. Response at the tip to a 1 Volt input is applied to the piezoelectric patch, covering the area between 60% and 80% of the beam. Only the contribution of the 5th mode is shown.

Table 3.5 Three different configurations are considered to find optimum solution to control the fifth mode. From these results, 70.07% is found as optimal value of percent distance between center of the PZT and the wall.

Ratio of distance between PZT center and the wall to the beam length	10^{-6} Max Amplitude per Unit Voltage (10^{-6}) mm/V	5th modal Frequency (Hz)
68%	5.9707	1829
70%	6.0468	1831
72%	5.9803	1833

3.4. MULTIPLE MODAL DISPLACEMENT OBJECTIVE TO PLACE PIEZOLECTRIC ACTUATOR(S) ON A PLATE: PIEZOELECTRIC PATCH(S) ON RECTANGULAR CANTILEVER BASE PLATE

Optimal placement of one and two PZT patches on an isotropic rectangular cantilevered base plate is studied. Maximization of first three modal displacements is sought for. The same finite element mesh is used throughout the optimization. Therefore, the optimization problem is a discrete one. Since PZT patches also contribute mass and stiffness matrices of the system, for each combination corresponding matrices, and eigenvectors are re-calculated to find modal displacements.

Geometry of the base plate and patches, and definition of design variables are shown in Figure 3.6 and Figure 3.7. Material Properties and thickness of layers are given in Table 3.6. It shall be noted that, power consumptions of a

71

single-PZT patch and two-PZT patch cases are assumed to be the same to have better comparison between the optimal results. In Figure 3.8, first three mode shapes of the base plate without any PZT patch are given.

In this section, solutions to the full combination of patch locations (discarding symmetric cases) are obtained and discussed below. Hence no optimization code is employed.
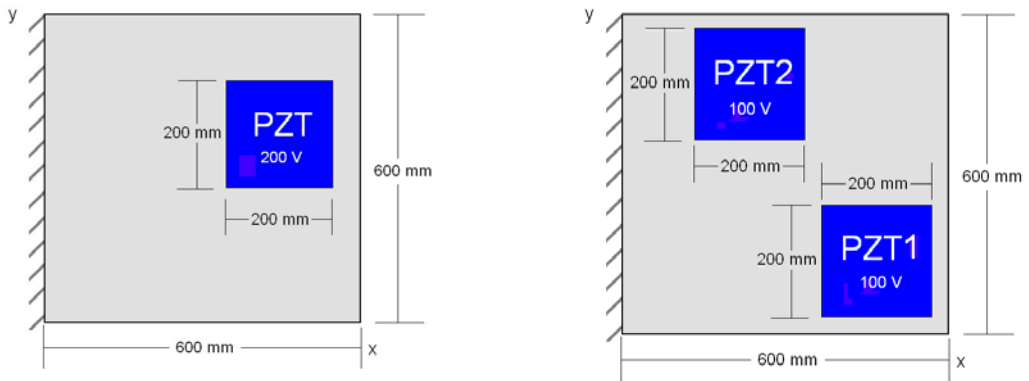

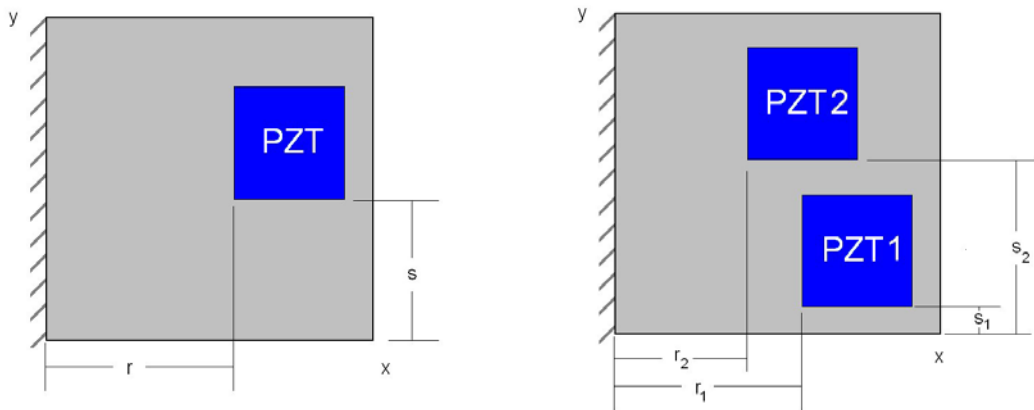Figure 3.6. Geometry of the base plate and PZT patch(s).

Figure 3.7. Definition of design variables. Since positions of the patches must correspond with previously defined FE mesh, these design variables are discrete.

Table 3.6. Material Properties and thickness of layers.

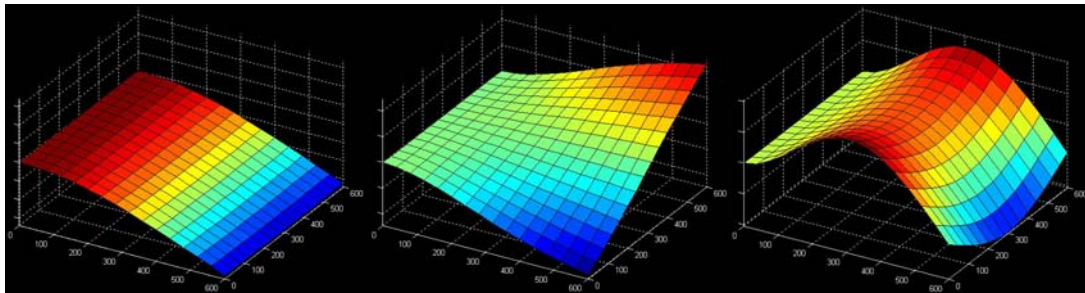| Layer	Property	Value
Base Plate	Modulus of Elasticity	200,000 Mpa
	Poisson's Ratio	0.3
	Density	7.8 10^{-6} kg/mm^3
	Thickness	5 mm
PZT	Modulus of Elasticity	63,000 Mpa
	Poisson's Ratio	0.3
	Density	7.64 10^{-6} kg/mm^3
	Thickness	1 mm
Adhesive	Modulus of Elasticity	4000 Mpa
	Shear Modulus	1400 Mpa
	Thickness	0.1 mm

Figure 3.8. First, second and third mode shapes of 600mm x 600mm, 5 mm thick-steel-plate. Frequencies are 11.76 Hz, 28.82 Hz and 72.10 Hz. 15x15 mesh.

3.4.1. Placement of Single Piezoelectric Patch

In this section, the placement of a single piezoelectric patch is examined. For this purpose, three objectives are considered. They are the modal displacements corresponding to the first three modes. The problem is solved for different mesh sizes. In Table 3.7, total number of combinations and total number of Pareto points are given for different mesh configurations. As expected, as the number of finite elements increase, not only the total number of possible patch locations increases, the number of Pareto frontal points increases as well. However the rate increase in the number of total Pareto points is much slower as it may be obtained from Figure 3.9.

Table 3.7 Number of total combinations and total Pareto points for different mesh configurations.

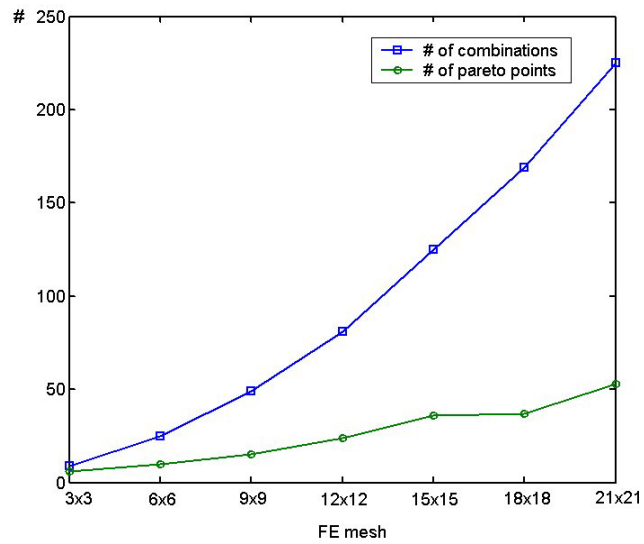| FE Mesh	Number of Combinations	Number of Total Pareto Frontal Points	Percentage of Pareto Points
3x3	9	6	66.67
6x6	25	10	40.00
9x9	49	15	30.61
12x12	81	24	29.63
15x15	121	36	29.75
18x18	169	37	21.89
21x21	225	53	23.56

Figure 3.9. Total number of combinations and total Pareto points for different mesh configurations

The results showing the modal displacements of the first three modes are presented in Figure 3.10. Those solutions that are on the front are identified by a circle (Figure 3.10). Figure 3.11 give two objective views. Note that these objective values, denoted as '$f1$', '$f2$', and '$f3$', are normalized with respect to their maximum such that;

$$fi = \left| \frac{value\,of\,i^{th}\,objective}{\max\,(value\,i^{th}\,objective)} \right| \quad i = 1,2,3 \tag{3.41}$$

74

The plots show that some objectives contradict each other. If we look at the first plot in Figure 3.11, it may be seen that, Pareto points related to first and second objectives are those eight points on the left. If we concentrate on the point where $f2$ is equal to 1, we see that $f1$ is about 0.9 and still high. Therefore we may conclude best solution for $f2$ is one of the best solutions for $f1$ and contradiction is not high. On the other hand best solution for $f1$ is worst solution for $f2$ and contradiction is high. Similar conclusions may be stated between $f1$ and $f3$ or between $f2$ and $f3$, after carefully examining the plots given in Figure 3.11.
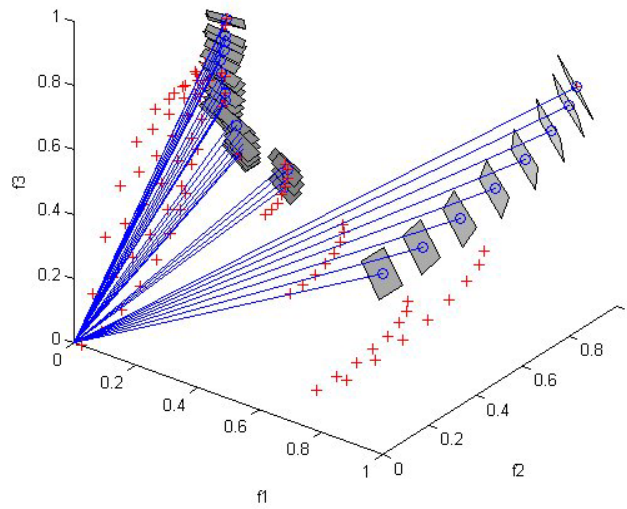

Figure 3.10 Plot of Pareto optimal points for the solution of 21x21 mesh. For better visualization Pareto optimal points are shown with small planes whose normals are pointed to the origin. Other solution points are marked with '+'.

In Figure 3.12, the maximum objective values for different mesh configurations are plotted. The corresponding numerical results are tabulated in Table 3.8. The table shows that, as the element number is increases, the value of the objective function converges the particular values. Including the 3x3 mesh, which has very erroneous results in terms modal displacements. However, note that the best location of single piezoelectric patch, considering each objective separately, is same for all mesh configurations and shown in Figure 3.13. Optimum locations for each objective are;

Best location to maximize first objective; r=0, s=200

Best location to maximize second objective; r=0, s=0 or s=400

Best location to maximize third objective; r=200, s=0 or s= 400

Where 'r' and 's' are design variables, shown in Figure 3.7. These three design points are only a small subset of Pareto optimal points. In objective space, three Pareto points, where '*f1*=1', '*f2*=1' and '*f3*=1' in Figure 3.10, corresponds these design points respectively.
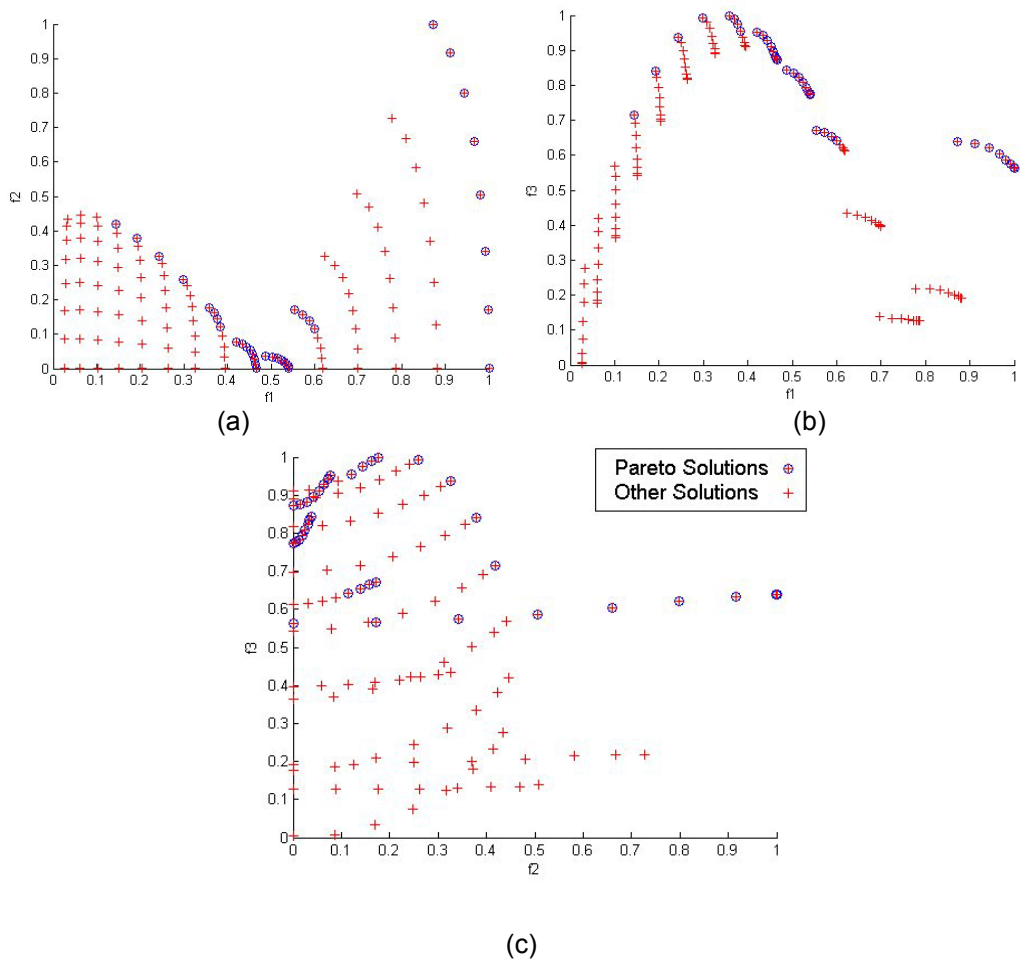

(a)

(b)
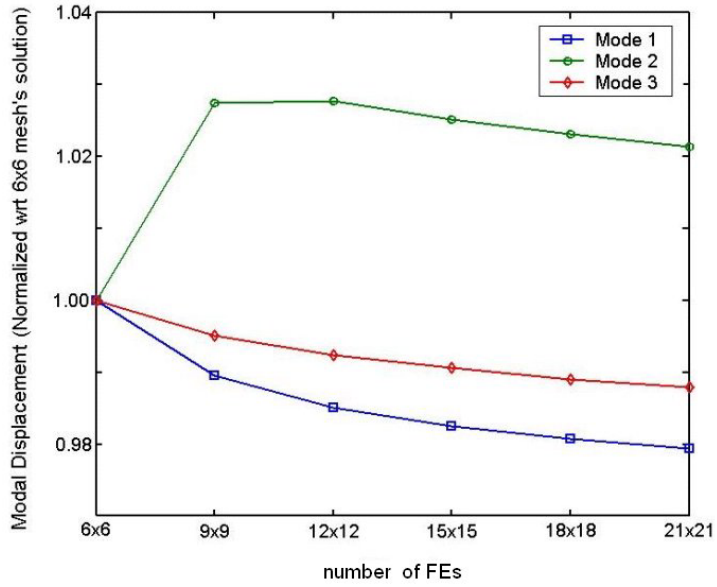
(c)

Figure 3.11. Side views of Figure 3.10.

Figure 3.12. Values of objective functions versus number of FEs . Solution for 3x3 mesh is highly erroneous and not included in this plot.

Table 3.8. Best values of objective functions for different mesh configurations.

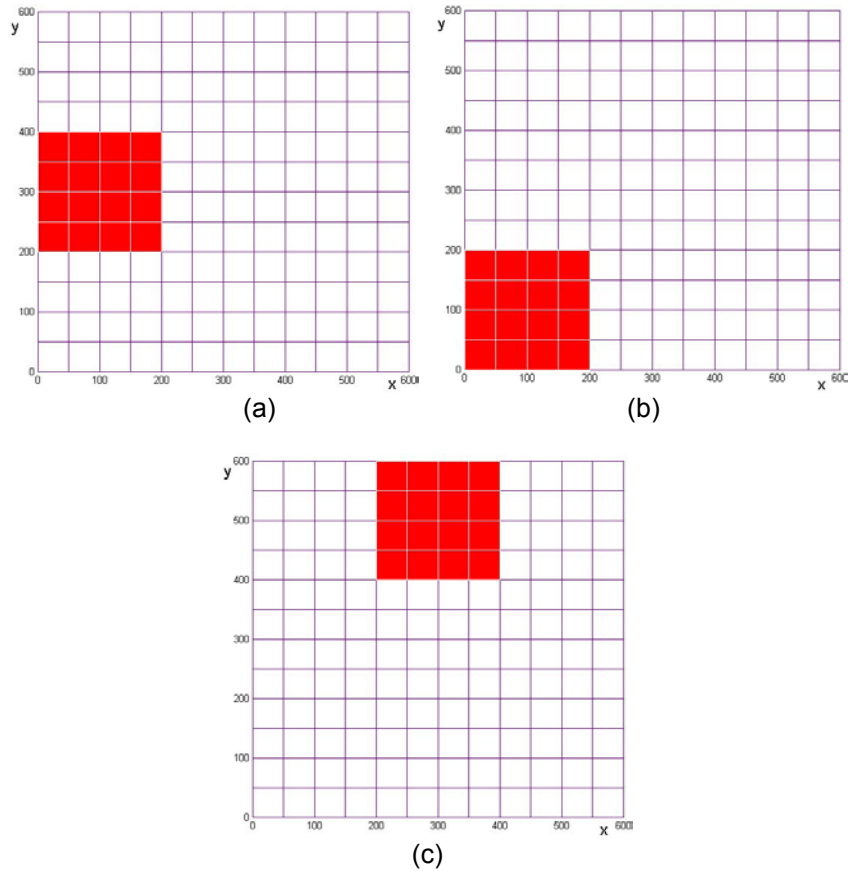| Number of FEs	First Objective x 10^{-9}	Second Objective x 10^{-9}	Third Objective x 10^{-9}
3x3	952.3	24.38	2.653
6x6	943.3	34.20	2.657
9x9	933.5	35.14	2.644
12x12	929.2	35.15	2.637
15x15	926.8	35.06	2.632
18x18	925.1	34.99	2.628
21x21	923.9	34.93	2.625

Figure 3.13. Best placements, considering first, second and third objectives separately. Although, results shown here are for 12x12 mesh, exactly same locations are found for all other mesh configurations from 3x3 to 21x21 mesh. Note that for second and third objectives, symmetric configurations of shown locations give also same maximum results.

3.4.2. Placement of Two Piezoelectric Patches

Same square plate, this time with two piezoelectric actuators is also considered. Total number of actuator placement combinations and those that are on the Pareto front for different mesh configurations are given in Table 3.9. In these calculations minimum distance between the piezoelectric patches is defined as a single finite element. For this reason, it may not be completely appropriate to compare models having different mesh sizes. However, except from the case for the first objective, exactly same piezoelectric patch positions are found as optimum for all mesh configurations (Figure 3.16). For the first objective, since the element size are too large, it is not possible to locate patches as shown in Figure 3.16. On the other hand, exactly same locations are found for the second and the

78

third objectives for all mesh configurations. The maximum objective function values for each mesh are listed in Table 3.10. The objective function values obtained from a 12x12 mesh are plotted in Figure 3.14. The Pareto points are also identified in this figure. The two dimensional plots are given in Figure 3.15. On this figure the Pareto points of the three objective functions are identified by a circle. As before the two-dimensional Pareto plots are the subset of the Pareto points obtained from three objectives.

Table 3.9. Number of total combinations and total Pareto points for different mesh configurations. Since same voltage differences are applied and patches are identical, these numbers are half of the number of combinations for unsymmetrical two-patch case.

FE Mesh	Number of Combinations	Number of Total Pareto Frontal Points	Percentage of Total Pareto Points to All
3x3	16	8	50.00
6x6	132	22	16.67
9x9	516	43	8.333
12x12	1420	75	5.282

Table 3.10. Best values of objective functions for different mesh configurations.

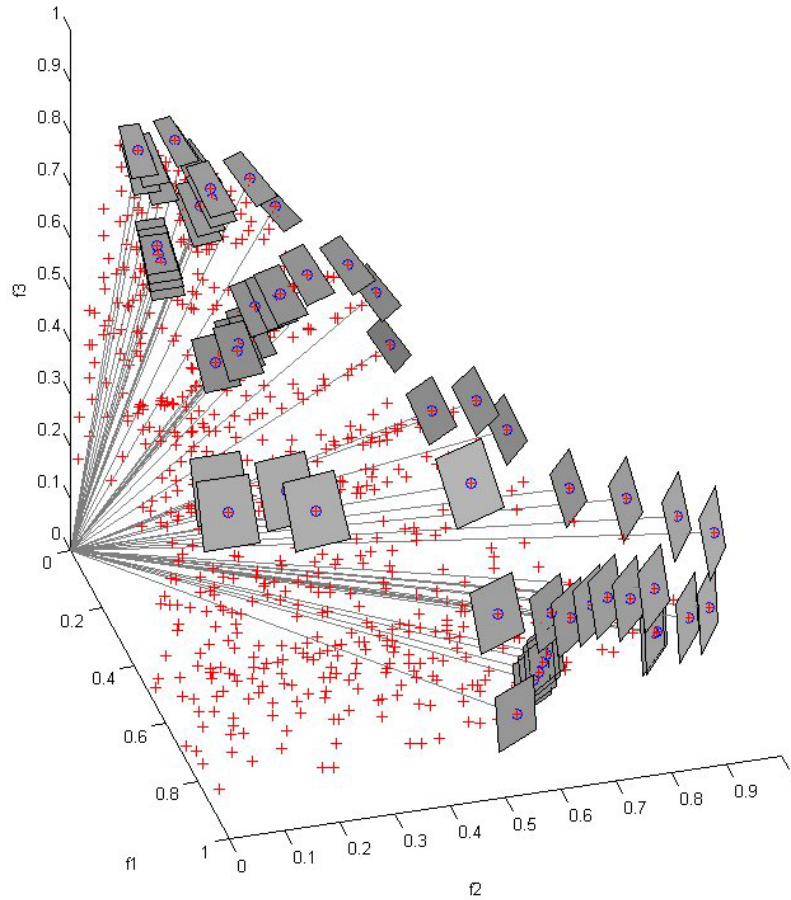| FE Mesh	First Objective $x10^{-9}$	Second Objective $x10^{-9}$	Third Objective $x10^{-9}$
3x3	767.2	18.25	2.594
6x6	775.5	25.81	2.592
9x9	782.9	26.73	2.581
12x12	781.1	26.79	2.576

Figure 3.14. Plot of Pareto optimal points for solution of 12x12 mesh. For better visualization Pareto optimal points are shown with small planes whose normals are pointed to the origin. Other solution points are marked with '+'.

If we examine the plot given in Figure 3.15 (c), the Pareto point, where $f3$ is equal to 1, gives $f2$ as almost 0. This situation may easily be explained since best configuration for the third objective and worst configuration for the second objective (Figure 3.16.b and Figure 3.17). This result is reasonable. On the contrary, when $f1$ is equal to 1 $f3$ is about 0.6 as seen in Figure 3.15.b. Since objectives are modal displacements, and best placement for the first bending mode provides an important amount of control for the second bending mode.
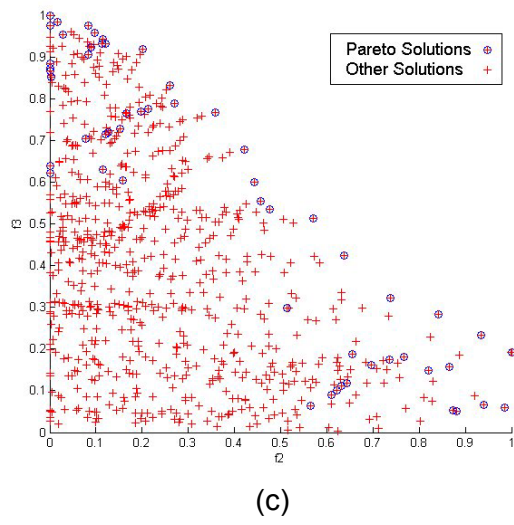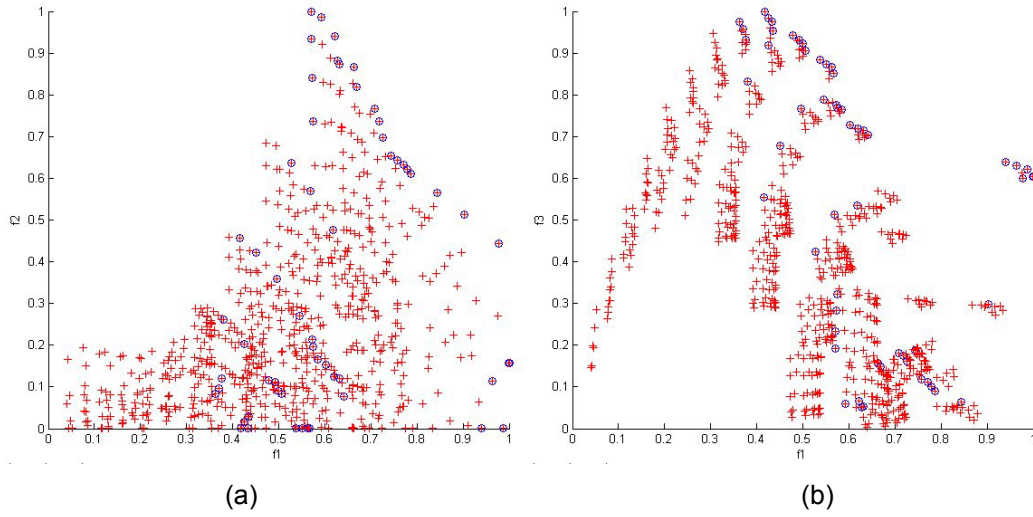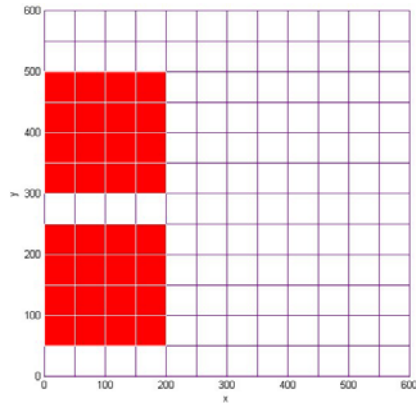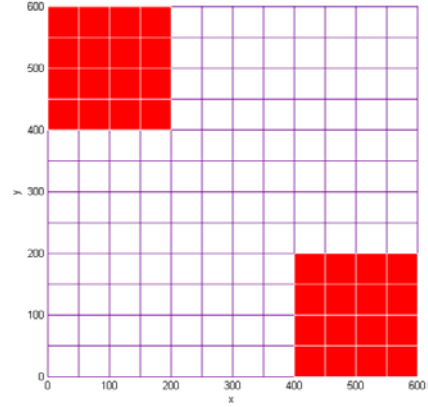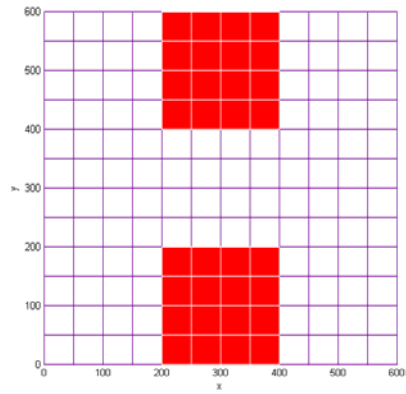
(a)

(b)

(c)

Figure 3.15. Side views of Figure 3.14.

81

(a)

(b)

(c)

Figure 3.16. Best placements, considering first, second and third objectives separately (12x12 mesh).
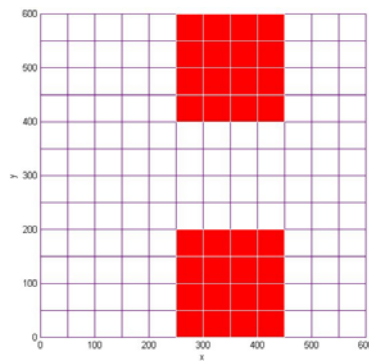

Figure 3.17. Worst placement, considering second objective only (12x12 mesh).

3.5. APPLICATION OF THE SIMULATED ANNEALING ALGORITHM TO COMBINATORIAL ACTUATOR PLACEMENT PROBLEMS

3.5.1. Search Direction and Step Size

'Hide and Seek' is a continuous simulated annealing algorithm [55]. Here, it is employed for a combinatorial optimization problem. Thus, two issues, the search direction and the step size, shall be addressed. Detailed information about the original algorithm is given in Appendix.A.

Three different search methods are considered. In addition to normal and adaptive step size random walk methods, a special method, suitable for our type of problems, which have hyperrectangular design space, is developed.

Random Walk Method (Method I)

Random walk algorithm for continuous problems is given in [55]. However, since we move PZT patches without changing existing finite element mesh, the problem considered is not continuous. Therefore, with some minor modifications to the original algorithm, the following search method is proposed;

Step 0: Choose a starting point x_0 in the interior of design space and set $k=0$.

Step 1: Choose a search direction, θ_k, on unit hypersphere and set '$\gamma = 0$'.

Step 2: Choose a step size λ_k, such that '$x_k + \lambda_k \theta_k$' is in the interior of design space. Use uniform distribution for selection of λ_k. Then round the value of each element of vector '$x_k + \lambda_k \theta_k$' to the nearest integer.

Step 3: If current test point is previously tried, set '$\gamma = \gamma + 1$' and go to Step 2 to choose another λ_k. When '$\gamma = \gamma_{max}$', go to Step 1 to choose another search direction.

Step 4: If probabilistic acceptance criterion is satisfied, accept the test location as the starting point; otherwise do not change the starting point.

Step 5: set '$k=k+1$' and go to step 1.

Since PZT placement problem, using existing FE mesh, is discrete, the probability of selecting previously tried point as new test point is high. In order to prevent unnecessary objective function evaluations, whenever formerly tested point is selected as new test point, it is rejected and method tries to find a new

candidate in the same search direction. However, after certain attempts (γ_{max}), if no new test point can be found on that direction, a new search direction is chosen. It is also possible to change search direction, whenever previously tested solution is selected, by setting γ_{max} as equal to 1.

Random Walk Method with Adaptive Step Size and Controlled Cooling Technique (Method II)

Instead of using adaptive cooling technique of 'Hide and Seek', more controlled cooling method, which does not allow sudden decrease of temperature, may also be used. This is especially useful if we want to relate step size of the search to the current temperature. For example, the following expression does not allow more than 10 percent decrease in temperature for single iteration:

$$T_k = \max\left(THS,\, 0.9\, T_{k-1}\right) \tag{3.42}$$

where T_k is current temperature, THS is 'Hide and Seek' temperature which is calculated as given in previous section and T_{k-1} is temperature of the previous iteration. Then instead of using uniform distribution, the step size may be selected from a temperature dependent probability density function;

$$\lambda_k = \rho^{\eta_k} \delta_{\max} \tag{3.43}$$

where ρ is a random number between 0 and 1 chosen from a uniform distribution, δ_{max} is maximum search step size restricted by boundary of the design space, and η_k is a temperature dependent parameter which determines the shape of probability density function. In this study η_k is assumed as;

$$\eta_k = e^{\left(1 - \frac{T_k}{T_{\max}}\right)} \tag{3.44}$$

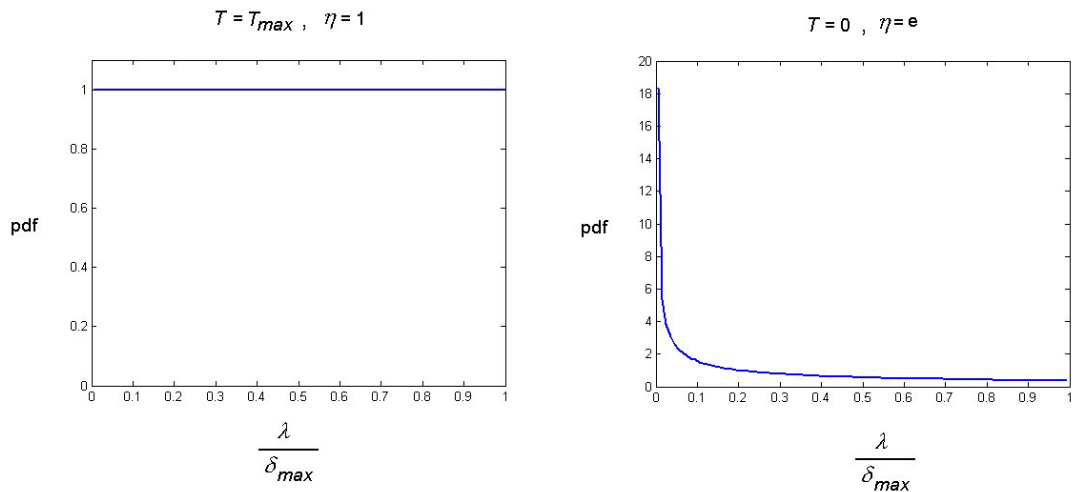In Figure 3.18, probability density functions for two extreme values of 'η_k' are given.

Figure 3.18. Probability density functions for determining the step size, for '$T = T_{max}$' and '$T = 0$'.

One-Dimensional Random Walk Method with Selected Design Variables (Method III)

In addition to random walk with or without uniform distribution, a special method is also considered. Instead of changing all design variables as in previous methods, one of the piezoelectric patches is selected randomly. Then it is allowed to move as described below;

Step 1: Choose a search direction, θ_k, as −1 or 0 or +1 for each design variable related to selected patch and set '$\gamma = 0$'.

Step 2: Choose a step size λ_k, such that '$\lambda_k = \rho^\eta \delta_{max}$' and '$x_k + \lambda_k \theta_k$' must be in the interior of design space, where ρ is a random number with uniform distribution between 0 and 1, η is a parameter which determines the shape of the probability density function, and δ_{max} is maximum search step size either restricted by pre-defined number or boundary of the design space. Each element of vector '$x_k + \lambda_k \theta_k$' must be rounded to the nearest integer since our problems are discrete.

Other steps are same with the steps of Method I. Different aspects of these search algorithms are explained using the simple one-dimensional example given in Figure 3.19.

Current Location
of PZT

Search Direction

-1 ← | → +1

50% probability   50% probability

Probability of choosing A as next test
location if search direction is '+1'

Method I or Method II when $T = T_{max}$ 1/3

Method III

$\eta = 1$ δ_{max} not restricted   1/3

$\eta = 1$ $\delta_{max} = 3$ 1/3

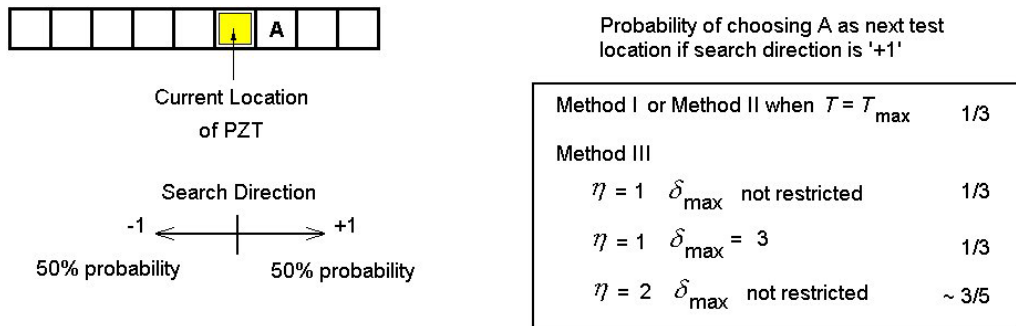$\eta = 2$ δ_{max} not restricted   ~ 3/5

Figure 3.19. 1D example for search algorithm.

From Table 3.11 to Table 3.13 probability of hitting location A, B or C as next test location is given for different search parameters of Method III. It is seen that if step size is restricted (Table 3.12) or probability of hitting closer neighborhood is increased (Table 3.13), probability of selecting A, B or C as the next test point is almost independent from the location of A, B and C. In other words, probability of success to find optimum, if optimum is A or B or C, is nearly equal for these methods. On the other hand, probability of finding optimum, with parameters used in Table 3.11, may be very low or high dependent on the location of optimum. It may be also noted that, since example is one dimensional, Method I would also give same results with Method III. Therefore, assuming that we do not know the location of the optimum, restricting the step size or increasing the probability of choosing closer solutions to the current initial location may be more suitable for our problems. However, if we restrict maximum step size, there is more chance of being trapped at the local optima, since we may miss the possibility of searching all design space. These ideas are more clearly presented with the example problems given in Section 3.5.3.

Table 3.11. Probability of selecting A, B or C as next test location for Method I or Method III with '$\eta = 1$' and δ_{max} is equal to distance from current location to the boundary of the feasible space in selected direction.

Starting search location (black square)	A (%)	B (%)	C (%)
A (black) B C — position 1	-	12.50	12.50
A B C — position 2	50.00	7.14	7.14
A B(black) C — position 3	25.00	-	8.33
A B C — position 4	16.67	16.67	10.00
A B C(black) — position 5	12.50	12.50	-
A B C — position 6	10.00	10.00	10.00
A B C — position 7	8.33	8.33	8.33
A B C — position 8	7.14	7.14	7.14
A B C — position 9	12.50	12.50	12.50
Average	17.77	10.85	9.49
Difference between averages of A and C			**8.28**

Table 3.12. Probability of hitting A, B or C as next test location for Method III with '$\eta = 1$' and '$\delta_{max} = 3$'.

Starting search location (black square)	A (%)	B (%)	C (%)
A (black) B C — position 1	-	33.33	0
A B C — position 2	50.00	16.67	16.67
A B(black) C — position 3	25.00	-	16.67
A B C — position 4	16.67	16.67	16.67
A B C(black) — position 5	0	16.67	-
A B C — position 6	0	16.67	16.67
A B C — position 7	0	0	16.67
A B C — position 8	0	0	16.67
A B C — position 9	0	0	0
Average	11.46	12.50	12.50
Difference between averages of A and C			**1.04**

Table 3.13. Probability of hitting A, B or C as next test location for Method III with '$\eta = 2$' and δ_{max} is equal to distance from current location to the boundary of the feasible space in selected direction.

Starting search location (black square)	A (%)	B (%)	C (%)
[A]■ B C (black at A)	-	11.33	8.41
A ■ B C (black 2nd)	50.00	19.14	5.88
A [B]■ C (black at B)	14.36	-	8.71
A B ■ C (black 4th)	9.21	29.36	22.67
A B [C]■ (black at C)	6.69	10.13	-
A B C ■ (black 6th)	5.28	6.92	22.67
A B C ■ (black 7th)	4.32	5.15	8.71
A B C ■ (black 8th)	3.69	4.34	5.88
A B C ■ (black 9th)	6.33	7.51	8.41
Average	12.48	11.73	11.42
Difference between averages of A and C			**1.06**

3.5.2. Stopping Criteria

Four different stopping criteria are simultaneously implemented in the algorithm for all methods;

(1) Number of maximum allowed iterations is exceeded.

(2) Number of maximum allowed iterations since previous record update is exceeded.

(3) Number of maximum allowed iterations for '$\beta < 0.01$' is exceeded continuously.

(4) None of the last 1000 tried locations is new.

3.5.3. Case Studies

Case Study I: Placement of Single PZT Patch

The successes of the suggested methods above are examined through the placement of a single PZT patch actuator on a square plate to maximize first modal displacement. Optimization parameters used in this problem are given in Table 3.14. Only first stopping criterion is taken into consideration.

Table 3.14. Optimization Parameters

Parameter	Value
maximum allowed number of iterations	27
probability for best estimator and temperature calculation	0.01
Degree of freedom of chi-square distribution (d)	2
number of times to insist on search direction (γ_{max})	1 or 10

The optimization problem is summarized below;

- Maximize : the first modal displacement of plate described in Figure 3.20.

- Model: 10x10 uniform finite element mesh is used to discretize the domain and a 2x2 mesh is used for the piezoelectric patch.

- Design Variables: element-wise x and y locations of patch, x_{loc} and y_{loc} (Figure 3.21).

- Subject to: design variables are bounded by design space; $0 \le x_{loc} \le 8$, $0 \le y_{loc} \le 8$, where x_{loc} and y_{loc} are integer quantities.
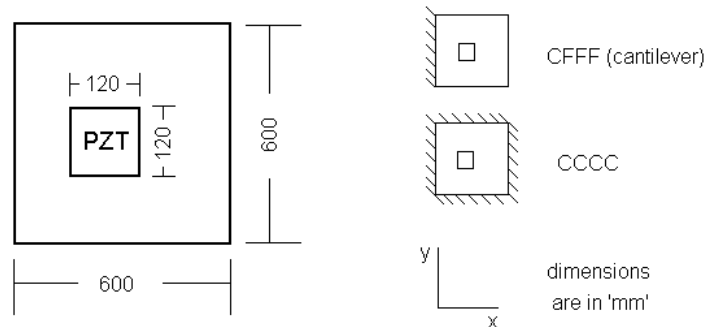
Figure 3.20. Geometry of the plate used in the example problem.
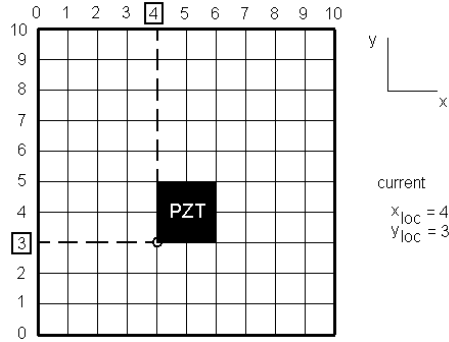
Figure 3.21. Design variables.

Table 3.15. Material properties of the layers.

Layer	Property	Value
Base Plate	Modulus of Elasticity	200,000 Mpa
	Poisson's Ratio	0.3
	Density	$7.8 \ 10^{-9} \ \text{ton/mm}^3$
	Thickness	5 mm
PZT	Modulus of Elasticity	63,000 Mpa
	Poisson's Ratio	0.3
	Density	$7.64 \ 10^{-9} \ \text{ton/mm}^3$
	Thickness	1 mm
	Transverse piezoelectric coefficient (e_{31})	0.01134 N/Vmm
Adhesive	Modulus of Elasticity	4000 Mpa
	Shear Modulus	1400 Mpa
	Thickness	0.1 mm

CFFF (cantilever) Case

In this section, a plate with a single edge clamped with remaining edges free is considered. First modal displacement is the objective function. If we search all the possible patch locations, the resulting normalized objective function is plotted in Figure 3.22. Figure 3.23 shows the best and the worst actuator locations to maximize modal displacement of the first mode.
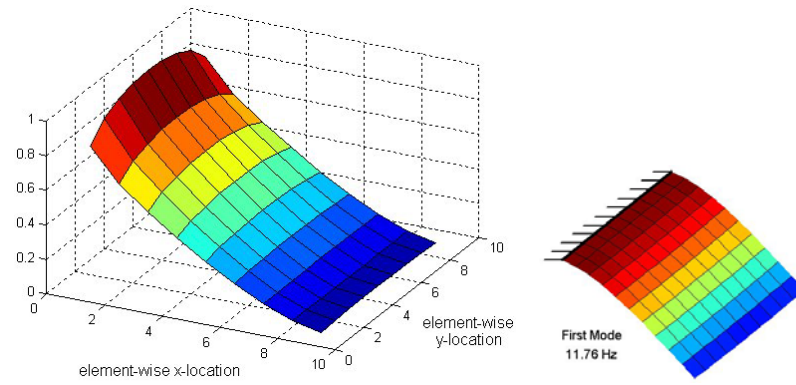
90

Figure 3.22. Plot of objective function versus design variables. Values of the objective function are normalized with respect to maximum. The first mode shape is also shown.
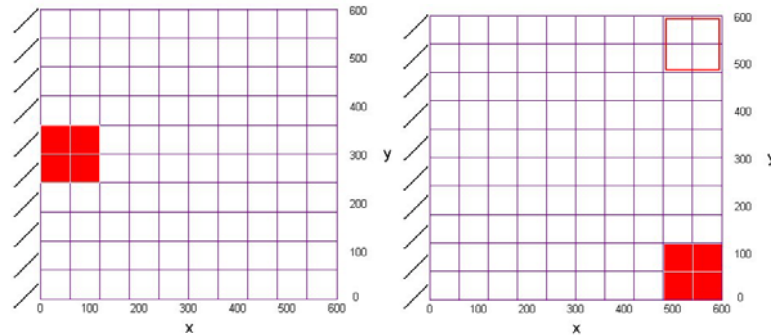

Figure 3.23. Best and worst (two symmetric) patch locations.

In order to compare search methods described in the previous section, 30 computer runs with random initial patch position are conducted for each method. The number '30' is generally assumed to be minimum sample size in order to build up a meaningful statistical hypothesis [56]. Maximum allowable iteration number was set to 27, which is one-third of the number of all possible patch locations, in this case, only one-third of these runs would be successful if the search method is entirely random. However, as seen in Table 3.17, different methods have very different level of successes to find best location of the piezoelectric patch to maximize modal displacement of the first mode. It is seen that in a one-dimensional search, Method III, is much more effective than Methods I and II. It is also observed that insisting on the search direction, by setting γ_{max} to 10, generally improves the effectiveness of the optimization method.

Table 3.16. Comparison of different search methods for CFFF case. Both best and worst locations may be found during a single run.

Total Number of Runs		30		
		number of runs which found best location	number of runs which found worst location	number of average iterations to find maximum*
Expected for Entirely Random Search		10.00	16.75	14.00
Method I	γ_{max} = 1	17	6	16.35
	γ_{max} = 10	14	8	15.86
Method II	γ_{max} = 1	8	6	9.25
	γ_{max} = 10	17	5	14.88
Method III, η=1 and δ_{max}> size of the design space in any direction	γ_{max} = 1	23	16	13.43
	γ_{max} = 10	27	14	12.52
Method III, η=1 and δ_{max}=3	γ_{max} = 1	26	10	14.04
	γ_{max} = 10	25	6	13.84
Method III, η=2 and δ_{max}> size of the design space in any direction	γ_{max} = 1	22	9	14.45
	γ_{max} = 10	26	8	10.92

*Average is taken over the runs where the best location was found

CCCC (4-side-clamped) Case

Similar study is conducted for all sides clamped case. In this case, 'γ_{max}=10' is used. Plot of normalized objective function versus design variables is shown in Figure 3.24. Best and worst patch locations are illustrated in Figure 3.25. Comparison of the methods is given in Table 3.17. As similar to the 1D study in Section 3.5.1, Method III, without a restriction on maximum step size and with uniform distribution for selection of the step size, is not successful since maximum location is at the center of the design space. When examining the effectiveness of the methods from the table, not only the average number of iterations, but also the number of runs which found the worst location should be taken into account. Since it is aimed to find maximum, an effective method should find the minimum less than expected for entirely random search. Method I, Method II and Method III with restricted step size have almost same moderate level of success to find optimum. However, Method III with enhanced probability on selection of closer solutions is much more effective for this case. Note that in this problem, since there is not any local optimum, the possibility of being trapped at a local optima is eliminated for this problem.
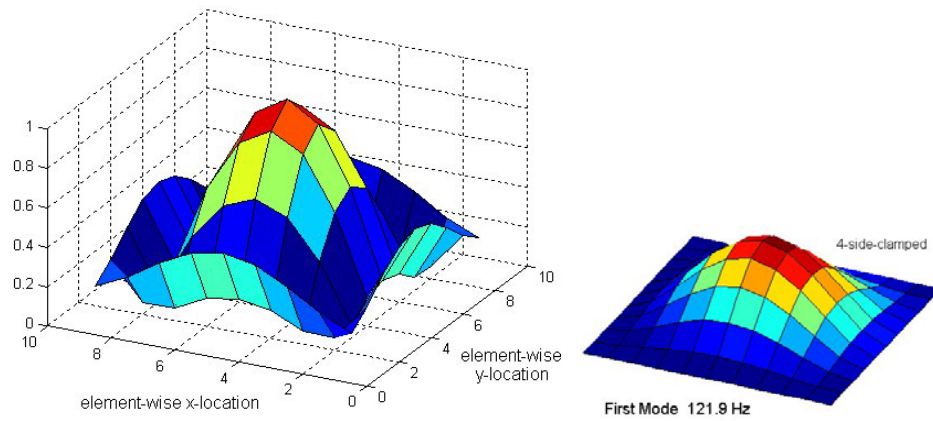
Figure 3.24. Plot of objective function versus design variables and mode shape. Values of the objective function are normalized with respect to maximum.
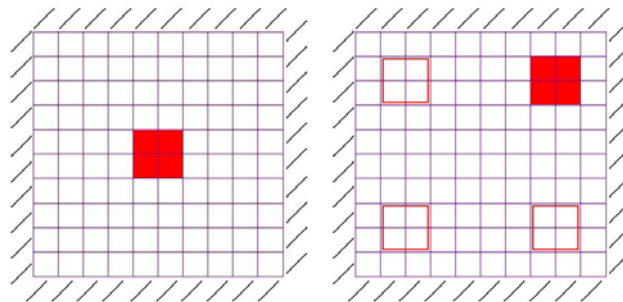

Figure 3.25. Best and worst (four different symmetric) configurations.

Table 3.17. Comparison of different search methods for CCCC case, $\gamma_{max} = 10$. Both best and worst locations may be found during a single run.

Total Number of Runs	30		
	# of runs which found best location	# of runs which found worst location	# of average iterations to find maximum*
Expected for Entirely Random Search	10.00	24.30	14.00
Method I	14	28	17.86
Method II	15	28	12.20
Method III, $\eta = 1$ and δ_{max} > size of the design space in any direction	4	21	20.50
Method III, $\eta = 1$ and $\delta_{max} = 3$	15	22	14.07
Method III, $\eta = 2$ and δ_{max} > size of the design space in any direction	21	16	14.95

*Average is taken over the runs where the best location was found

93

Case Study 2: Placement of Double Piezoelectric Patches on a Cantilevered Plate

Positive and negative potential differences are applied two different patches as shown in Figure 3.26 on cantilevered square base plate. Chosen FE mesh consists of 9x9 elements. Material properties and geometry are same with the previous single-patch case. However, size of the patches is bigger (200mm x 200mm). Plate is clamped from '$x=0$' edge. Maximization of second modal displacement is chosen as objective. Second mode shape is given in Figure 3.27. Optimization parameters are listed in Table 3.18. Comparison of the methods is given in Table 3.19. For Method III, step size is not restricted and probability of choosing closer solutions is increased ($\eta = 2$). It may be also noted that only one PZT patch moves for each iteration step when Method III is used.
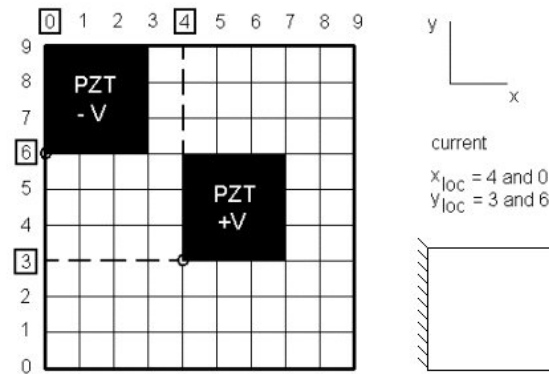
Figure 3.26. Double-patch case and design variables
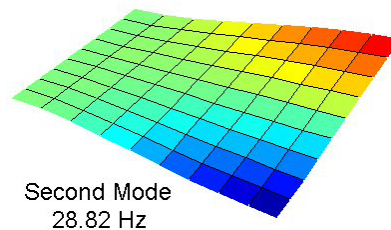
Figure 3.27. Second mode Shape of cantilevered square plate without PZT patches; first torsional mode.

Examining all 1032 combinations, worst and best patch locations found are drawn in Figure 3.28. It may be noted that, best location is on the corner of the design space, which is a 4-dimensional hyper-rectangle. When 30 different runs are conducted with entirely random 129 tries out of 1032 possible configurations to find any one of two symmetric best locations, 7.04 of these runs are expected to be successful. The initial location is selected to be the worst configuration. The maximum number of iterations is taken to be 129. Other optimization parameters used are listed in Table 3.18. Results, given in Table 3.19, show that, Method III is very successful especially comparing the results found for single patch case. However, normal random walk, Method I, and random walk with adaptive step size, Method II, are found to be the least successful approaches finding optimum.

Table 3.18. Optimization Parameters.

Parameter	Value
Maximum allowed number of iterations	129 (1/8 of all combinations)
Probability for best estimator and temperature calculation	0.01
Degree of freedom of chi-square distribution (d)	2 or 4
Maximum allowed step size (δ_{max}), Method III only	> Size of the design space in any direction
Probability distribution parameter for step size (η), Method III only	2
number of times to insist on search direction (γ_{max})	10
Starting Locations	Worst possible configuration

It is also seen that, with Method III, taking degree of freedom of chi-square distribution (d) as 4, all 30 runs are successful. However, in that case, probability of acceptance of any configuration other than current best configuration is almost zero. This situation may cause finding a local optimum instead of global optimum for other problems, which may have many local optima.
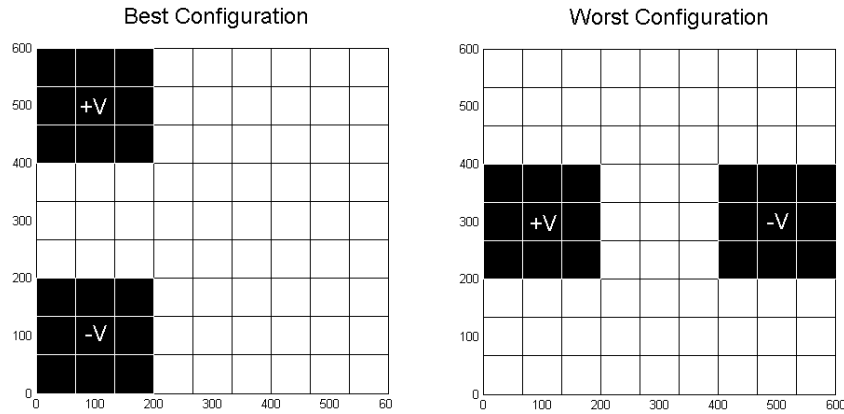
Figure 3.28. Best and worst configurations to maximize second modal displacement.

Table 3.19. Summary of the results for double-patch case. Effect of changing degree of freedom of chi-square distribution (d) is also studied.

Total Number of Runs	30	
	# of runs which find best location	# of average iterations to find maximum*
Expected for Entirely Random Search (129 tries)	7.04	-
Method I, $d=2$	11	66.36
Method I, $d=4$	9	33.78
Method II, $d=2$	11	50.73
Method II, $d=4$	9	40.00
Method III, $d=2$	28	47.61
Method III, $d=4$	30	51.73

*Average is taken over the runs where the best location was found

Case Study 3: Placement of Single Patch When Local Optimum Exists

In this section, Maximization of the seventh modal displacement of the plate having same geometry and material properties, used in Case Study I, is discussed. This mode is intentionally chosen to understand the effect of local optimum on the efficiency of the optimization method. Side length of the square PZT patch is 120 mm. Boundary conditions employed are illustrated and the seventh mode shape is plotted in Figure 3.29. A much denser mesh (15x15) is used to capture the mode shape more accurately. Calculating objective function

for all possible configurations, a surface, representing normalized objective function versus design variables is plotted in Figure 3.30. Besides the maximum iteration number criterion, other stopping criteria are also considered. Optimization parameters are given in Table 3.20.
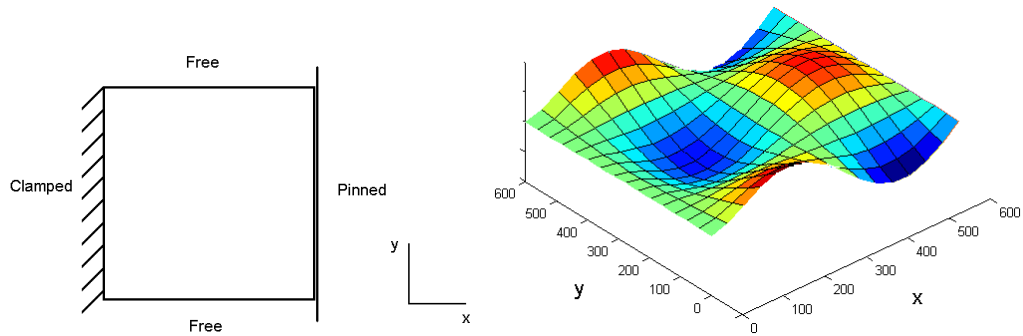

Figure 3.29. Boundary conditions and 7th mode shape of the example plate without any patch.

In Table 3.21, summary of the results obtained using Method II and Method III with three different sets of search method parameters is given. 30 separate runs were conducted in each case. In the first row of the table, number of successful runs out of these 30 runs was given. Average number of total iterations for all runs was given in the second row. In the third row, expected number of successful runs for average number of iterations was given if entirely random search would have used. In the fourth and fifth rows, average numbers of iterations of successful runs are given for total iterations and iterations when optimum was found. Finally, number of runs, which found local optimum but did not find global optimum, is also given.
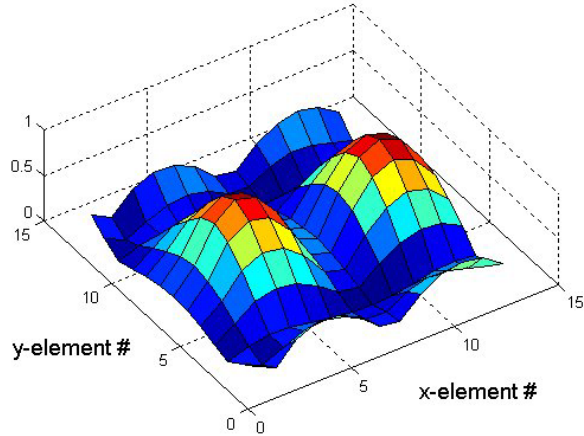
97

Figure 3.30. Normalized objective function versus design variables. Value of the objective at the local optimum is 96.62 percent of the value of the objective at global optimum, which is near the right side of the figure.

Table 3.20. Optimization Parameters.

Parameter	Value
Number of maximum allowed iterations (S1)	100
Number of maximum allowed iterations since previous record update (S2)	40
Number of maximum allowed iterations for $\beta < 0.01$ continuously (S3)	10
Probability for best estimator and temperature calculation	0.01
Degree of freedom of chi-square distribution (d)	2
Number of times to insist on search direction (γ_{max})	10
Starting Location	random

It may be observed from Table 3.21 that, when we use Method II or Method III with restriction on step size, and enhanced probability of selecting new test point from the closer neighborhood better results are obtained. It may also be seen that, average number of iterations required to find global optimum for restricted step size cases are relatively good. On the other hand, number of runs, to find the local optimum, is higher for Method II. In other words, 11 out of 30 runs were trapped at the local optimum for Method II. When number of local optima is higher, this problem may be much worse. Another interesting result may be seen in Table 3.22. When step size is restricted, Method III may not find any other feasible solution around the current accepted solution. 13 out of 30 runs were stopped because of this criterion, when maximum step size was 3. When step

size is restricted with a small value, search is possible only in the relatively small neighborhood of the currently accepted solution. If none of the possible locations in this neighborhood is accepted as new solution, algorithm stops due to this criterion. If maximum step size is not restricted, the method can find a distant solution when all closer solutions are already tried. Therefore none of the runs was stopped because of this criterion as seen in Table 3.22, except from runs whose search step size are restricted. It is also seen that, third stopping criterion, in Table 3.22, generally broke the iterations before the optimum was found. To increase the related optimization parameter, S3 in Table 3.20, may increase the effectiveness of the methods.

Table 3.21. Summary of the results, 30 runs are conducted for each column.

	Method II	Method III					
		δ_{max}	η	δ_{max}	η	δ_{max}	η
		Max. Available	1	3	1	Max. Available	2
Number of successful runs	13	11		12		13	
Average number of iterations	60.70	45.63		45.03		51.67	
Expected number of successful runs for average number of iterations when entirely random search is used	10.78	8.10		7.99		9.17	
Average number of iterations for successful runs	63.23	65.36		50.50		57.15	
Average number of iterations to find the optimum	30.77	39.09		28.08		22.38	
Number of runs to find the local optimum only	11	4		10		8	

Table 3.22. Number of how many times each stopping criterion met for 30 different runs of each three different set of search method parameters. Numbers in the parentheses are for only successful runs.

Stopping Criterion	Method II	Method III					
		δ_{max}	η	δ_{max}	η	δ_{max}	η
		Max. Available	1	3	1	Max. Available	2
	Number of times each stopping criterion met						
Number of maximum allowed iterations	1 (1)	2 (2)		0 (0)		0 (0)	
Number of maximum allowed iterations since previous record update	16 (7)	6 (3)		8 (1)		17 (8)	
Number of maximum allowed iterations for $\beta<0.01$ continuously	13 (5)	22 (6)		9 (2)		13 (5)	
New possible location can not be find	0 (0)	0 (0)		13 (9)		0 (0)	

Discussion on Results

The above case studies on piezoelectric actuator placement, show that, Method I, normal random walk method is generally the worst method when we compare number of the successful runs. For most of the previously considered problems, it provides a minor improvement compared to an entirely random search approach.

In order to have an increase in the efficiency of the method, an adaptive search step size may be used. By establishing a relationship between the temperature, the control parameter of optimization method, and search step size, a better approach to our problems is obtained. A coarse global search at the beginning, when temperature is high, and a fine-tuning search around the global optimum, when temperature is low, increases the efficiency of the optimization method. Press et al.[57] also suggests such an adaptive approach for continuous problems.

Both Method II and Method III are quite successful for the selected case studies with a single piezoelectric patch. It is not a straightforward process to select most suitable method for a specific problem. However, examining the results of the first example, single-patch case, and the second example, double-patch case, it may be stated that Method III is more successful in the second case study. Instead of moving all patches together, moving only one PZT in each

iteration step causes a decrease in randomness of the method and therefore increases the efficiency. Thus Method III is more suitable for multi-patch placement problems. Alternatively, Method II may be modified to prevent changing all design variables at the same time.

3.6. CASE STUDIES ON MAXIMIZATION OF CONTROL EFFECTIVENESS AND MINIMIZATION OF SPILLOVER

3.6.1. Introduction

In this section, beam and plate examples, having different boundary conditions and objective functions, are considered. For all case studies, the modal state vector is selected as given in Equation (3.13).

To conduct multi-objective optimizations, MC-MOSA optimization method [58] developed for continuous multi objective optimization problems, is selected. This method is based on 'Hide and Seek' simulated annealing method. However, unlike single objective case, a population of fitness functions is employed instead of a single cost function. A solution, which improves any of these fitness functions, is accepted. If no improvement is observed, the solution may also be accepted with the probability used in 'Hide and Seek' simulated annealing method. The method is demonstrated to be very effective way in obtaining solutions very close to the actual Pareto fronts [58]. When weighted sum of the objective functions is used to construct a single objective function, any optimization method tries to find a specific solution on the Pareto front. However, if MC-MOSA is used, multi-objective nature of the problem is not lost, and obtained solutions spread the whole Pareto front.

In Appendix B, details of the MC-MOSA Method are given. Since studied problems are discrete, original method is slightly modified. Furthermore, upper and lower bound estimations for objective functions are no more necessary, since non-dimensional objective values are used. The maximum or minimum value of the objective functions, up to previous iteration, is used to non-dimensionalize all past values of the objective functions.

3.6.2. Simply Supported Narrow Plate with Single Piezoelectric Patch

In this case study, maximization of performance index given in Equation (3.38) [52] is aimed. To simulate a simply supported beam type one-dimensional

structure, a two-side simply supported two-side free narrow plate is chosen. Substrate is a steel plate, whose dimensions are shown in Figure 3.31. Then, 'x₁', the distance between the left side and the middle of the patch, is the only design variable. Material properties and thickness are given in Table 3.23. First five modes are taken into account for the reduced model and in the performance index (n=5). Modal damping ratios are assumed as '0.02' in all these modes. 120x1 plate elements of equal dimensions are used to discretize the domain. Without changing this mesh configuration, cost of all possible patch locations are obtained to find the location that maximizes the performance index.
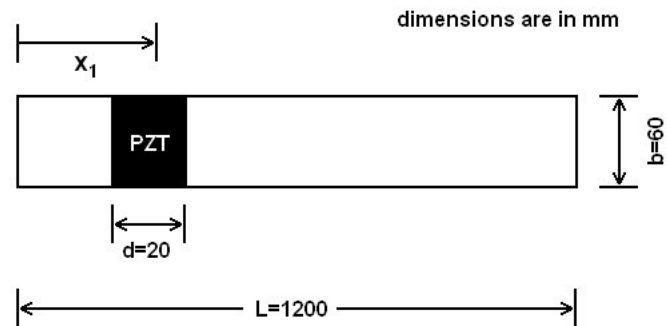
Figure 3.31. Geometry of the narrow plate.
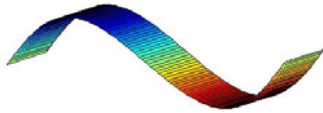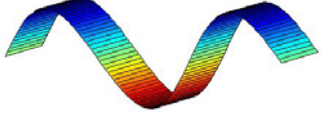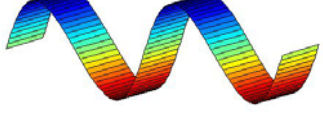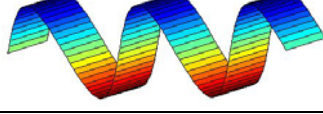
Table 3.23. Properties of the narrow plate

Property	Substrate	Adhesive	PZT
E (Mpa)	200000	4000	63000
v	0.300	0.429	0.300
h (mm)	3.00	0.100	1.00
ρ (ton/mm^3)	7.80 10^{-9}	-	7.64 10^{-9}

First five mode shapes and corresponding modal frequencies are presented in Table 3.24. As seen in the table, effect of the patch on the modal frequencies is quite small. Thus patch does not change the ordering of the modal

frequencies, consequently the modes. Since damping ration of the modes are small and modal frequencies are well spaced, the value of a diagonal element of the controllability grammian is very close to the corresponding controllability grammian eigenvalue associated with the related mode. Therefore, as explained in the above sections [52], instead of the eigenvalues, the diagonal elements may also be used in constructing the performance index, given in Equation (3.38).

Table 3.24. First five mode shapes and undamped natural frequencies of the narrow plate.

Mode Shape	Frequency (Hz), No piezoelectric patch	Frequency (Hz), PZT is on top of the middle region
	4.7843	4.7838
	19.145	19.146
	43.106	43.108
	76.704	76.713
	119.99	120.01

Normalized performance indices for all possible patch locations are plotted in Figure 3.32. As seen in the graph, two symmetric best placements exist at 'x/L =0.125' and 'x/L=0.875'. It is seen that, PI tends to decrease, when middle of the patch approaches the strain node of any mode among the first five modes. However, it is not exactly zero, since patch has a finite length and its location must be restricted with pre-defined mesh configuration. It is also seen that worst

location is the middle of the beam, which is also a strain node of the second and fourth modes.
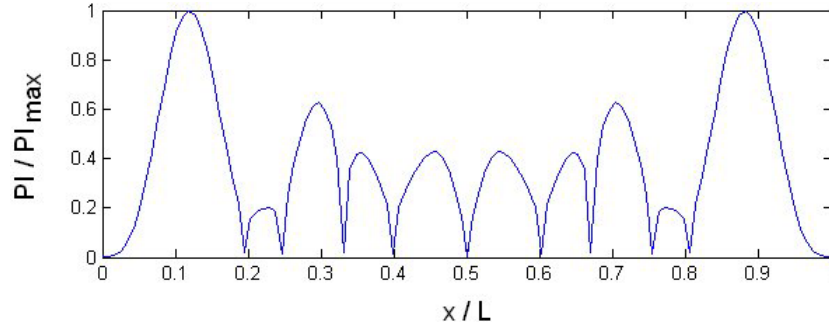

Figure 3.32. Normalized performance index versus patch location. x/L =0.125 and x/L=0.875 are best locations.

3.6.3. Simply Supported Narrow Plate with Double Piezoelectric Patch

In the second example, the goal is to maximize the control on the first 'n_c' modes using two patches, as shown in Figure 3.33. It is also desired to reduce the spillover effects on residual modes. Different performance indices are compared. Number of controlled modes and residual modes are also changed to identify their effects on optimum results. Therefore four different optimization problems are defined. The sum of all eigenvalues weight the highest eigenvalue value, the sixth root of the product of six eigenvalues favors the smallest eigenvalue. In this way a more balanced optimization is expected to be possible. The second objective is related to the two spillover modes. If the same kind of an objective were constructed then the reduction of the spillover of a single mode would be sufficient. In this case, it is also possible to try to minimize the sum of the eigenvalues of the controllability grammian related to control spillover modes. The optimization problems, considered, are listed in Table 3.25. It should be noted that diagonal elements of the controllability grammian are used instead of eigenvalues. To show their closeness, both eigenvalues and diagonal elements of an example case are given in Table 3.26.
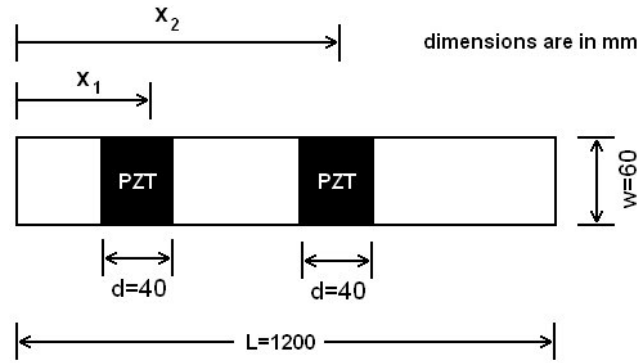
104

Figure 3.33. Geometry of the narrow plate. 'x_1' and 'x_2', distances from the left side to the center of the patches, are design variables.

Table 3.25. Objective functions for selected problems. For all problems; maximize {f_1} and minimize {f_2}.

Problem	Controlled modes	Residual modes	f_1	f_2
P1	1,2,3	4,5	$\left(\sum_{k=1}^{6} W_{C_{kk}}\right)\sqrt[6]{\prod_{k=1}^{6} W_{C_{kk}}}$	$\left(\sum_{k=7}^{10} W_{C_{kk}}\right)\sqrt[4]{\prod_{k=7}^{10} W_{C_{kk}}}$
P2	1,2,3	4,5	$\left(\sum_{k=1}^{6} W_{C_{kk}}\right)\sqrt[6]{\prod_{k=1}^{6} W_{C_{kk}}}$	$\sum_{k=7}^{10} W_{C_{kk}}$
P3	1,2	3,4,5	$\left(\sum_{k=1}^{4} W_{C_{kk}}\right)\sqrt[4]{\prod_{k=1}^{4} W_{C_{kk}}}$	$\left(\sum_{k=5}^{10} W_{C_{kk}}\right)\sqrt[6]{\prod_{k=5}^{10} W_{C_{kk}}}$
P4	1,2	3,4,5	$\left(\sum_{k=1}^{4} W_{C_{kk}}\right)\sqrt[4]{\prod_{k=1}^{4} W_{C_{kk}}}$	$\sum_{k=5}^{10} W_{C_{kk}}$

Material properties are same with the previous example. 60x1 plate elements are used to discretize the domain. Without changing this mesh configuration, total number of the possible configurations is 3192. As a placement constraint, at least one finite element (20 mm) is situated between the patches.

Table 3.26. Diagonal elements and eigenvalues of the controllability grammian of the worst configuration for the second objective of Problem P1.

Mode	State	Diagonal Element (10^{-6})	Eigenvalue (10^{-6})
1	1	2.3792	2.3769
	2	2.3792	2.3792
2	3	34.261	34.192
	4	34.261	34.257
3	5	144.83	144.23
	6	144.83	144.75
4	7	335.21	335.22
	8	335.21	335.28
5	9	525.98	526.06
	10	525.98	526.59

Table 3.27. Values of the objective functions for best and worst configurations. Symmetric configurations of the best and worst solutions are not shown.
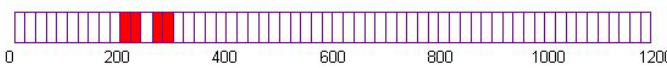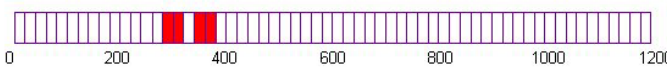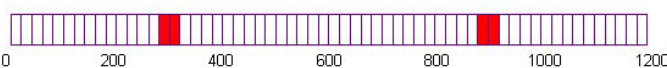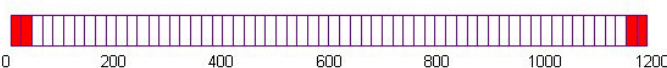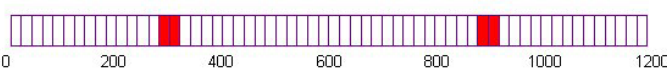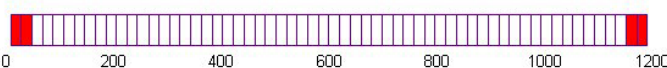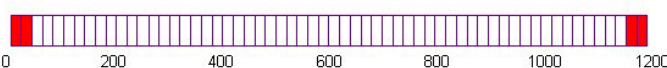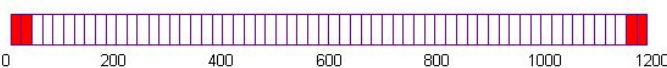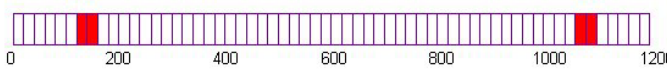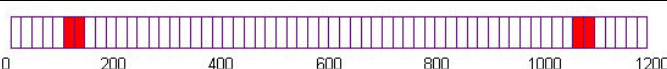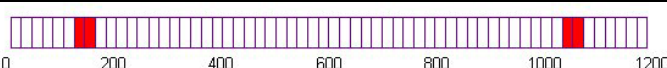
	Problem	x_1	x_2	f_1 (10^{-9})	f_2 (10^{-9})
Best configuration for the first objective	P1	220	280	22.89	40.93
	P2	220	280	22.89	406000
	P3	300	360	5.652	144.9
	P4	300	360	5.652	1192000
Best configuration for the second objective	P1	300	900	14.58	0.0009349
	P2	20	1180	0.01069	128700
	P3	300	900	4.694	0.04738
	P4	20	1180	0.0006646	140300
Worst configuration for the first objective	P1	20	1280	0.01069	3.744
	P2	20	1180	0.01069	128700
	P3	20	1180	0.0006646	2.381
	P4	20	1180	0.0006646	140300
Worst configuration for the second objective	P1	140	1060	8.264	723.2
	P2	120	1080	5.192	1731000
	P3	140	1060	0.6616	592.5
	P4	140	1060	0.6616	2012000

For all problems, best and worst configurations related to selected objectives are given in Table 3.27. Values of the objective functions for these

configurations are also given in Table 3.27. Table 3.28 graphically shows the locations of the patches for best and worst configurations. As seen in the tables, best configuration for the second objective, which minimizes the spillover, for P1 and P3, is also very good solution for the first objective. However for P2 and P4, this situation completely changes. The positions found for minimum spillover is also worst solution for the first objective. This example shows the importance of the definition of the performance index, especially for the objective related to the spillover. When the definitions change, the solutions found for the minimum spillover objective alter significantly as seen in Table 3.27 and Table 3.28.

In Figure 3.34 to Figure 3.37, all the solutions are plotted for the above bi-objective problems. Although number of possible configurations is same for all problems, different number of Pareto solutions is obtained as shown in Table 3.29. However fewer Pareto points can be counted from the plots since some points are very close to each other. Values of the objective functions are normalized with respect to their absolute maxima.

Table 3.28. Best and worst configurations for selected objectives. There are also symmetric configurations of these solutions. Shaded areas are actuator locations.

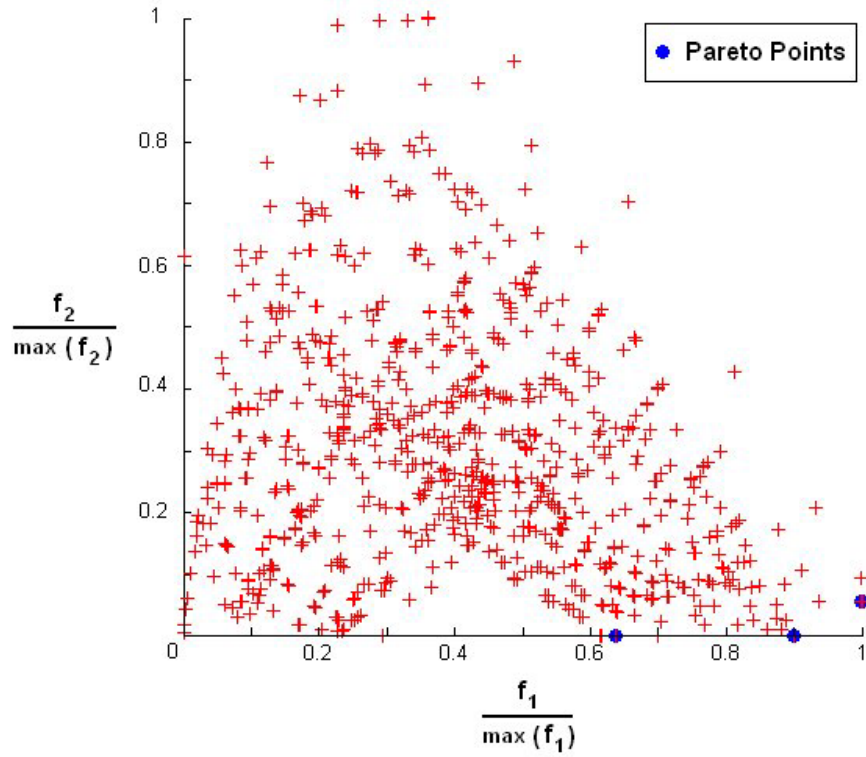|	Problem	Configuration
Best configuration for the first objective	P1, P2	
	P3, P4	
Best configuration for the second objective	P1	
	P2	
	P3	
	P4	
Worst configuration for the first objective	P1, P2	
	P3, P4	
Worst configuration for the second objective	P1	
	P2	
	P3	
	P4	

108

Figure 3.34. Control effectiveness versus spillover, Problem P1. Maximization of the first objective and minimization of the second objective are aimed.

Table 3.29. Number of Pareto points.

Problem	Number of Pareto points
P1	6
P2	16
P3	16
P4	42
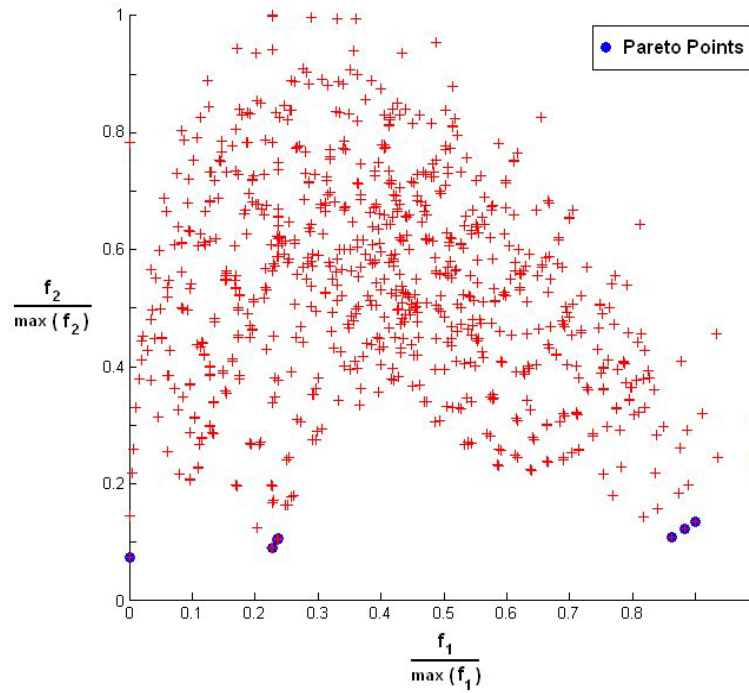
Figure 3.35. Control effectiveness versus spillover, Problem P2. Maximization of the first objective and minimization of the second objective are aimed.
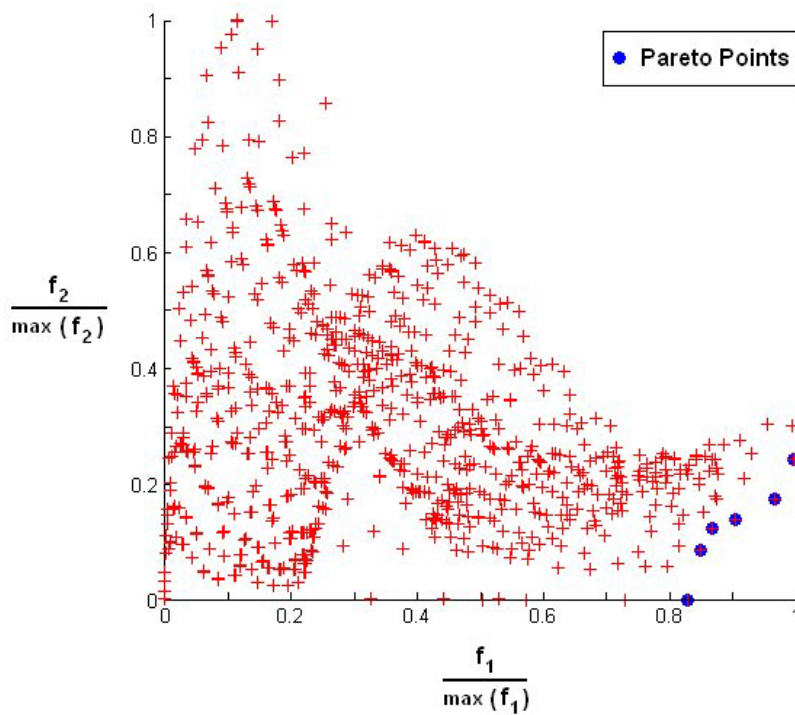

Figure 3.36. Control effectiveness versus spillover, Problem P3. Maximization of the first objective and minimization of the second objective are aimed.
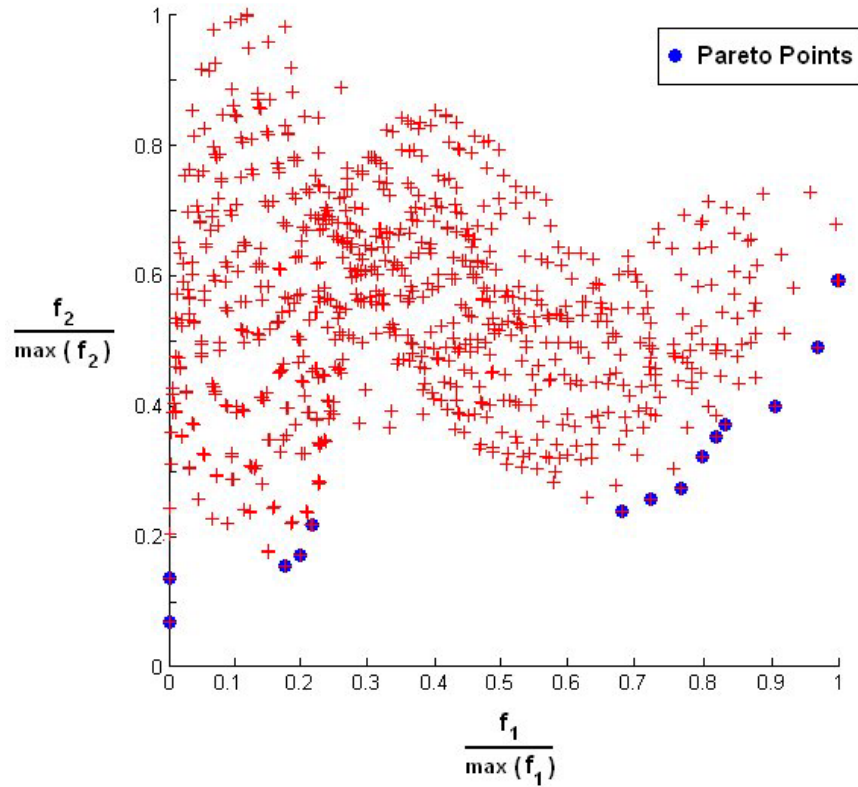
Figure 3.37. Control effectiveness versus spillover, Problem P4. Maximization of the first objective and minimization of the second objective are aimed.

3.6.4. Cantilevered Plate with a Double Piezoelectric Patch

A cantilever plate, having two piezoelectric patches bonded on the surface, is investigated. 12x6 plate elements are used to model the structure. Geometry and discrete design variables are shown in Figure 3.38. Without changing pre-defined finite element mesh, 2094 different configurations are possible, including symmetric configurations. Although material properties are same with the previous beam examples, modal damping ratios are selected higher and given in Table 3.30. Contrary to the narrow plate example considered above, the modal frequencies are affected when piezoelectric patches are added to the model (Table 3.31). However, since frequencies are well spread, the order of the modes does not change for different configurations. This makes it easy to select the modes for later selection of the controllability grammian eigenvalues.

111

These five modes are also used in the reduced model. It is desired to effectively control of the first four modes while minimizing the spillover on the fifth mode. Therefore objective functions are;

$$\text{maximize} \left\{ \left(\sum_{k=1}^{8} W_{C_{kk}} \right) \sqrt[8]{\prod_{k=1}^{8} W_{C_{kk}}} \right\}$$

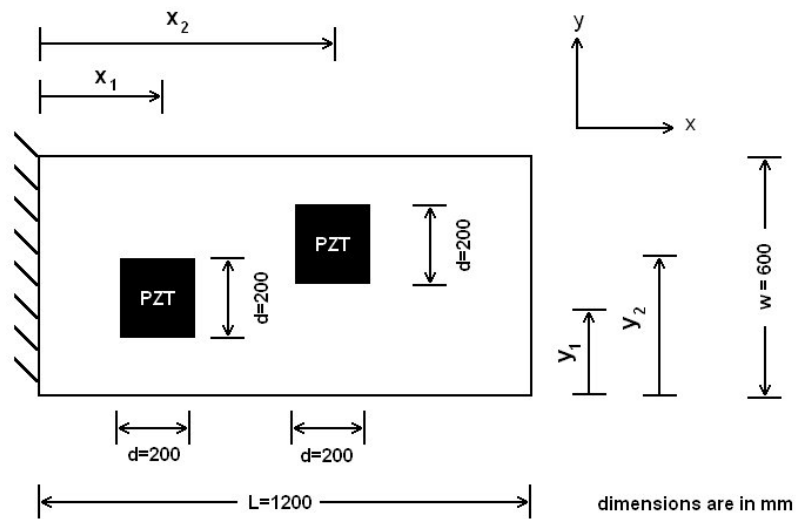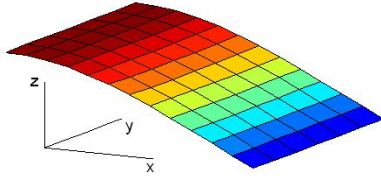$$\text{minimize} \left\{ \left(\sum_{k=9}^{10} W_{C_{kk}} \right) \sqrt{\prod_{k=9}^{10} W_{C_{kk}}} \right\}$$
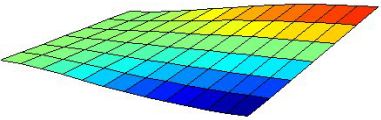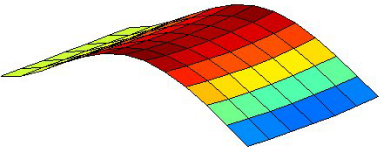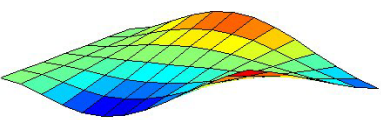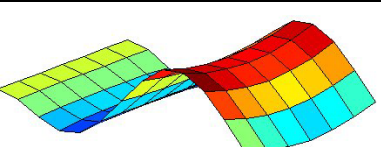

Figure 3.38. Geometry of the cantilever plate. 'x₁', 'x₂', 'y₁' and 'y₂', measured from the centers of the patches, are discrete design variables, which confine pre-defined finite element mesh.

Table 3.30. Modal damping ratios.

Mode	Modal damping ratio
1	0.10
2	0.06
3	0.04
4	0.02
5	0.02

Table 3.31 First five mode shapes and undamped natural frequencies of cantilevered plate. Coordinates axes shown for first mode is also used to plot other modes.

Mode Shape	Frequency (Hz), No piezoelectric patch	Frequency (Hz), 2 PZTs whose location maximizes control
mode 1: first bending	1.748	1.883
mode 2: first torsion	7.523	7.923
mode 3: second bending	10.89	11.42
mode 4: second torsion	24.49	25.64
mode 5: third bending	30.57	31.55

Best and worst locations for selected objectives are shown in Figure 3.39. As seen in the figure, worst configuration for the first objective does not have any control on the torsional modes. On the other hand, configuration, which maximizes the first objective, is particularly effective in controlling the first bending and torsional modes. Since only one mode, third bending, is selected as the residual mode, the configurations, which maximize and minimize the second objective, are clearer. When middle of the piezoelectric patches are on the strain node line, there is very small amount of spillover on that mode. Theoretically this

value would be zero. However, in addition to numerical inaccuracies, finite length of the patch creates some spillover. For best placement case of the second objective, i.e. effectively controlling the third bending patches are on the wave crests as expected. As seen in Table 3.32, and Pareto Plot (Figure 3.40), best configurations for both objectives are not good solutions for other objective. Especially for the configuration, which maximizes the control, the spillover is very high. On the other hand, value of the first objective for minimum spillover configuration is about 9 times less than the maximum. Therefore, a practical solution of the problem is probably another Pareto point, excluding the configurations given in Figure 3.39.
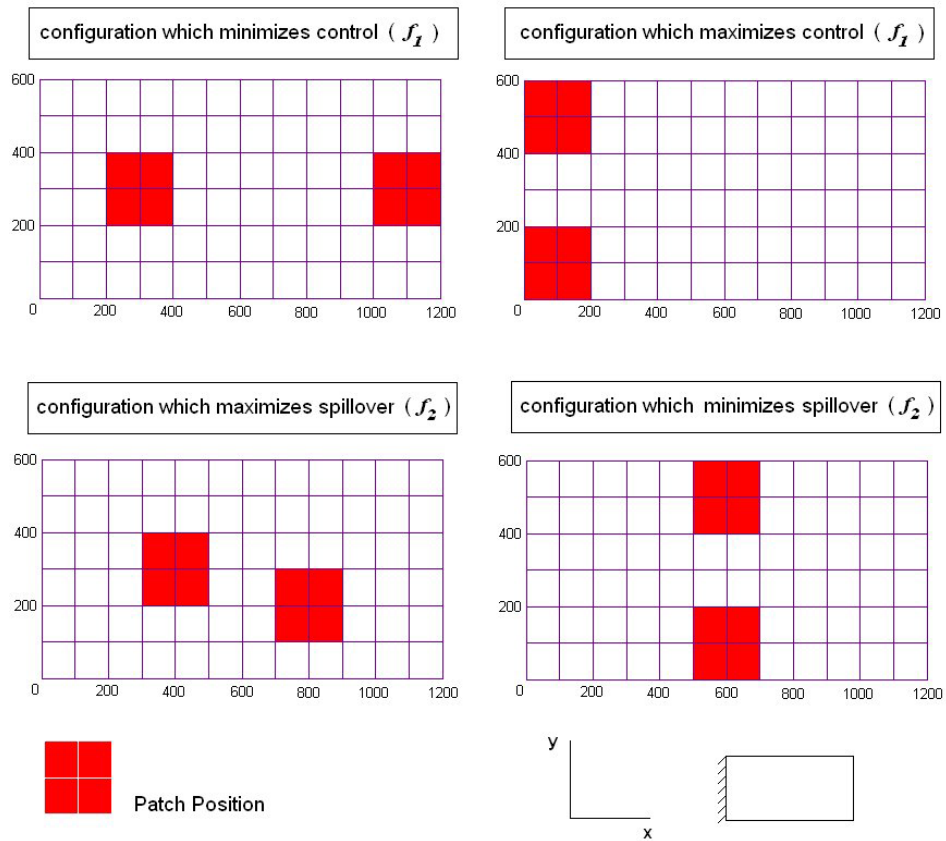

Figure 3.39. Best and worst configurations for selected objectives.

114

Table 3.32. Values of the discrete design variables and objective functions for best and worst configurations. Symmetric configurations of the best and worst solutions are not considered.

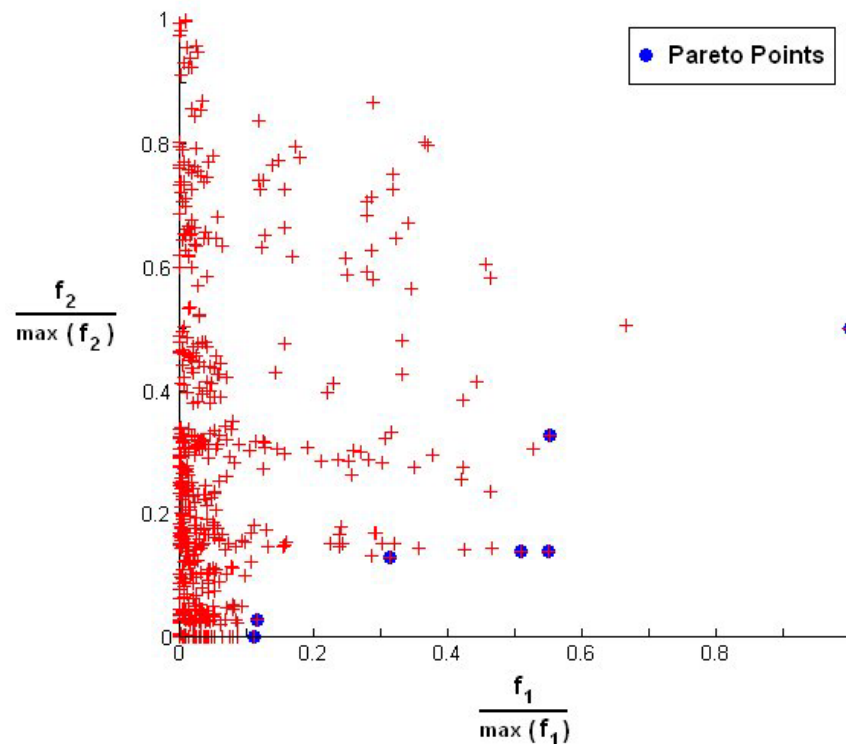|	x_1	x_2	y_1	y_2	f_1 (10^{-6})	f_2 (10^{-6})
Best configuration for the first objective	100	100	100	500	9.421	64.16
Best configuration for the second objective	600	600	100	500	1.067	0.00009460
Worst configuration for the first objective	300	1100	300	300	0.0000	21.16
Worst configuration for the second objective	400	800	300	200	0.08819	128.1

Figure 3.40. Pareto and other solutions in the objective space. There are totally 10 Pareto solutions, although, less points can be counted from the plot since some solutions are very close to each other. Values of the objective functions are normalized with respect to their absolute maxima. Maximization of the first objective and minimization of the second objective are aimed.

3.6.5. Two-Side-Clamped, Two-Side-Free Plate

In this example, a rectangular plate with two piezoelectric patches, shown in Figure 3.41, is studied. Properties of the substrate, adhesive layer and piezoelectric patch are given in Table 3.23. Modal damping ratios are also selected same with the previous example (Table 3.30). This geometry and the boundary conditions are especially chosen to eliminate the symmetric solutions. Different sizes of the patches also enhance this unsymmetrical situation. In other words, each possible placement of the patches is unique since there is no symmetry line in terms of the locations. Since, Pareto solutions found on the actual front are used to measure how successful the method is, it is not desired to have symmetrical solutions. Although existing numerical errors are very small, they affect the number of Pareto solutions. For instance, let Point A be a Pareto solution, which is shown in Figure 3.42, and let B a geometrically symmetric solution of A. Ideally, these solutions coincide, however, due to numerical errors, Solution B may be in any of the four quadrants with the equal probability. For two of these four possibilities, one of the solutions dominates the other solution and there exists only one Pareto solution. On the other hand, for the other possibilities, there exist two Pareto solutions. Therefore, there is an obvious uncertainty for the number of the Pareto solutions due to geometrical symmetry.

An 10x8 regular FE mesh is used for all configurations: Then, our design variables, shown in Figure 3.43, are discrete while they can be also expressed as;

$$
\begin{aligned}
x_1 &= 100(p-1) & p &\in \{1,2,..,8\} \\
x_2 &= 100(r-1) & r &\in \{1,2,...,9\} \\
y_1 &= 100(s-1) & s &\in \{1,2,...,6\} \\
y_2 &= 100(t-1) & t &\in \{1,2,...,7\}
\end{aligned}
$$

Furthermore, at least a single finite element exists between the patches, which may also be assumed as a constraint. Therefore, total number of all possible patch locations is only 1764.
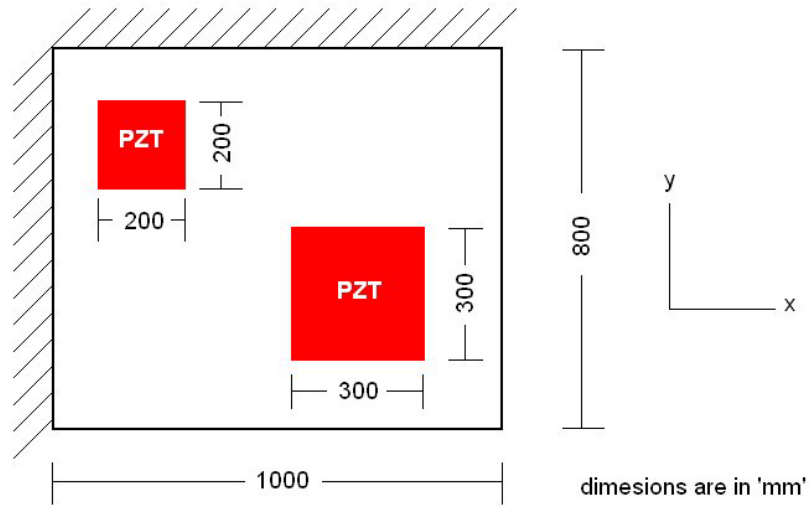
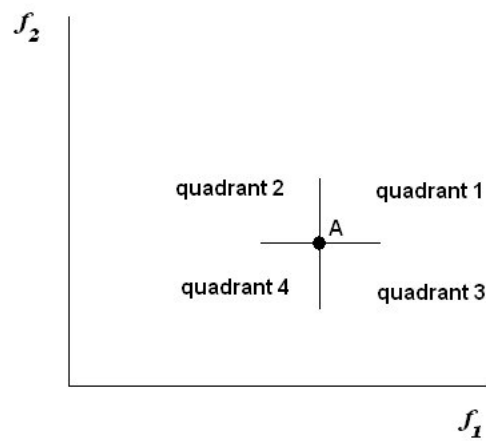Figure 3.41. Geometry of the substrate and the patches.

Figure 3.42. Symmetric solutions in objective space may affect the total number of Pareto solutions due to numerical inaccuracies.
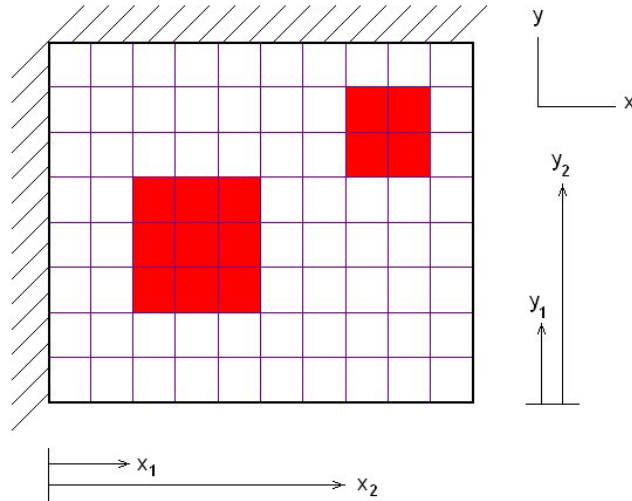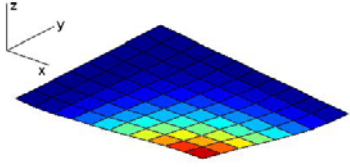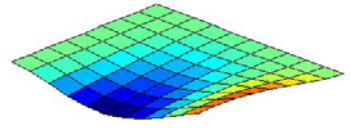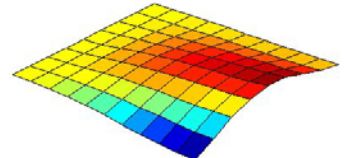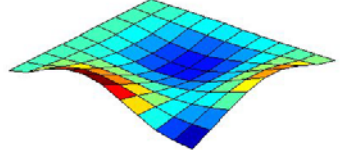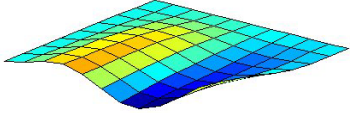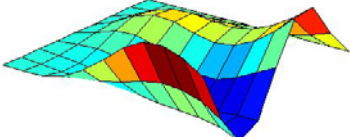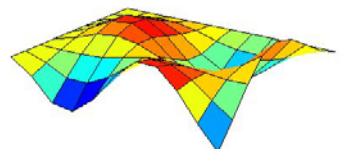
Figure 3.43. Design variables.

In Table 3.33, mode shapes and the frequencies of the base plate without any patch and two other configurations, shown in Figure 3.44, are compared. These two configurations are especially selected, since for Configuration-A, effect of the patches on the stiffness is very important whereas for configuration B, masses of the patches play an important role on the dynamic response of the structure. As seen in the table, frequency wise ordering modes do not change. In addition, corresponding shifts on the frequencies are quite small. Although frequencies of the sixth and seventh modes are close to each other, a change in the order of the modes does not affect the values of objective functions since both of them are selected as residual modes. The objective function related to spillover is defined as the sum of the diagonal elements of the controllability grammian. Since the weights defined in Equation (3.40), are selected to be unity, any change in the order of the residual modes does not affect the value of the related objective function.

Table 3.33. Mode shapes and the frequencies of the base plate and two other configurations shown in Figure 3.44.

Mode	Mode Shape	Frequency (Hz)		
		without any patch	Config.-A	Config.-B
1		6.475	6.608	5.977
2		19.82	20.06	19.42
3		27.55	28.19	27.26
4		44.29	45.39	45.29
5		48.40	49.46	48.87
6		71.91	73.17	73.51
7		74.13	76.71	76.72
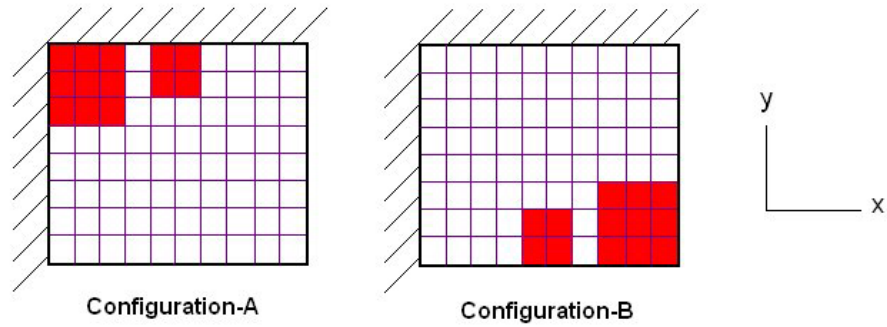
Figure 3.44. The configurations used in Table 3.33.

In Table 3.34, two different sets of objective functions used are given. The difference between the two problems P1 and P2 is the number of the residual modes. Therefore, the first goal is to investigate the effect of the spillover on the Pareto solutions for different number of the residual modes. Another goal of this study is to employ the multi-objective optimization algorithm MC-MOSA, while comparing different search techniques. These are pure randomwalk and one-dimensional randomwalk. For one-dimensional randomwalk technique, only one patch at a time may change its position. It is seen that, this search technique is more successful as before. Optimization parameters and initial values of the problems are given in Table 3.35. Also given are the parameters used in two different search techniques, which are abbreviated as ST1 and ST2.

Table 3.34 Objective functions (for both problems maximize $\{f_1\}$ and minimize $\{f_2\}$).

Problem	Controlled modes	Residual modes	f_1	f_2
P1	1,2,3	4,5	$\left(\sum_{k=1}^{6} W_{C_{kk}}\right)\sqrt[6]{\prod_{k=1}^{6} W_{C_{kk}}}$	$\sum_{k=7}^{10} W_{C_{kk}}$
P2	1,2,3	4,5,6,7	$\left(\sum_{k=1}^{6} W_{C_{kk}}\right)\sqrt[6]{\prod_{k=1}^{6} W_{C_{kk}}}$	$\sum_{k=7}^{14} W_{C_{kk}}$

Table 3.35 Optimization parameters and other definitions used in the problems.

Number of all combinations	1764
Number of allowed iterations	441
Initial location (x_1, y_1, x_2, y_2)	100,400,800,0 Worst configuration for the first objective
Minimum number of the elements between the patches	1
p (probability used when estimating the best)	0.99
d (chi-square dof)	2
Search Technique 1 (ST1)	Pure randomwalk
Search Technique 2 (ST2)	1-Dimensional randomwalk, no restriction on the step size, uniform distribution is used for step length, Hide and Seek type cooling

In Figure 3.45, solutions found for all combinations and solutions of the MC-MOSA (ST1) are given for Problem P1. Actually, three different runs are conducted using MC-MOSA algorithm. The solutions, presented in Figure 3.45, are the results of the second run. In Figure 3.46, the frontal solutions are given only. Summary of the results of these three runs is given in Table 3.36. Although among the three runs, the first run is the least successful, as seen in the plot, obtained front is very close to real front. Since number of the iterations is one-fourth of the all possible configurations, expected number of solutions to be found on the actual front for an entirely random search would have been 5.5. Therefore, average number of solutions obtained on the real front is 2.4 times better according to entirely random search approach.

Table 3.36. Number of total Pareto points found for each run (ST1). First run is compared with the results of full combination in Figure 3.45.

Run #	# of total Pareto points	# of Pareto points on the actual front
Full Combination	21	21
1	14	9
2	12	11
3	19	19
Average of 3 runs	15.00	13.00
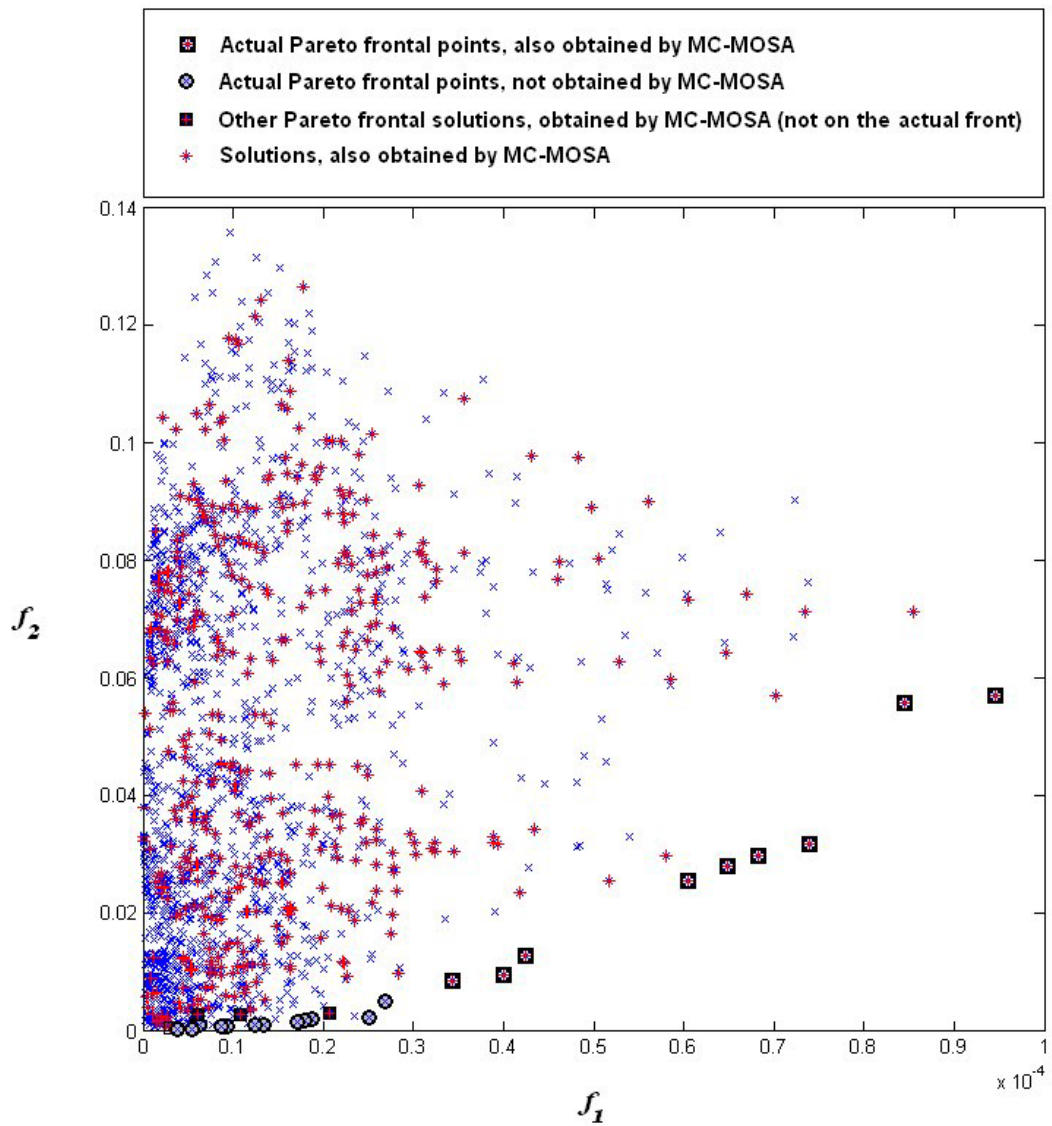
Figure 3.45. Pareto frontal solutions and other solution in objective space. Frontal solutions, obtained by MC-MOSA Method with ST1 (Table 3.35), are compared with the actual front (P1, Run 1). Maximization of the first objective and minimization of the second objective are aimed.

122
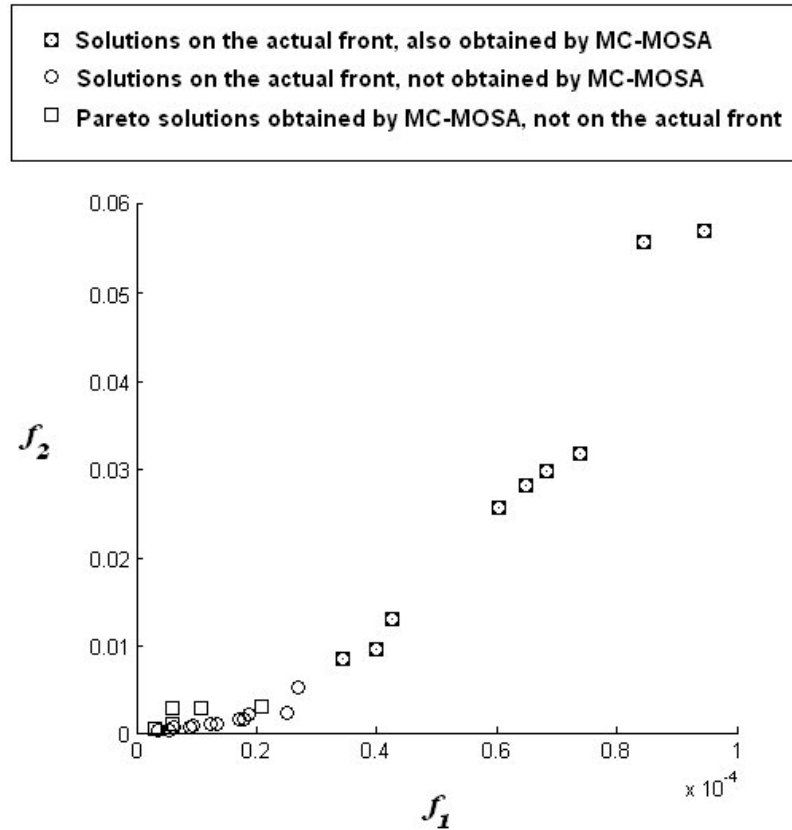
Figure 3.46. Comparison of the Pareto frontal solutions (P1, ST1, Run 1). Maximization of the first objective and minimization of the second objective are aimed.

On the other hand, when ST2 (Table 3.35) is used, the success of the method to find the actual frontal points is improved as seen in Table 3.37. In this case average number of solutions obtained on the real front is 2.7 times better compared with an entirely random search approach.

Table 3.37. Number of total Pareto points found for each run (ST2).

Run #	# of total Pareto points	# of Pareto points on the actual front
Full Combination	21	21
1	17	15
2	17	17
3	13	12
Average of 3 runs	15.67	14.67

In the second part of this example, effects of adding more residual modes on Pareto solutions are investigated. In other words, frontal solutions of Problems P1 and P2 are compared. For comparison purposes, solutions are normalized with respect to their maximums and plotted in Figure 3.47. Fronts obtained for dimensional results are also given in Figure 3.48. Since all combinations are considered for both problems, Pareto solutions presented in these figures are on the actual fronts. As seen in the graphs, not only the front obtained from dimensional solutions, but also the front obtained for non-dimensional results is affected when number of the residual modes is increased. Since, the sum of the diagonal elements of the controllability Grammian is directly used to measure the spillover, the effect of the modes having higher frequencies are generally higher. In other words, since all weights are assumed as '1' in Equation (3.40), importance of the higher frequency modes is automatically increased. Therefore, added residual modes for Problem P2, sixth and seventh modes have the most significance on the results and Pareto fronts. As seen in Figure 3.47 and Figure 3.48, their contributions on the frontal solutions are not negligible. It may be also noted that, number of the Pareto points are also changed. For Problem P1, number of Pareto solutions on the actual front is 21, whereas it reduces to 17 for Problem P2.

Figure 3.47. Comparison of the non-dimensional Pareto frontal solutions (P1 and P2).
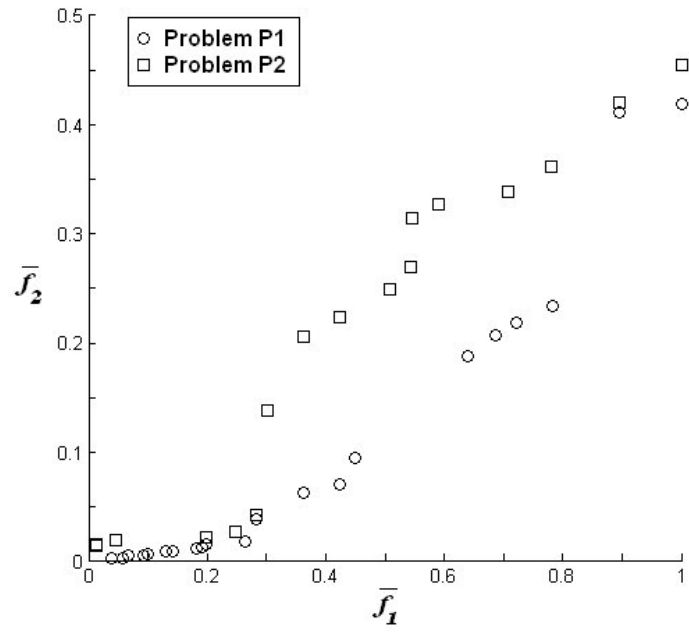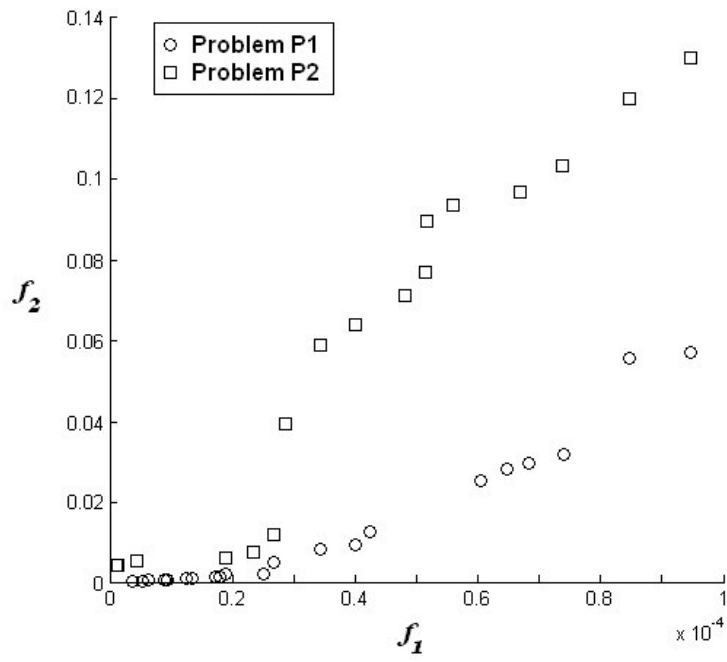

Figure 3.48. Comparison of the Pareto frontal solutions (P1 and P2).

3.7. MAXIMIZATION OF THE ACTUATION EFFECT OF PIEZOELECTRIC LAYER BY A PROPER BONDING GEOMETRY

3.7.1. Introduction

Instead of bonding the entire contact surface of the actuator, introducing a proper bonding geometry may be quite advantageous in some cases. Especially when;

- Stiffness of the actuator(s) is comparable with substrate;
- Many actuators mean a multi input – multi output system, with complicated control algorithms;
- Actuator already covers whole substrate and location is not a design variable;
- Re-distribution of actuation forces due to unbonding increases the control effectiveness. Then the desired control may be achieved by a single input – single output system.

Since it needs more effort to control a stiffer structure, when stiffness of the actuator is comparable with the rest of the structure, it may introduce an extra difficulty because of the actuator itself. However, by creating a proper debonding region between the actuator and substrate, stiffness of the whole system may be decreased substantially. For multi objective placement problems, some Pareto solutions may be one of the worst solutions for one or more objectives. In those cases, introducing a debonding region may improve the value(s) of the worst objective(s) an important amount without deteriorating the value(s) of the best objective(s). For example, to control first bending mode of a narrow cantilever plate, best actuator position is shown as Configuration-A in Figure 3.49. Having any actuation effect to control first torsional mode with this configuration is not possible. However, creating a debonding region between the patch and substrate makes this mode controllable without diminishing the controllability of the first bending mode.

For better demonstration of these ideas two case studies are presented in sections 3.7.2 and 3.7.3 It may be noted that contribution of the actuator to the stiffness of the whole system is quite high in these examples. Furthermore, since whole top layer is an actuator, location is not a design variable.

126
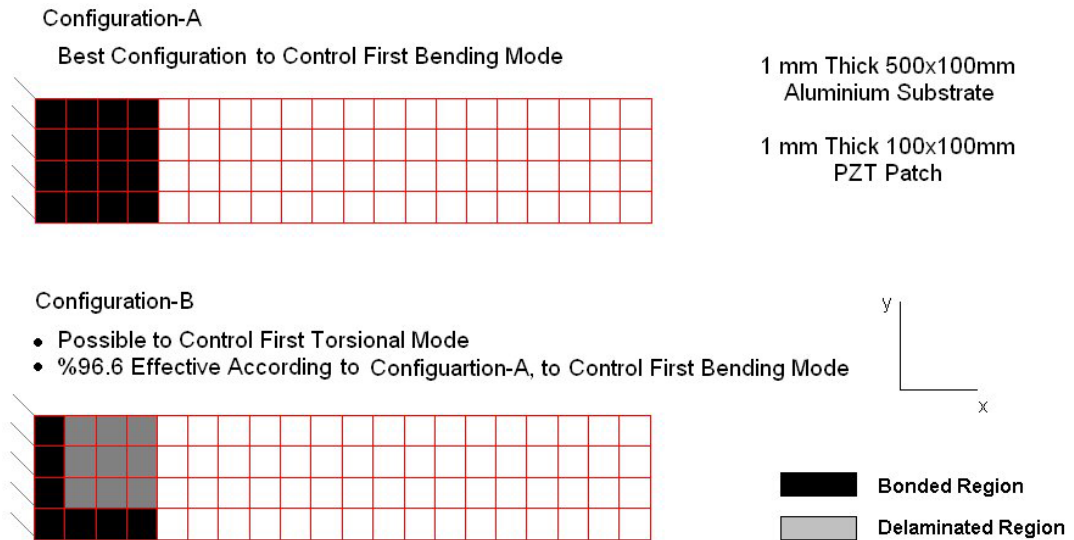
Figure 3.49. Introducing a proper debonding region between the piezoelectric patch and substrate, it is possible to control previously uncontrolled first torsional mode, without loosing an important amount of actuation effect on first bending mode.

3.7.2. Case Study I: Maximization Of Tip Displacement Of Square Cantilever Plate With Defining Proper Bonding Region

Maximization of static transverse displacement at the center of free edge, Point A on midplane of the substrate shown in Figure 3.50, is considered as design objective. Material properties of the layers are given in Table 3.38. Optimization problem may be defined as;

Objective: Maximize transverse displacement at point A (Figure 3.50).
Design Variables: Discrete (element-wise) size and location of the rectangular unbonded region (Figure 3.51)

Deformed shape when potential difference is applied on actuator for fully bonded case is given in Figure 3.52. Best sixteen configurations are found as shown in Figure 3.53 after examining all 3025 possible configurations. It should be also noted that, among all configurations, fully bonded actuator is the 275th best solution. Percentage of improvement when compared to the fully bonded case is given in Figure 3.53 for first eight best cases. From the results, it is clear that the amount of improvement is quite small.
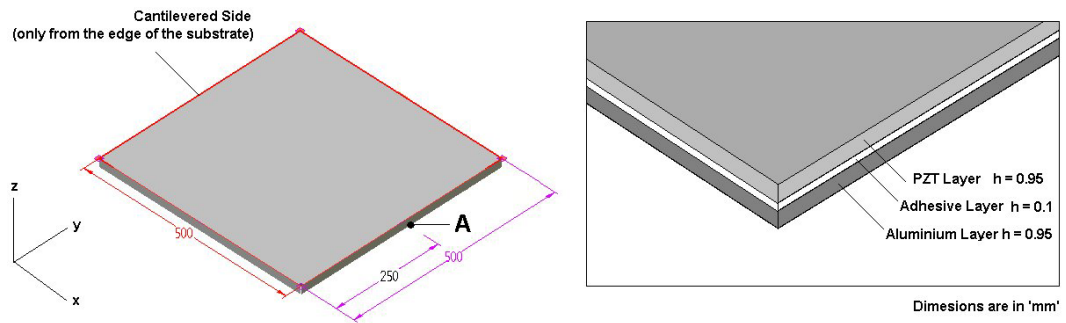
Figure 3.50. Geometry of the problem.

Table 3.38. Material properties of the layers.

Layer	Property	Value
Base Plate	Modulus of Elasticity	70,000 Mpa
	Poisson's Ratio	0.3
	Density	$7.8 \ 10^{-9}$ ton/mm^3
PZT	Modulus of Elasticity	63,000 Mpa
	Poisson's Ratio	0.3
	Density	$7.64 \ 10^{-9}$ ton/mm^3
	Transverse piezoelectric coefficient (e_{31})	0.01134 N/Vmm
Adhesive	Modulus of Elasticity	4000 Mpa
	Shear Modulus	1400 Mpa
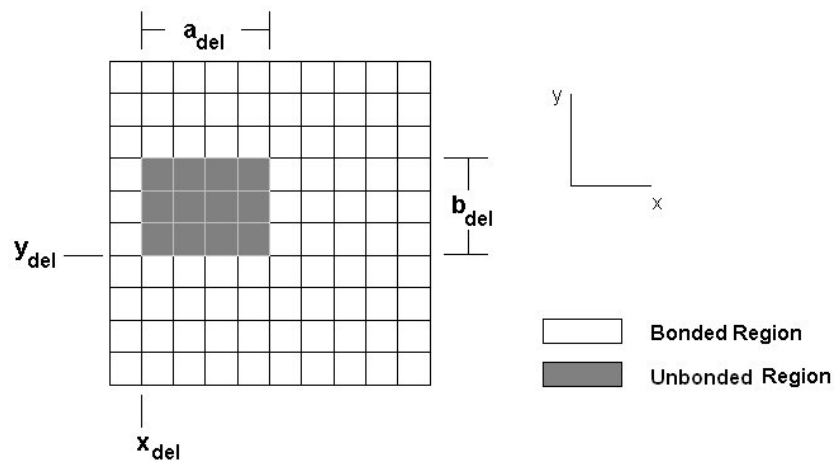
Figure 3.51. Design variables.

128

To verify the above results, MSC.NASTRAN model of best configuration (Figure 3.54) is created and its top layer is thermally loaded to simulate the behavior of the piezoelectric material. 3D brick elements are used to model aluminum substrate, adhesive layer and PZT layer separately. Coefficient of thermal expansion for substrate and adhesive layers are selected to be zero. The only difference between applied loading and potential difference loading is the existing strain in the transverse direction due to thermal expansion. However, since top layer is very thin, its effect on displacements was negligible.
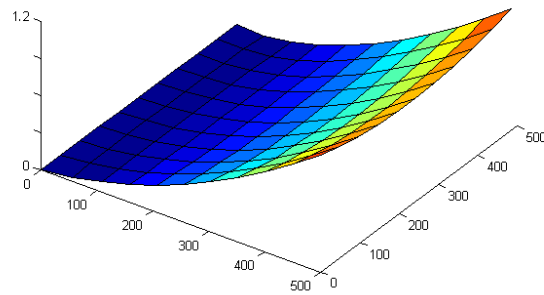
Figure 3.52 Deformed shape when potential difference is applied on PZT layer for fully bonded cases. Displacements are normalized with respect to transverse displacement of Point A.
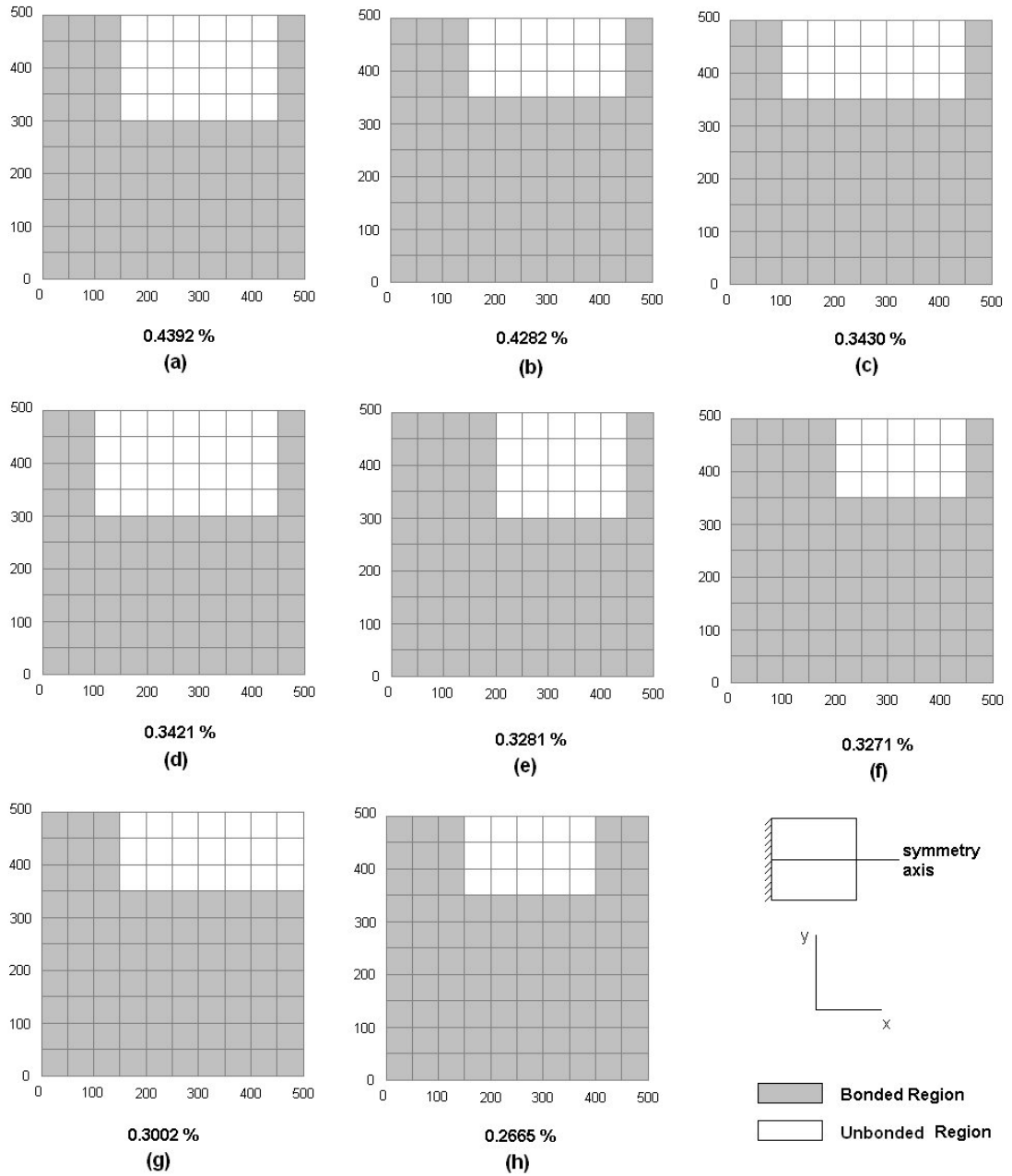
Figure 3.53. First sixteen best configurations (symmetric solutions are not shown). Percent values shows that how much that configuration is better than the fully bonded case which is 275th best solution out of 3025 possible configurations.

130
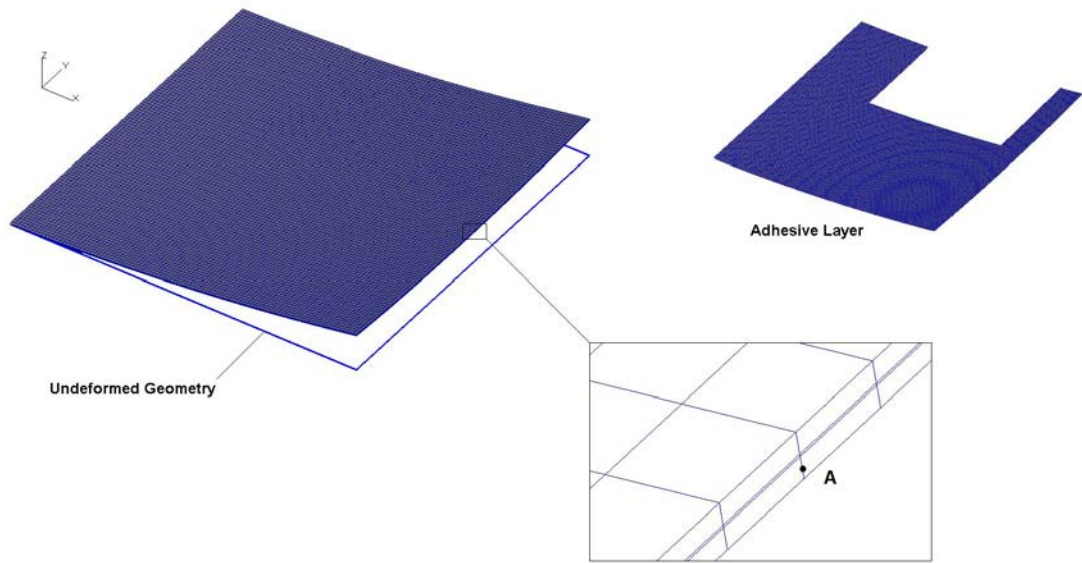
Figure 3.54. Deformed shape of MSC.NASTRAN model. 3D brick elements are used to model aluminum substrate, adhesive layer and PZT layer separately. Instead of applying potential difference on PZT layer, thermal loading analogy is used.

Comparison of MLP-FAB model and MSC.NASTRAN model is given in Table 3.39. Although improvement estimated with the solid model is better, it is still not an important amount. It is also seen that, with increasing mesh density, the difference between the MLP-FAB and solid model becomes smaller.

Table 3.39 Percent improvement of the transverse displacement according to fully bonded case

Model	Percent difference of transverse displacement at point A of the Configuration-(a)* and fully bonded case
10x10 MLP-FAB	0.4392
20x20 MLP-FAB	0.5343
100x100x3 Solid Model	0.6933

* see Figure 3.53 (a).

Here only a single rectangular unbonded region is allowed. However, there may be other possible solutions, which further improves objective function. For example, configuration shown in Figure 3.55 creates extra 0.2266 %

transverse displacement as compared to Configuration-(a) when 10x10 mesh size is used. In total 0.6758 % improvement according to fully bonded case is obtained. However, acquired benefit associated with the unbonding is still quite small for the selected objective.
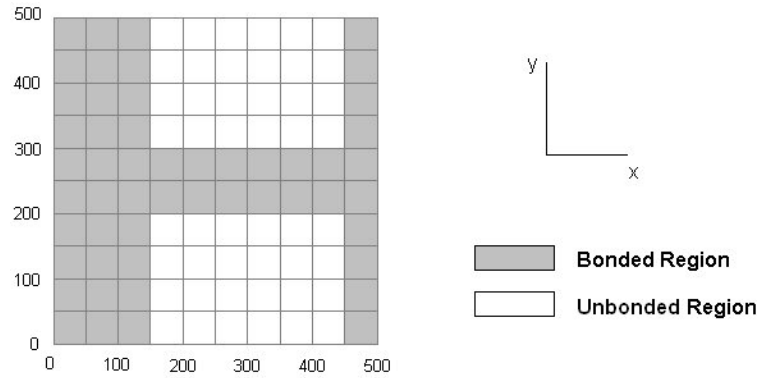
Figure 3.55. Configuration shown above creates extra 0.2266 % transverse displacement according to Configuration I. Totally 0.6758 % improvement according to fully bonded case is obtained.

3.7.3. Case Study II: Combined Maximization of Three Modal Displacements of Square Cantilever Plate

Maximization of modal displacements of first bending, first torsional and second bending modes are objectives. Mode shapes of these three modes for a fully bonded case are given in Figure 3.56. Material properties and geometry are same with the properties of the example given in Section 3.7.2. Optimization problem may be defined as;

Objectives: Maximizing the modal displacements of first bending, first torsional and second bending modes.

Design Variables: Size and location of the rectangular unbonded region (Figure 3.51).

Constraints: Unbonding of the layers in the regions, shown in Figure 3.57, are not allowed.
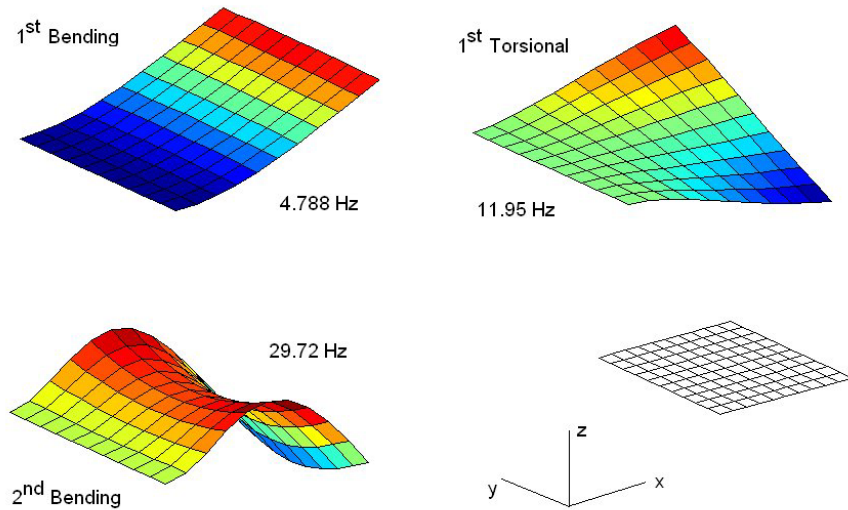
Figure 3.56. Mode shapes and modal frequencies with full bonding.
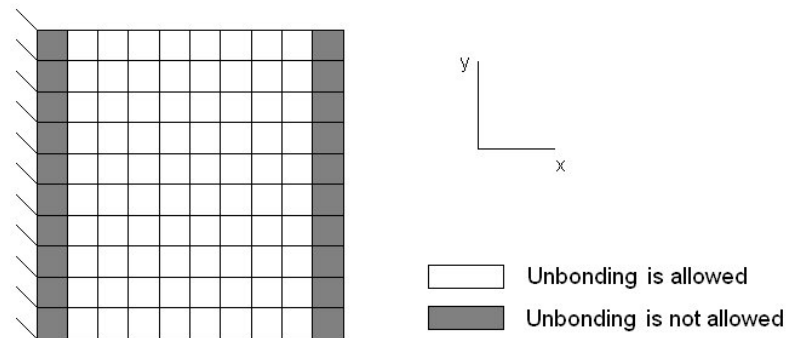
Figure 3.57. Debonding is not allowed along the elements located near the edges.

Because of the imposed constraint, number of possible configurations reduces from 3025 to 1981. In fact, it is not meaningful to have an edge delamination, since instead one may employ a smaller actuator patch. One other reason to have such constraint is easiness of handling the solutions. When edge delamination is allowed, there may be low frequency local modes associated with the vibration of the unbonded portion of the actuator (antisymmetric modes). This behavior may cause a change in the frequency wise ordering of the modes. For example, although for fully bonded case, first three modes are first bending, first torsional and second bending modes respectively, when there is an edge

133

delamination as shown in Figure 3.58, three other modes having smaller frequencies exist and change the order. Even for constrained cases, best solutions must be checked if their first three modes are desired modes. It may be also noted that effect of contact between the layers, which is ignored in this study, may be very important for some of these antisymmetric modes.
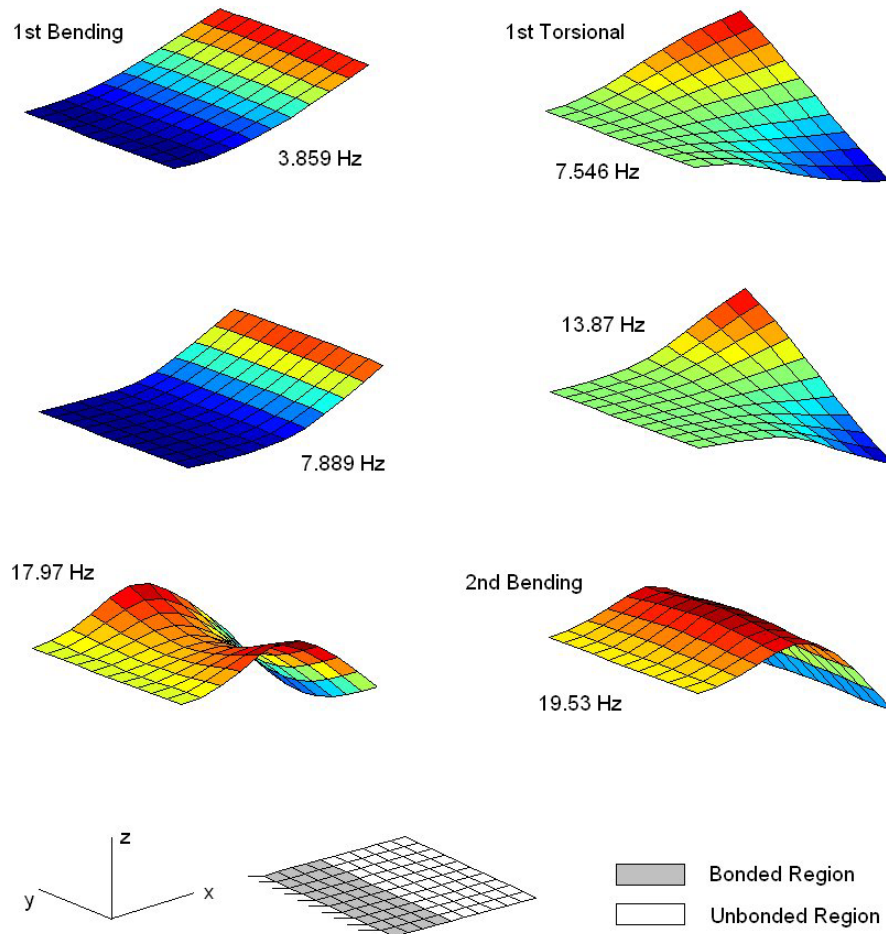
Figure 3.58. Mode shapes of the substrate for 2-layered plate when the unbonded region is at the edge.

In Table 3.40, first three modal frequencies are compared for two separate configurations in Figure 3.59 and Figure 3.60 respectively. The configuration (Figure 3.59) is best solution for maximizing modal displacements of first and second bending modes. On the other hand, the configuration (Figure 3.60) is best solution for second objective, modal displacement of first torsional mode. As seen

134

in Figure 3.59 and Figure 3.60, although mode shapes of first three modes are not exactly same with the mode shapes of fully bonded case, they are still similar to first bending, first torsional and second bending modes. However, as seen in Table 3.40, modal frequencies are lower than the fully bonded case, which indicates a reduction in the stiffness of the structure as expected. In addition, application surfaces of actuation forces changes because of unbonding. Combined effect of these makes the modal displacements much higher as compared with the fully bonded case as seen in Table 3.41. Unlike the previous example, static displacement of a particular point, modal displacements are very sensitive to design variables. Therefore, improvements in the values of objectives are quite satisfactory when compared with the fully covered case.

Table 3.40 Percent improvement in the values of the objectives with respect to fully bonded case.

Mode	Modal Frequency (Hz)		
	Fully covered	Configuration given in Figure 3.59	Configuration given in Figure 3.60
1 (1st Bending)	4.788	3.737	4.222
2 (1st Torsional)	11.95	8.026	9.783
3 (2nd Bending)	29.72	18.85	21.49
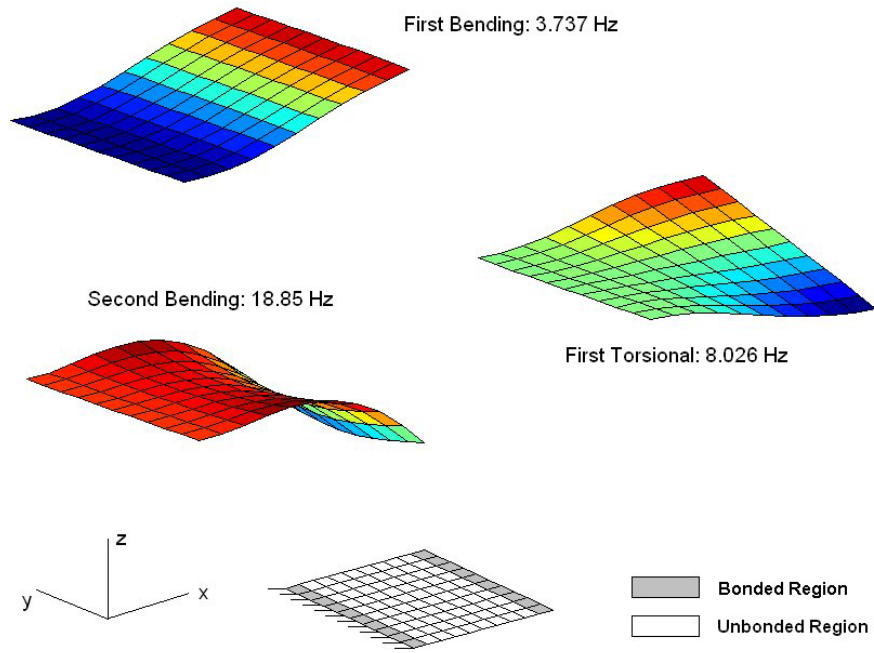
Figure 3.59. First three mode shapes of best configuration of first and third objectives.
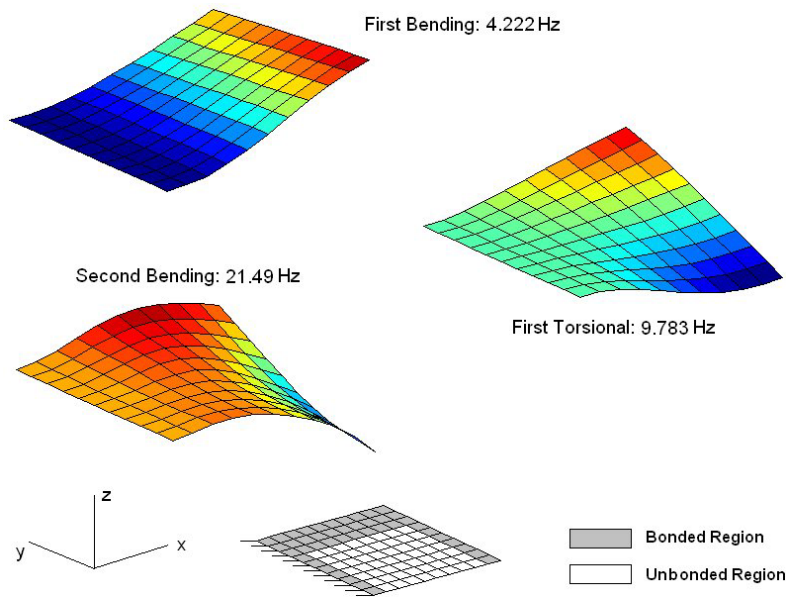
Figure 3.60. First three mode shapes of best configuration of second objective.

136

Table 3.41. Obtained improvements with respect to fully bonded case. Since fully bonded case has no control on first torsional mode, improvement due to configuration given in Figure 3.60 can not be given.

Objective Function	Percent improvement for Configuration given in Figure 3.59	Percent Improvement for Configuration given in Figure 3.60
1 (1st Bending)	55.37	25.30
2 (1st Torsional)	No Improvement	Not Applicable
3 (2nd Bending)	491.4	235.9

Whole set of Pareto solutions can be presented, since results were already obtained for all possible configurations. However, the configuration of each Pareto solution must be checked if their first three modes are first bending, first torsional and second bending modes respectively. Then it is possible to obtain correct Pareto frontal surface by eliminating those unaccepted solutions.

3.7.4. Summary of the Chapter

A new set of design variables, which are related to geometry of the geometry of the debonding area, is introduced to maximize the effect of the actuation of piezoelectric patches. Two case studies are considered. Although, improvement due to unbonding for objective considered in the first case study is very small, for the second case study, where modal displacements of first three modes of fully bonded cases are selected as objectives, substantial improvement is obtained. Therefore, in addition to placement of actuators, placement of unbonded region between the actuator and substrate is also a good design challenge for maximizing the actuator effectiveness.

CHAPTER 4

SUMMARY AND CONCLUSIONS

4.1. MODELING STUDIES

In this study, a consistent finite element model, which includes the adhesive layer flexibility for piezolaminated plates, was developed. This model, MLP-FAB, is also suitable for modeling multiple delamination regions between the layers. Excluding adhesive layers, each layer is modeled individually using Classical Plate Theory. Then special adhesive layer elements are used to attach the elements representing these layers. Results found for developed model were verified with the analytical and numeric results found in the literature. Furthermore, for comparison purposes, several FE models consisting of solid elements were also developed using MSC.NASTRAN, commercial FE package program. After considering static deformations and modal analyses, good agreement between the results was demonstrated. It was also shown that, estimated stresses in adhesive layer for delaminated or undelaminated cases were very close with the stresses existed in solid model.

Static displacements of models having hard and soft adhesives were compared. It was observed that, stiffness or thickness of the adhesive layer has an important effect on these results. Effects of delamination on the adhesive stresses were also investigated. It was seen that, although deformed shapes are quite similar, local stresses near the delamination edge differ an important amount in adhesive layer. High stress gradients in those regions were observed as expected.

4.2. OPTIMIZATION STUDIES

In the second part of the study, maximization of actuation effect was addressed. For this purpose, either actuator locations or parameters related to

unbonded region geometry were employed as design variables. The latter technique is easily applicable for most practical engineering problems. It is demonstrated that by finding best bonding geometry, an important amount of increase in objective function values were obtained especially when modal displacements are selected as design variables. If the stiffness of the actuators is comparable with the stiffness of the substrate, creating an unbonded region decrease the stiffness of the whole structure an important amount and makes the system more controllable with a less effort. Furthermore, re-distribution of actuation forces due to selective bonding may increase the control effectiveness.

For both placement of actuators and optimization of debonding region cases, design variables were considered as discrete parameters since already existing FE mesh is used for every iteration step. It may be noted that, changing mesh for each one of iterations may not be suitable since there may be different level of FE modeling errors for different mesh configurations.

Full combinations were obtained; in addition a simulated annealing optimization method, 'Hide and Seek' [55] was used to find optimum configurations. Single and multi-objective optimization problems were solved considering different objectives related to static and dynamic response of the structure. Pareto solutions for multi-objective cases were identified considering all combinations. Since modal displacements of different vibration modes are generally very conflicting design objectives, non-convex 2D and 3D Pareto frontal surfaces were obtained. For simulated annealing method, different search techniques were considered and compared. Furthermore, a multi-objective SA method (MC-MOSA) [58] is also used in some placement problems. For these problems, maximization of the diagonal elements or eigenvalues of the controllability grammian of some selected modes, and minimization of the controllability for the selected spillover modes were the objectives.

Since objective function values of full combinations of possible configurations is obtained for some case studies, it is compared with results found using simulated annealing method to examine the effectiveness of the optimization method. In view of the fact that different search and cooling techniques are employed, different optimization parameters are needed to run the method appropriately. As seen in Section 3.5, although some of these methods with same parameters were successful in others, they were not successful.

139

Examining the results of selected case studies, following suggestions may be made;

- For multiple actuator placement problems, it is advisable to change the position of a randomly selected single patch in every iteration step instead of changing location of all patches.

- When 'Random Walk' method is used as search technique, randomness associated with the search method increases. Although, it is favorable to seek distant global optima, for selected case studies, this technique decreases the effectiveness of the optimization method. Therefore it is not suggested especially for single objective cases

- Adaptive search, which changes step size according to the temperature, which is control parameter of optimization method, is recommended. A coarse global search at the beginning, when temperature is high, and a fine-tuning search around the global optimum, when temperature is low, increases the efficiency of the optimization method.

- In the studied multi-objective examples, linear combinations of the objective functions are used to construct the fitness functions used in MC-MOSA optimization method. Higher order fitness functions may also be used. However, the results obtained using linear type of fitness functions, are quite good to get solutions, which are very close to the actual Pareto front.

4.3. RECOMMENDED FUTURE STUDIES

The following items should be addressed in future studies;

- Instead of using Classical Plate Theory assumptions, a different set of assumptions can be used when modeling individual layers. Namely, first or higher order shear deformation theories may be used.

- Actuator placement and debonding area optimization problems were considered separately in this study. All design variables related to these problems may be employed simultaneously.

- Continuous design variables such as applied voltages on different piezoelectric patches may be employed in addition to the previous discrete design variables. In that case, an optimization method, which is capable of handling continuous and discrete variables at the same time, shall be used.

- For multi-objective cases, obtained Pareto solutions are candidates for best solution. However, choosing best solution for a specific practical problem generally requires a good engineering experience on the area of that problem. Therefore, some case studies may be conducted to discuss the selection of best solution from the set of all Pareto solutions.

APPENDIX A

'HIDE AND SEEK' SIMULATED ANNEALING METHOD

There is an analogy between the annealing process, metal cools and freezes into a minimum energy crystalline structure, and the search for a global optimum in a more general system by implementing a cooling algorithm. Therefore the method is called as simulated annealing algorithm. The algorithm employs a random search, which not only accepts changes that decrease the objective function, but also some changes that increase it. Major advantage of the method over other methods is the ability of avoiding to be trapped at local optima. Method does not need any gradient information and easily applicable to discrete problems. However, it generally requires large number of function evaluations according to gradient-based algorithms.

In order to find optimum location of piezoelectric patches on a given plate structure, having a pre-defined FE mesh, we have to solve a combinatorial optimization problem. For this purpose, a discrete simulated annealing optimization algorithm, which is capable of using different search techniques, is studied in this section. Comparison between these search algorithms is also conducted to find the method, which suits our problems best. Another purpose of this study is to develop a robust optimization algorithm, which does not need fine-tuning of optimization parameters for different problems. The flowchart of the proposed algorithm is given in Figure A.1.
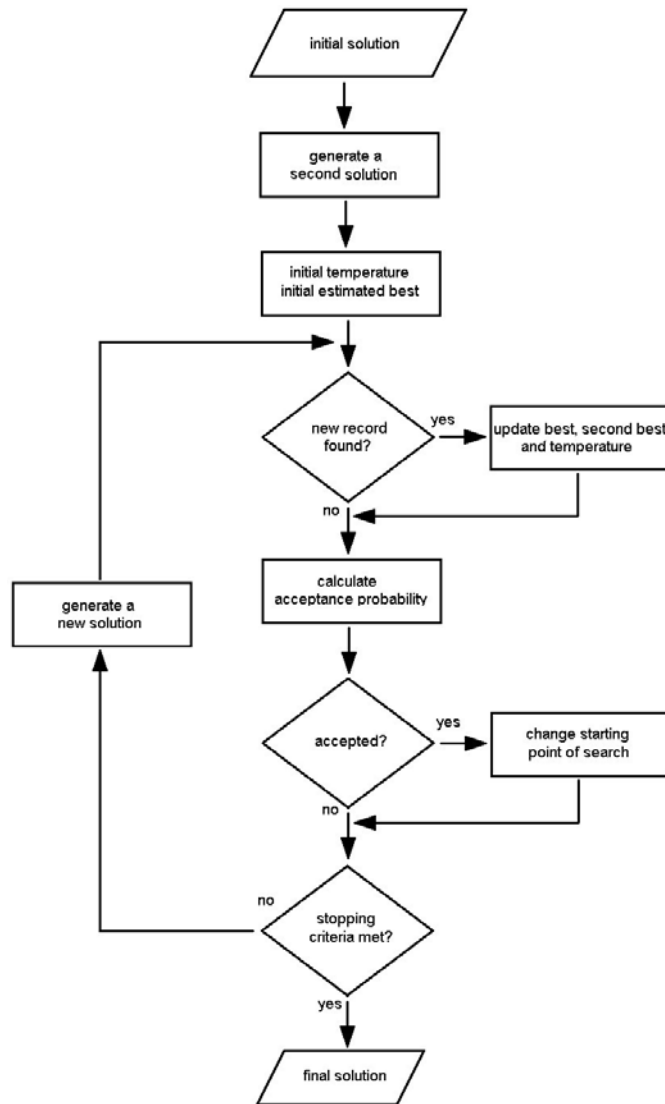
Figure A.1. Flowchart of optimization method used.

Calculation of the Temperature and Acceptance Criterion

Control parameter of the 'Hide and Seek' SA optimization method, temperature may be found from [55];

$$THS = 2\frac{f*-f(x)}{\chi^2_{1-p}(d)}$$
(A.1)

where $\chi^2_{1-p}(d)$ is equal to value of cumulative density function of chi-square distribution with *d* degrees of freedom and probability of '1-*p*', *f(x)* is value of the objective for current solution and *f** is estimated best which is found from;

$$f^* = f_1 + \frac{f_1 - f_2}{(1-p)^{-d/2} - 1} \tag{A.2}$$

where f_1 and f_2 are best and second best values of objective functions found so far, *p* corresponds to probability that the real best is better than estimated value. However, our problems may have symmetric configurations for design variables. In order to discard these solutions when updating f_1 and f_2, solutions that are very close to f_1 or f_2 are not taken into account.

Then using the calculated temperature, acceptance probability of the new solution as new starting point for maximization problem is;

$$\beta = \min(1, e^{\frac{f(x) - f_{sp}}{T}}) \tag{A.3}$$

where f_{sp} is value of the objective function at the last accepted point which is used as starting point of the search for each iteration step.

APPENDIX B

MULTIPLE COOLING – MULTI OBJECTIVE SIMULATED ANNEALING METHOD (MODIFIED FOR DISCRETE PROBLEMS)

A discrete multi-objective problem may be defined as;

$$\text{maximize or minimize } \{f_i(\mathbf{x})\} \quad i = 1,..,n$$

$$\text{subject to } \begin{aligned} g_i(\mathbf{x}) &\leq 0 \quad i = 1,..,p \\ h_i(\mathbf{x}) &= 0 \quad i = 1,...,r \\ x_i^L &\leq x_i \leq x_i^U \quad i = 1,...,s \\ x_i &\in N \quad i = 1,..,n \end{aligned} \tag{B.1}$$

However, studied problems do not have functional constraints. The limit constraints on the design variables are existed for the placement problems. Since the search technique is responsible to find a solution in the feasible region, only the objective functions are critical for modified MC-MOSA algorithm.

Unlike single objective case, values of the fitness functions are utilized when deciding the acceptance of the last solution. For linear case, these fitness functions are set of weighted sums of the objective functions;

$$z_k = \sum_{i=1}^{n} w_{ki} f_i(\mathbf{x}) \quad k = 1,..,m \tag{B.2}$$

Where, the weight sets are;

$$\sum_{i=1}^{n} w_{ki} = 1 \quad k = 1,..,m \tag{B.3}$$

Alternatively, nonlinear fitness functions may also be employed. However, in this study, only linear type of these functions is used.

Normalizing the values of the objective functions may eliminate the main disadvantages of this method. Without any normalization, different objective functions may have values of different order of magnitudes. Therefore the values of the fitness functions may be insensitive for some objective functions. In this study current maximum or current minimum values of the objective functions are used for non-dimensionalization. Therefore fitness functions are;

$$\bar{z}_k = \sum_{i=1}^{n} w_{ki} \, \bar{f}_i(\mathbf{x}) \quad k = 1,..,m \tag{B.4}$$

where

$$\bar{f}_i(\mathbf{x}) = \frac{f_i(\mathbf{x}_{current})}{\max\{f_i(\mathbf{x}_0, \mathbf{x}_1,..., \mathbf{x}_{current-1})\}} \quad i = 1,..,n \tag{B.5}$$

It may be noted that, Equation (B.5) is used for objective functions always having positive values. Selected objective functions, in the examples, satisfy this condition. Since current maximum may change during the iterations, past values of the non-dimensional objective functions must be updated. Otherwise, best value estimator used in 'Hide and Seek' method does not work properly.

Since values of the fitness functions are used to accept or reject the test points, different temperatures associated with each of these functions, are employed. If any of the fitness functions is improved, related temperature is also updated. In addition, estimated best of this fitness function is also changed.

It should be noted that, suggested non-dimensionalization may not be suitable if constraint are converted to penalty functions and added to the objective function.

Algorithm of Modified MC-MOSA Method

Step 0: Chose a starting point $\mathbf{x}_0$ in the feasible region. Set initial temperatures as sufficiently high. Set iteration number $k = 0$. Choose a weight set for fitness functions.

Step 1: Set $k = k + 1$. Find a search direction θ_k and determine the step length λ_k to find a new test point in the feasible region. One of the search techniques, suggested for single objective problems may be used. Rounding off is used to get integer values. Then find the new test point;

$$y_k = x_{k-1} + \theta_k \lambda_k$$

Step 2: Find the values of objective functions and non-dimensionalize them. If any record found for the objective functions, also non-dimensionalize past values of the objective functions. Calculate the values of the fitness functions. Find which fitness function improves most. Update the temperatures and estimated bests of the fitness functions, which have new records. Accept the test point as new search starting point. If none of the fitness functions improves, set the acceptance probability as highest probability among the probabilities of all fitness functions. Accept or reject the test point using this probability.

Step 3: Check if any of the stopping criteria is met. Total number of allowed iterations, number of consequent iterations having low probability or number of consequent iterations without any new record of fitness functions may be employed as stopping criteria. If none of them is satisfied, go to Step 1.

REFERENCES

[1]   Padula, S.L., Kincaid, R. K., 'Optimization Strategies for Sensor and Actuator Placement', NASA/TM-1999-209126, April 1999.

[2]   Frecker, M.I., 'Recent Advances in Optimization of Smart Structures and Actuators', Journal of Intelligent Material Systems and Structures 2003; 14(4):207-216.

[3]   Pletner, B., Abramovich H., 'Consistent Methodology for the Modeling of Piezolaminated Shells', AIAA J. 1997; 35(8):1316-1326.

[4]   Reddy, J.N., 'On Laminated Composite Plates with Integrated Sensors and Actuators', Engineering Structures 1999; 21(7):568-593.

[5]   Liu, G.R., Peng, X.Q., Lam, K.Y., Tani, J., 'Vibration Control Simulation of Laminated Composite Plates with Integrated Piezoelectrics', Journal of Sound and Vibration 1999; 220(5):827-846.

[6]   Correia, V.M.F., Gomes, M.A.A., Suleman, A., Soares, C.M.M., Soares, C.A.M., 'Modelling and Design of Adaptive Composite Structures', Computer Methods in Applied Mechanics and Engineering 2000; 185:325-346.

[7]   Carrera, E., 'Historical Review of Zig-Zag Theories for Multilayered Plates and Shells', Applied Mechanics Review 2003; 56(3):287-308.

[8]   Carrera, E., 'Multilayered Shell Theories Accounting for Layerwise Mixed Description, Part 1 - Governing Equations', AIAA J. 1999; 37(9):1007-1016.

[9]   Carrera, E., 'Multilayered Shell Theories Accounting for Layerwise Mixed Description, Part 2 - Numerical Evaluations', AIAA J. 1999; 37(9):1117-1124.

[10]   Carrera, E., 'Evaluation of Layerwise Mixed Theories for Laminated Plates Analysis', AIAA J. 1998; 36(5):830-839.

[11]   Carrera, E., 'Single vs Multilayer Plate Modelings on the Basis of Reisner's Mixed Theorem', AIAA J. 2000; 38(2):542-552.

[12]   Brank, B., Carrera, E., 'Multilayered Shell Finite Element with Interlaminar Continuous Shear Stresses: A Refinement of the Reissner-Mindlin Formulation', International Journal For Numerical Methods In Engineering 2000; 48(5):843-874.

[13]   Icardi, U., '8-Noded Zigzag Element for Deflection and Stress-Analysis of Plates with General Lay-Up', Composites Part B – Engineering 1998; 29(4):425-441.

[14]   Heyliger, P., Pei, K.C., Saravanos, D., 'Layerwise Mechanics and Finite-Element Model for Laminated Piezoelectric Shells', AIAA J. 1996; 34(11):2353-2360.

[15]   Han, J.H., Lee, I., 'Analysis of Composite Plates with Piezoelectric Actuators for Vibration Control Using Layerwise Displacement Theory', Composites Part B – Engineering 1998; 29(5):621-632.

148

[16]   Tzou, H.S., Ye, R., 'Analysis of Piezoelastic Structures with Laminated Piezoelectric Triangle Shell Elements', AIAA J. 1996; 34(1):110-115.

[17]   Masud, A., Panahandeh, M., 'Finite-Element Formulation for Analysis of Laminated Composites', Journal of Engineering Mechanics-ASCE 1999; 125(10):1115-1124.

[18]   Saravanos, D.A., 'Mixed Laminate Theory and Finite-Element for Smart Piezoelectric Composite Shell Structures', AIAA J. 1997; 35(8):1327-1333.

[19]   Saravanos, D.A., Heyliger, P.R., Hopkins, D.A., 'Layerwise Mechanics and Finite-Element for the Dynamic Analysis of Piezoelectric Composite Plates', International Journal of Solids and Structures 1997; 34(3):359-378.

[20]   Tzou, H.S., Tseng, C.I., 'Distributed Dynamic Identification and Controls of Flexible Shells', AIAA-90-1089-CP 1989.

[21]   Ha, S.K., Chang, F., 'Finite Element Modeling of the Response of Laminated Composites with Distributed Piezoelectric Actuators', AIAA-90-1131-CP 1990; 2323-2330.

[22]   Ochoa, O.O., Reddy, J.N., *Finite Element Analysis of Composite Laminates*. Dordrecht: Kluwer Academic, 1992.

[23]   Reddy, J.N., *Mechanics of Laminated Composite Plates*. Boca Raton: CRC Press; 1997.

[24]   Moorthy, C.M.D., Reddy, J.N., 'Modeling of Laminates Using a Layerwise Element with Enhanced Strains', International Journal For Numerical Methods In Engineering 1998; 43(4):755-779 .

[25]   Moorthy, C.M.D., Reddy, J.N., 'Recovery of Interlaminar Stresses and Strain-Energy Release Rates in Composite Laminates', Finite Elements In Analysis And Design 1999; 33(1):1-27.

[26]   Yuceoglu, U., Updike, D.P., 'Comparison of Continuum and Mechanical Spring Models of Adhesive Layers in Bonded Joints', In: Advances in Aerospace Structures and Materials, ASME Publication 1981; AD-Vol.01:75-83.

[27]   Tekinalp, O., Yuceoglu, U., Caglayan, N., 'Vibrations of Two-Layer, Orthotropic, Beamlike Strips Connected by Mechanical Springs', In: Recent Developments in Composite Materials and Structures, Eds.: Hui, D., Sun, C.T., an ASME publication 1990; AD-Vol.19/AMD-Vol.113:67-72.

[28]   Tekinalp, O., Yuceoglu, U., Yavuz, A., 'Natural Vibration Characteristics of Composite Multilayer Beams and Blades', In: Ferguson, N.S., Wolfe, H.W., Mei, C., editors. Structural Dynamics: Recent Advances. ISVR, Univ. of Southampton, England, 1994.

[29]   Yuceoglu, U., Toghi, F., Tekinalp, O., 'Free Bending Vibrations of Adhesively Bonded, Orthotropic Plates with Single Lap Joint', ASME Journal of Vibration and Acoustics 1996; 118(1):122-134.

[30]   Li, D.S., Cheng, L., Gosselin, C.M., 'Optimal Design of PZT Actuators in Active Structural Acoustic Control of a Cylindrical Shell with a Floor Partition', Journal of Sound and Vibration 2004; 269:569–588.

[31]   Damaren, C.J., 'Optimal Location of Collocated Piezo-Actuator/Sensor Combinations in Spacecraft Box Structures', Smart Materials Structures 2003; 12:494–499.

[32]   Maxwell, N. D., Asokanthan, S. F., 'Optimally Distributed Actuator Placement and Control for a Slewing Single-Link Flexible Manipulator', Smart Materials And Structures 2003; 12:287–296.

[33]   Yan, Y. J., Yam, L. H., 'Optimal Design of Number and Locations of Actuators in Active Vibration Control of a Space Truss', Smart Materials And Structures 2002; 11:496–503.

[34]   Ip, K., Tse, P., 'Optimal Configuration of a Piezoelectric Patch for Vibration Control of Isotropic Rectangular Plates,' Technical Note, Smart Materials And Structures 2001; 10:395-403.

[35]   Gao, W., Chen, J.J., Ma, H.B., Ma, X.S., 'Optimal Placement of Active Bars in Active Vibration Control for Piezoelectric Intelligent Truss Structures with Random Parameters', Computers and Structures 2003; 81:53-60.

[36]   Locatelli, G., Langer, H., Muller, M., Baier, H., 'Simultaneous optimization of actuator placement and structural parameters by mathematical and genetic optimization algorithms', Proc. of IUTAM Conference Smart Structures and Structronic Systems, Kluwer ed., Sept. 2000, Magdeburg.

[37]   Han, J.H., Lee, I., 'Optimal Placement of Piezoelectric Sensors and Actuators for Vibration Control of a Composite Plate Using genetic Algorithms', Smart Materials and Structures 1999; 8(2):257-267.

[38]   Sadri, A. M., Wright, J. R., Wynne R. J., 'Modelling and Optimal Placement of Piezoelectric Actuators in Isotropic Plates Using Genetic Algorithms', Smart Materials and Structures 1999; 8:490-498.

[39]   Zhang, H., Lennox, B., Goulding, P.R., Leung, A.Y.T., 'A Float-Encoded Genetic Algorithm Technique for Integrated Optimization of Piezoelectric Actuator and Sensor Placement and Feedback Gains', Smart Materials and Structures 2000; 9:552-557.

[40]   Gao, F., Shen Y., Li, L., 'The Optimal Design of Piezoelectric Actuators for Plate Vibroacoustic Control Using Genetic Algorithms with Immune Diversity', Smart Materials and Structures 2000; 9:485-491.

[41]   Metropolis, N., Rosenbluth. A., Rosenbluth, M., Teller, A., Teller, E., 'Equation of State Calculations by Fast Computing Machines', Journal of Chemical Physiscs 1953; 21(6):1080-1092.

[42]   Kirkpatrick, S., Gelatt, C., Vecchi, M., 'Optimization by Simulated Annealing', Science 1983, 220(4598):671-680.

[43]   Chen, G., Bruno, R. J., Salama, M., 'Optimal Placement of Active/Passive Members in Truss Structures Using Simulated Annealing', AIAA J. 1991; 29(8):1327-1334.

[44]   Liu X., Begg, D.W., Matravers, D.R., 'Optimal Topology/Actuator Placement Design of Structures Using SA', Journal of Aerospace Engineering 1997; 10(3):119-125.

[45]   Nguyen, C., Pietrzko, S., Buetikofer, R., 'The Influence of Temperature and Bonding Thickness on the Actuation of a Cantilever Beam by PZT Patches', Smart Materials and Structures 2004; 13:851-860.

[46]   Wu, T., Ro, P., 'Dynamic Peak Amplitude Analysis and Bonding Layer Effects of Piezolelectric Bimorph Cantilevers', Smart Materials and Structures 2004; 13:203-210.

[47]   Ikeda, T., *Fundamentals of Piezoelectricity*. Oxford: Oxford University Press; 1990.

[48]   Cheng, D.K., *Field and Wave Electromagnetics*. Addison-Wesley Pub Co; 1989.

[49]   Robbins, D.H., Reddy, J.N., 'Analysis of Piezoelectrically Actuated Beams Using a Layer-Wise Displacement Theory', Computers and Structures 1991; 41(2):265-279.

[50]   Carrera, E., Demasi, L., Manganello, M., 'Assesment of Plate Elements on Bending and Vibrations of Composite Structures', Mechanics of Advanced Materials and Sructures 2002; 9(4):333-357.

[51]   Junkins JL, Kim Y, *Introduction to Dynamics and Control of Flexible Structures*, AIAA Inc., 1993.

[52]   Hac A, Liu L, 'Sensor and Actuator Location in Motion Control of Flexible Structures', J of Sound and Vibration, 1993; 167(2);239-61.

[53]   Sarafin TP, *Spacecraft Structures and Mechanisms*, Kluwer Academic Publishers, 1995.

[54]   Barboni, R., Mannini, A., Fantini, E., Gaudenzi, P., 'Optimal Placement of PZT Actuators for the Control of Beam Dynamics', Smart Material and Structures 2000; 9:110-120.

[55]   Belisle, C.J.P., Romeijn, E.R., Smith, R.L., 'Hide-and-Seek: a Simulated Annealing Algorithm for Global Optimization' Department of Industrial and Operations Engineering, Univ. Of Michigan, Technical Report 90-25, 1990.

[56]   Lehmann, E.L., *Elements of Large Sampling Theory*, Springer, New York, 1999.

[57]   Press, W.H., Flannery, B.P., Teukolsky, S.A., *Numerical Recipes in C: The Art of Scientific Computing*. Cambridge University Press, 1992.

[58]   Karslı, G., *Simulated Annealing For The Generation Of Pareto Fronts With Aerospace Applications*, M.S. Thesis, Aeronautical Engineering Department, METU, Ankara, January 2004

CURRICULUM VITAE

PERSONEL INFORMATION

Surname, Name: Ertürk, Cevher Levent
Nationality: Turkish
Date and Place of Birth: 13 December 1971, Ankara
Marital Status: Married
Military Service: Completed in May 2000
Phone: +90 (312)210 10 50-1247
Fax: +90 (312) 210 13 15
Email: levent.erturk@bilten.metu.edu.tr

EDUCATION

Degree	Institution	Year of Grad.
MS	METU Aeronautical Engineering	1996
BS	METU Aeronautical Engineering	1993
High School	Bahçelievler Deneme Lisesi, Ankara	1988

WORK EXPERIENCE

Year	Place	Enrollment
Jun.2000-Present	TÜBİTAK-BİLTEN, Ankara	Senior Engineer
Aug.2001-Jun.2002	SSTL, Guildford, UK (Assigned by BİLTEN)	KHTT Engineer
Nov.1997-Apr.2000	TAI, Ankara	Design Engineer
Oct.1997-Feb.1998	ALENIA, Napples Italy (Assigned by TAI)	Design Engineer
Jan.1997-Aug.1997	Sikorsky Aircraft, Stratford, CT USA	O.J. Training
Aug1996-Dec.1996	GIT, Dep. Aerospace Eng., Atlanta, GA USA	O.J. Training
Oct.1993-Jun.1996	METU Dep. of Aeronautical Eng., Ankara	Res. Assistant

FOREIGN LANGUAGES

Fluent English, Basic French

PAPERS

1. Erturk, C.L., Tekinalp, O., 'A Layerwise Approach to Piezo-Electric Plates Accounting for Adhesive Flexibility and Delaminated Regions', Computers and Structures 2005;83(4):279-296

2. Erturk, C.L., Tekinalp, O., 'Modeling of Laminated Plates With Surface Bonded Piezoelectric Sensors and Actuators', *2002 AIAA, ASME, AHS, Structures, Structural Dynamics, and Materials Conference, Adaptive Structures Forum*, AIAA-2002-1440, April 22-25, Denver, Colorado.